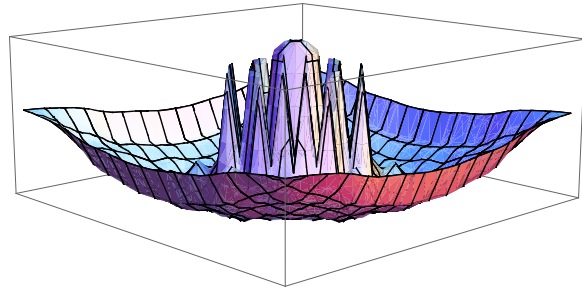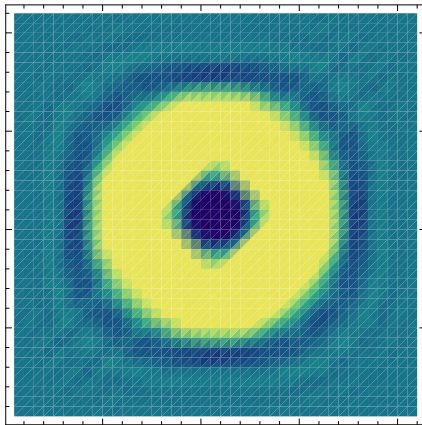# Superfluid and Antiferromagnetic phases in Ultracold Fermionic Quantum Gases

D I S S E R T A T I O N

zur Erlangung des Grades
"Doktor der Naturwissenschaften"

am Fachbereich Physik, Mathematik und Informatik
der Johannes Gutenberg-Universität
in Mainz

Tobias Gottwald
geb. in Mainz

Mainz, den 27.08.2010
(D77)

Abstract

In this thesis several models are treated, which are relevant for ultracold fermionic quantum gases loaded onto optical lattices. In particular, imbalanced superfluid Fermi mixtures, which are considered as the best way to realize Fulde-Ferrell-Larkin-Ovchinnikov (FFLO) states experimentally, and antiferromagnetic states, whose experimental realization is one of the next major goals, are examined analytically and numerically with the use of appropriate versions of the Hubbard model.

The usual Bardeen-Cooper-Schrieffer (BCS) superconductor is known to break down in a magnetic field with a strength exceeding the size of the superfluid gap. A spatially inhomogeneous spin-imbalanced superconductor with a complex order parameter known as FFLO-state is predicted to occur in translationally invariant systems. Since in ultracold quantum gases the experimental setups have a limited size and a trapping potential, we analyze the realistic situation of a non-translationally invariant finite sized Hubbard model for this purpose. We first argue analytically, why the order parameter should be real in a system with continuous coordinates, and map our statements onto the Hubbard model with discrete coordinates defined on a lattice. The relevant Hubbard model is then treated numerically within mean field theory. We show that the numerical results agree with our analytically derived statements and we simulate various experimentally relevant systems in this thesis.

Analogous calculations are presented for the situation at repulsive interaction strength where the Néel state is expected to be realized experimentally in the near future. We map our analytical results obtained for the attractive model onto corresponding results for the repulsive model. We obtain a spatially invariant unit vector defining the direction of the order parameter as a consequence of the trapping potential, which is affirmed by our mean field numerical results for the repulsive case. Furthermore, we observe domain wall formation, antiferromagnetically induced density shifts, and we show the relevant role of spin-imbalance for antiferromagnetic states.

Since the first step for understanding the physics of the examined models was the application of a mean field approximation, we analyze the effect of including the second order terms of the weak coupling perturbation expansion for the repulsive model. We show that our results survive the influence of quantum fluctuations and show that the renormalization factors for order parameters and critical temperatures lead to a weaker influence of the fluctuations on the results in finite sized systems than on the results in the thermodynamical limit. Furthermore, in the context of second order theory we address the question whether results obtained in the dynamical mean field theory (DMFT), which is meanwhile a frequently used method for describing trapped systems, survive the effect of the non-local Feynman diagrams neglected in DMFT.

Kurzfassung

In dieser Dissertation werden unterschiedliche, für ultrakalte fermionische Quantengase relevante Modelle behandelt. Insbesondere suprafluide Fermi-Mischungen mit Spin-Ungleichgewicht, die als beste Möglichkeit zur experimentellen Verwirklichung von Fulde-Ferrell-Larkin-Ovchinnikov (FFLO)-Zuständen in Betracht kommen, und antiferromagnetische Zustände, deren experimentelle Herstellung eines der größten Ziele der nächsten Zeit ist, werden analytisch und numerisch unter Benutzung verschiedener Varianten des Hubbard-Modells untersucht.

Der herkömmliche Bardeen-Cooper-Schrieffer (BCS) Supraleiter bricht in einem Magnetfeld mit einer Stärke, die größer ist als seine suprafluide Lücke, zusammen. Ein räumlich inhomogener Supraleiter mit einem Spin-Ungleichgewicht und einem komplexen Ordnungsparameter, bekannt als FFLO-Zustand, stellt sich in translationsinvarianten Systemen ein. Da ultrakalten Quantengasen eine kleine Systemgröße und ein Fallenpotential zugrundeliegen, untersuchen wir zu diesem Zweck die realistische Situation eines nicht translationsinvarianten Hubbard-Modells mit beschränkter Sytemgröße. Wir argumentieren zuerst analytisch in einem System mit kontinuierlichen Ortskoordinaten, warum der Ordnungsparameter eine reelle Größe sein sollte und bilden diese Ergebnisse auf ein Hubbard-Modell mit diskreten, auf einem Gitter definierten, Ortskoordinaten ab. Das relevante Hubbard-Modell wird dann in Molekularfeldnäherung numerisch behandelt. Wir zeigen, dass unsere numerischen Ergebnisse zur analytischen Voraussage passen und simulieren verschiedene experimentell relevante Modelle in dieser Dissertation.

Analoge Rechnungen werden für die Situation bei abstoßender Wechselwirkung präsentiert. Für diesen Fall wird in naher Zukunft das Gelingen der experimentellen Herstellung eines Néel-Zustandes erwartet. Wir bilden unsere analytischen Ergebnisse für das Modell mit anziehender Wechselwirkung auf entsprechende Resultate für das Modell mit abstoßender Wechselwirkung ab. Dabei erhalten wir als Konsequenz des Fallenpotentials einen nicht von den Ortskoordinaten abhängigen Einheitsvektor, der über das gesamte System parallel zum antiferromagnetischen Ordnungsparameter steht. Dieser wird auch durch unsere numerischen Ergebnisse bestätigt. Darüber hinaus beobachten wir die Bildung von Domänengrenzen und antiferromagnetisch induzierter Veränderung von Teilchendichten. Ferner zeigen wir die relevante Rolle, die Spin-Ungleichgewicht in antiferromagnetischen Systemen spielt.

Da der erste Schritt zum Verstehen der untersuchten Modelle die Anwendung der Molekularfeldnäherung war, analysieren wir auch die durch Quantenfluktuationen entstehenden Effekte durch die Hinzunahme der zweiten Ordnung der Störreihe bei abstoßender Wechselwirkung. Wir zeigen, dass unsere Ergebnisse den Einfluß der Fluktuationen überleben und dass die Renormierungsfaktoren für Ordnungsparameter und kritische Temperaturen bei kleinen Systemen zu einem geringeren Einfluß führen als im thermodynamischen Limes. Außerdem stellen wir die Frage, ob Ergebnisse, die in der mittlerweile zur Beschreibung von Fallensystemen üblich gewordenen Dynamischen Molekularfeldtheorie (DMFT) erhalten worden sind, die nicht-lokalen Effekte, die in DMFT vernachlässigt werden, überleben.

Contents

Chapter 1

Introduction

The experimental realization of a Bose-Einstein condensate (BEC) in 1995 opened up a new research field [1]. For bosons, the addition of optical lattices led to the experimental realization of the Bose-Hubbard model [2, 3]. Phenomena as the bosonic superfluid to Mott-insulator transition have been experimentally detected [4, 5, 6, 7, 8, 9]. Within this framework the experimental simulation of microscopic models has been achieved. Also phenomena using a tiny number of lattice sites as second order atom tunneling [10] and time-resolved control of the superexchange interaction [11] have been realized in the context of ultracold quantum gases.

Coherent pairing for fermions has been in the focus of research since the middle of the last century in the context of superconductors. Bardeen, Cooper and Schrieffer suggested a phonon-induced attractive interaction between electrons, explaining the frictionless flow in low-T_C superconductors [12]. Since in ultracold quantum gases interactions are tunable via Feshbach resonances [13], this type of superfluidity has also been realized in ultracold Fermi gases [14]. The first realization of fermionic superfluidity has also generated an interest in further experiments. E.g., superfluid two-component mixtures with a spin-population imbalance have been realized [15, 16, 17, 18, 19, 20, 21]. Phenomena such as vortices have been analyzed, and techniques like the spin-selective in-situ imaging of an atomic cloud have been developed and applied. Furthermore, the crossover from the weak coupling BCS-regime to the strong coupling regime, where the condensate consists of a BEC of two-atomic molecules, has been experimentally achieved and theoretically described [22, 23, 24].

Experiments for fermions on an optical lattice are an additional experimental achievement which became of great interest during the last years, especially in the context of the simulation of the Hubbard model discussed since 1963 [25]. Interaction-free systems have been used, e.g., to observe Fermi surfaces [26] or in order to realize spin-selective transport mechanisms [27]. For repulsive interaction strengths the Mott transition has also been observed experimentally [28, 29, 30]. Superfluidity in optical lattices has also been reported [31] and theoretically analyzed [32, 33].

Ongoing ideas for experiments with fermions on optical lattices deal, e.g., with multicolor superfluids (Fermi-mixtures with more than two components) [34, 35], mixtures with components having different masses [36, 37, 38] or exotic types of superfluidity with p- or d-wave symmetries [39, 40]. Also the use of dipolar molecules possessing a non-isotropic long-ranged interaction is discussed [41, 42, 43].

In recent years magnetic phenomena like (anti-)ferromagnetism have also been taken into account for experiments with fermionic quantum gases. E.g., the Stoner-ferromagnet has been realized in a lattice-free gas at repulsive interaction strength [44]. The realization of the antiferromagnet [45, 46, 47, 48, 49, 50, 51, 52] and the realization of imbalanced superfluids

in one, two, and three dimensions [24, 53, 54, 55, 56, 57, 58] are some of the next major experimental goals. Inspired by these goals, this thesis focuses on the theoretical predictions for trapped experimental environments with a superimposed optical lattice in two dimensions.

1.1   Structure of this thesis

The focus of this work lies on the analysis of superfluid and antiferromagnetic phases at thermal equilibrium in trapped ultracold two-component Fermi mixtures. In the introduction we will present the relevant Hamiltonian, namely the Hubbard model, and show its relation to ongoing experiments.

Since there is a huge variety of literature treating superfluidity and antiferromagnetism using different assumptions on the structure of ordering types, we go back to the roots and derive a continuity equation for superfluid currents. We show that the definition frequently used in the literature is incorrect and introduce the concept of a generalized "supercurrent" for fermions. With the help of the corresponding continuity equation at thermal equilibrium, we formulate statements helping to understand the structure of superfluid and antiferromagnetic order parameters. Although this is a main result of this thesis, we present this topic in the introductionary part, since this result will accompany us through the following chapters.

In chapter 2 we discuss the possible ordering types occurring in the attractive-U Hubbard model in translationally invariant systems. Thereby we introduce the Bardeen-Cooper-Schrieffer (BCS) phase and the Fulde-Ferrel-Larkin-Ovchinnikov (FFLO) phase. Since the repulsive and the attractive Hubbard model may be mapped onto each other for translationally invariant situations, the results of chapter 2 may be transferred to the repulsive case. Chapter 2 shows or at least suggests which phases may occur in trapped systems.

In chapter 3 we present results for trapped systems with attractive interaction. The focus lies on the successful calculation of the superfluid order parameter. We present the effects arising from particle imbalance and/or from spin-dependent hopping. Furthermore, we compare our results to the existing literature and show how we improved those results.

In chapter 4 we treat the case of repulsive interaction strengths, which is not equivalent to the attractive case, if the trapping potential is included in the calculations. We calculate the antiferromagnetic order parameter for balanced and imbalanced systems and suggest possibilities for the experimental detection of the Néel-state in ultracold Fermi gases.

Finally, having neglected quantum fluctuations in chapters 2-4, we include those perturbatively within a real-space Baym-Kadanoff second order expansion in chapter 5. We will apply this formalism on the repulsive-U case and show how quantum fluctuations influence the antiferromagnetic ordering in trapped and in periodic systems.

1.2   Experimental background

It is, of course, of interest to integrate the theoretical results of this work into the experimental background. Therefore, we will briefly discuss how the models studied in this thesis are realized in ultracold quantum gases. We explain how optical lattices are used to create a Hubbard model, we show the role of Feshbach resonances for tuning interactions, and present some imaging techniques.

1.2.1   Optical lattices

Older trapping techniques as the Penning or the Pauli trap are used to store charged ions. Since charged ions interact via a long-range Coulomb interaction, experiments with ultracold

quantum gases are performed using charge neutral atoms. Hence, different trapping methods have to be used. One way to trap neutral atoms are magneto-optical traps. The magnetic part of the trap makes use of a spatially inhomogeneous magnetic field. Since it is the purpose of many experiments to use a constant field in order to tune the interactions (explained later in the text), we will focus on pure optical traps. In the following we explain how superimposed laser beams may be used to trap neutral atoms and to create a periodic potential simultaneously. For a derivation of the following statements see, e.g., Refs. [59, 60, 61, 62].

The functionality of optical traps and lattices can be understood via the AC-Stark shift. For this purpose, different hyperfine states of an atom type (e.g., ^{40}K or ^{6}Li) or selected hyperfine states of different atom types are loaded into a trap with a superimposed magnetic field used to separate the states energetically and used to control the interaction strengths. The trap itself is made of a laser beam with a frequency detuned from a transition into a different hyperfine state. Depending on whether the detuning is into the red (blue), the atoms feel an attractive (repulsive) potential proportional to the intensity of the laser. The effective potential has the form

$$V(\mathbf{x}) \propto I(\mathbf{x}) + B_{\mathrm{eff}}(\mathbf{x})\, m_F \;, \tag{1.1}$$

where $I(\mathbf{x})$ is the intensity of the laser, $B_{\mathrm{eff}}(\mathbf{x})$ is an effective Zeeman term arising from the ellipticity of the beam and m_F is the hyperfine state. A perfectly circularly or linearly polarized beam does not create an effective Zeeman term [59].

A modern strategy for trapping neutral alkali atoms and for simultaneously creating an optical lattice uses both a red and a blue detuned laser. A singly propagating laser creates a potential proportional to the gaussian shape of the laser beam, while a standing beam creates a product of the gaussian shape and a $\cos^2(x/\lambda)$-term. Superimposing, e.g., a red detuned standing beam and a blue detuned singly propagating beam makes the intensities of the gaussian profile (which is used to trap the atoms) and the intensity of the cosine term (used to create the optical lattice) independently tunable. Assuming to have loaded two different hyperfine states/ atom types in the trap leads to the following potential (in good approximation, assuming that the atoms are kept in the trap center)

$$V_\sigma(\mathbf{x}) = \frac{V_{\sigma,\mathrm{per}}}{d} \sum_{i=1}^{d} \cos^2\left(\frac{2\pi x_i}{\lambda}\right) + \mathbf{x} \cdot V_{\sigma,\mathrm{trap}} \cdot \mathbf{x} \;, \tag{1.2}$$

where λ is the wavelength of the red detuned laser, $V_{\sigma,\mathrm{per}}$ the periodic part of the potential and $V_{\sigma,\mathrm{trap}}$ is the trapping part. Both parts may be spin-dependent (but in most cases they are assumed to be spin-independent). The spin-dependence may be caused, e.g., by different atom types or, as mentioned above, by elliptically polarized laser beams. The dimensionality d may be freely chosen between 1 and 3, depending on the number and the configuration of lasers used.

In summary, we have shown what the form of a typical potential, created by laser beams, may be. At this point, it is worth mentioning that in the experiment innumerable additional challenges occur. Just in order to mention a few, for example, a laser frequency with too small detuning from the resonance causes particle loss due to spontaneous emission. The use of a magnetic field may allow additional hyperfine transitions, which may also lead to massive particle loss. Since the detailed experimental realization is not the topic of this thesis, we refer to the literature mentioned above.

1.2.2 Feshbach resonances

An interesting tool for controlling the interaction strengths provided by a superimposed spatially homogeneous magnetic field are Feshbach resonances [6]. At low temperatures the

(i)   (ii)
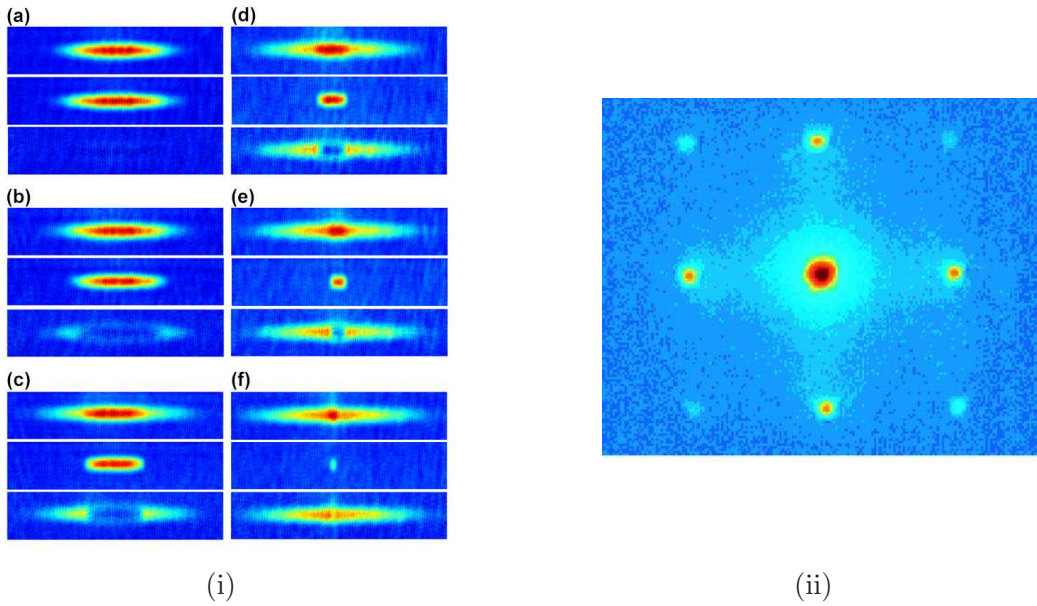
Figure 1.1: Left panel(i): In-situ images of a superfluid two-component Fermi mixure taken from Ref. [17]. From (a) to (f), the spin-imbalance is increased successively. In each part the upper plot shows the particle density of the majority species, the middle plot shows the same for the minority species, and the lower plot shows the resulting magnetization. Right panel(ii): TOF image of a superfluid single-species Bose gas loaded on an optical lattice before. This image has been taken from Ref. [7]. The sharp peaks indicate a strong condensate fraction. The occurrence of more than one peak arises from the mapping from the crystal momentum on the lattice onto the conventional momentum occurring in free expansion.

interaction may be approximated by a contact interaction which depends only on the s-wave scattering length a_s. The interaction takes the form [6, 63, 64]

$$U(\mathbf{x} - \mathbf{y}) = \frac{8\pi\hbar a_s}{m_\uparrow + m_\downarrow}\delta(\mathbf{x} - \mathbf{y}) \tag{1.3}$$

The s-wave scattering length a_s itself is tunable via a Feshbach resonance. We will not explain the mechanism in detail, since this is not a topic of this thesis. For a detailed presentation of the role of Feshbach resonances in ultracold quantum gases we refer to Ref. [65]. The only part we need to know for our purposes is that the s-wave scattering length may be tuned with the help of a magnetic field obeying the formula

$$a_s = a_0 \left(1 - \frac{\Delta B_{\mathrm{el}}}{B - B_{\mathrm{res}}}\right) , \tag{1.4}$$

where a_0 is the scattering length far away from the resonance, B is the strength of the magnetic field superimposed, ΔB_{el} is the width of the area, where a_s has a different sign from a_0 and B_{res} is the position of the resonance. Note that depending on the prior experimental treatment a positive scattering may imply either a repulsive interaction or the existence of a bound molecule state.

1.2.3   Imaging techniques

Finally, besides RF-spectroscopy as a classical method to determine the density of states experimentally, we want to briefly present two imaging techniques used to visualize the shape

of the particle distribution in the atomic cloud. The first technique, which will be mentioned in the following chapters, is in-situ imaging. In this method, the thermalized cloud is interfused by a laser giving a picure of the particle density. Using polarized lasers may be used to visualize different pseudospin species simultaneously. An example taken from the literature is presented in Figure (1.1)(i).

The second method commonly used, especially in order to detect coherent condensates, is the time-of-flight method (TOF). For the purpose of using TOF-imaging the trapping potential and the magnetic field are suddenly turned off. The atomic cloud expands freely and falls into a CCD camera. The time between the release and the detection must be sufficiently long, so that the cloud has a multiple of the size it had at the time of the release. With this method, e.g., the superfluid to Mott-insulating phase transition may be detected for bosons. If a three dimensional system is analyzed with this method, one obtains a picture integrated over the z-axis, of course. A picture obtained with the TOF method is shown in (1.1)(ii).

1.3 Production of a Hubbard model

The potential defined by the laser (1.2) in combination with the inter-particle interaction (1.3) are the ingredients allowing to observe Hubbard model physics in ultracold quantum gases. In second quantization, the full fermionic Hamiltonian in grand canonical form writes

$$\mathcal{H} = \mathcal{H}_1 + \mathcal{H}_2 \tag{1.5}$$

$$\mathcal{H}_1 = \sum_\sigma \int d\mathbf{x}\, \hat{\psi}_\sigma^\dagger(\mathbf{x}) \left(-\frac{\hbar^2}{2m_\sigma} \triangle + V_\sigma(\mathbf{x}) - \mu_\sigma \right) \hat{\psi}_\sigma(\mathbf{x}) \tag{1.6}$$

$$\mathcal{H}_2 = \sum_{\sigma \geq \sigma'} \iint d\mathbf{x}\, d\mathbf{x}'\, \hat{\psi}_\sigma^\dagger(\mathbf{x}) \hat{\psi}_{\sigma'}^\dagger(\mathbf{x}')\, U_{\sigma\sigma'}(\mathbf{x} - \mathbf{x}')\, \hat{\psi}_{\sigma'}(\mathbf{x}') \hat{\psi}_\sigma(\mathbf{x}) \,. \tag{1.7}$$

Assuming that the temperature is sufficiently low, so that the interaction and the trapping term are not too large and that the tight-binding condition

$$V_{\sigma,\text{per}} \gg \frac{2\hbar^2}{m_\sigma \lambda^2} \tag{1.8}$$

is satisfied, one can assume that only the lowest Bloch band is occupied [66]. Expanding the field operators in terms of Wannier-functions gives

$$\hat{\psi}_\sigma(\mathbf{x}) \to \sum_{\mathbf{i}} w_{0,\mathbf{i}\sigma}(\mathbf{x})\, \hat{c}_{\mathbf{i}\sigma} \,, \tag{1.9}$$

where $w_{0,\mathbf{i}\sigma}(\mathbf{x})$ is the Wannier-function in the lowest Bloch band located at the discrete position $\mathbf{i}$, and $\hat{c}_{\mathbf{i}\sigma}$ is the annihilation operator of a fermion located at site $\mathbf{i}$. The discrete lattice sites lie exactly on the minima of the potential $V_{\sigma,\text{per}}(\mathbf{x})$. With the help of this expansion one may rewrite

$$\mathcal{H}_1 \to \sum_{\mathbf{i}\sigma} \epsilon_{\mathbf{i}\sigma} \hat{n}_{\mathbf{i}\sigma} - \sum_{\mathbf{i}\neq\mathbf{j}\,\sigma} t_{\mathbf{i}\mathbf{j}\sigma} \hat{c}_{\mathbf{i}\sigma}^\dagger \hat{c}_{\mathbf{j}\sigma} \tag{1.10}$$

$$\mathcal{H}_2 \to \sum_{\mathbf{i}\mathbf{j}\mathbf{k}\mathbf{l},\, \sigma \geq \sigma'} U_{\mathbf{i}\mathbf{j}\mathbf{k}\mathbf{l}}^{\sigma\sigma'} \hat{c}_{\mathbf{i}\sigma}^\dagger \hat{c}_{\mathbf{j}\sigma'}^\dagger \hat{c}_{\mathbf{k}\sigma'} \hat{c}_{\mathbf{l}\sigma} \,, \tag{1.11}$$

where $\hat{n}_{\mathbf{i}\sigma} = \hat{c}_{\mathbf{i}\sigma}^{\dagger} \hat{c}_{\mathbf{i}\sigma}$ and the relevant model parameters are defined as

$$
\begin{aligned}
\epsilon_{\mathbf{i}\sigma} &\equiv \int d\mathbf{x}\, w_{0,\mathbf{i}\sigma}^{*}(\mathbf{x}) \left(-\frac{\hbar^2}{2m_\sigma} \triangle + V_\sigma(\mathbf{x}) \right) w_{0,\mathbf{i}\sigma}(\mathbf{x}) && (1.12) \\
&\approx \mathbf{i} \cdot V_{\sigma,\mathrm{trap}} \cdot \mathbf{i} - \mu_\sigma \\
t_{\mathbf{ij}\sigma} &\equiv \int d\mathbf{x}\, w_{0,\mathbf{i}\sigma}^{*}(\mathbf{x}) \left(-\frac{\hbar^2}{2m_\sigma} \triangle + V_\sigma(\mathbf{x}) \right) w_{0,\mathbf{j}\sigma}(\mathbf{x}) && (1.13) \\
&\approx t_\sigma \delta_{||\mathbf{i}-\mathbf{j}||,1} \\
U_{\mathbf{ijkl}}^{\sigma\sigma'} &\equiv \iint d\mathbf{x}\, d\mathbf{x}'\, w_{0,\mathbf{i}\sigma}^{*}(\mathbf{x})\, w_{0,\mathbf{j}\sigma'}^{*}(\mathbf{x}')\, U_{\sigma\sigma'}(\mathbf{x}-\mathbf{x}')\, w_{0,\mathbf{k}\sigma'}(\mathbf{x}')\, w_{0,\mathbf{l}\sigma}(\mathbf{x}) && (1.14) \\
&\approx U\, \delta_{\mathbf{ijkl}}\, \delta_{\bar{\sigma}\sigma'} \;.
\end{aligned}
$$

In (1.12) we have used that the trapping potential varies slowly in space and that constant local contributions may be absorbed into the chemical potential. In (1.13) we have again used that the trapping potential varies slowly and we have neglected the overlap between Wannier-functions which are not located at nearest neighboring sites. In (1.12) we have again used that the overlap of the Wannier function is maximal if all four functions carry the same lattice index. Furthermore, we have made use of $U_{\sigma\sigma'}(\mathbf{x}-\mathbf{x}') \propto \delta(\mathbf{x}-\mathbf{x}')$ and the fact that - because of the Pauli blocking - contact potentials act only between particles with different spin index. In summary, when inserting Eqs. (1.12)-(1.14) into the full Hamiltonian (1.5), one obtains the classical spin-asymmetric Hubbard Hamiltonian with a trapping potential,

$$
\mathcal{H}_{\mathrm{Hub}} = -\sum_{(\mathbf{ij})\sigma} t_\sigma \hat{c}_{\mathbf{i}\sigma}^{\dagger} \hat{c}_{\mathbf{j}\sigma} + \sum_{\mathbf{i}\sigma} \left(\mathbf{i} \cdot V_\sigma \cdot \mathbf{i} - \mu_\sigma \right) \hat{n}_{\mathbf{i}\sigma} + U \sum_{\mathbf{i}} \hat{n}_{\mathbf{i}\uparrow} \hat{n}_{\mathbf{i}\downarrow} \;, \tag{1.15}
$$

where $(\dots)$ denotes pairs of sites which are nearest neighbors. In the following chapters we will often assume a spin-independent isotropic trapping potential for simplicity.

At this point it is worth mentioning that, at $V_\sigma = 0$, the Wannier-functions of the lowest Bloch band, created by a potential $V_{\mathrm{per}} \propto \cos^2(\lambda x)$, are represented by solutions of Mathieu-type differential equations [67]. The interesting point here is that these Mathieu-functions are real special functions. Since the influence of the trapping potential on the Wannier-functions is small in our case, we assume that this fact does not change. Having real Wannier functions will be of great importance during this chapter and during the rest of this thesis.

Another interesting point regarding the Wannier-functions is the fact that, if one approximates the minima of the periodic potential harmonically, one finds analytical expressions for U and t_σ. An expansion up to second order in $\mathbf{x}$ yields an exactly solvable harmonic oscillator describing a selected site where the ground state approximates the lowest Bloch band Wannier-function. The simplified overlap integrals yield:

$$
\begin{aligned}
t_\sigma &\propto \xi_\sigma^d \exp(-2\xi_\sigma^2) && (1.16) \\
U &\propto \frac{(\xi_\uparrow \xi_\downarrow)^d}{(\xi_\uparrow^2 + \xi_\downarrow^2)^{\frac{d}{2}}} && (1.17) \\
\xi_\sigma &= \left(\frac{V_{\sigma,\mathrm{per}} m_\sigma \lambda^2}{8\pi^2 \hbar^2} \right)^{\frac{1}{4}} && (1.18)
\end{aligned}
$$

Hence, the depth of the lattice may additionally be used to tune the ratio U/t.

In order to avoid confusion in the following chapters, it is useful to introduce the chemical potential difference $\Delta\mu \equiv \mu_\uparrow - \mu_\downarrow$ and the spin-averaged chemical potential $\mu \equiv (\mu_\uparrow + \mu_\downarrow)/2$ here. Formally, $\Delta\mu$ gives rise to a Zeeman term in the Hamiltonian, but at this point we

emphasize that this term is just used in the grand canonical formalism to control the particle numbers and it has nothing to do with the magnetic field superimposed on the experimental setup which is used to control interaction strengths or, if chosen spatially inhomogeneous, to keep the particles trapped.

Furthermore, note that we have introduced all model parameters which could depend on the internal state of the atom, especially the hopping amplitude t_σ, as spin-dependent basically for completeness. In the following we will assume balanced masses/hopping in most cases, otherwise we will explicitly mention this point.

1.4 Nature of the superfluid order parameters

An ambiguous point in the literature is the functional form of the superfluid order parameter $\Delta(\mathbf{x}) \equiv \langle \hat{\psi}_\downarrow(\mathbf{x})\hat{\psi}_\uparrow(\mathbf{x}) \rangle$ for Fermi-systems. Often the order parameter is treated as a real function for numerical simplicity, or simplified, but complex ansatzes are analyzed. Therefore, in this section we will present physical arguments, which form the superfluid order parameter may have at thermal equilibrium. We first formulate our arguments in a general continuous system, since this is more simple, and then map our results on Hubbard-type models with attractive and repulsive interaction respectively. Furthermore, the definition of the superfluid current and of the corresponding continuity equation is ambiguous. We will clarify this point in this section, too. We start with the treatment of general bosonic systems in order to see the analogies and differences between BEC and fermionic superfluidity (also called pseudo BEC). Then we generalize the bosonic theory to fermionic systems.

1.4.1 Superfluid currents in BECs

A system containing only spinless bosons is described by the Hamiltonian

$$
\begin{aligned}
\mathcal{H} \;=\; & \int d\mathbf{x} \; \hat{\Psi}_{\mathbf{B}}^\dagger(\mathbf{x}) \left(-\frac{\hbar^2}{2m} \triangle + V(\mathbf{x}) \right) \hat{\Psi}_{\mathbf{B}}(\mathbf{x}) \\
+ \; & \iint d\mathbf{x}\,d\mathbf{x}'\, U(\mathbf{x}-\mathbf{x}')\hat{\Psi}_{\mathbf{B}}^\dagger(\mathbf{x})\hat{\Psi}_{\mathbf{B}}^\dagger(\mathbf{x}')\hat{\Psi}_{\mathbf{B}}(\mathbf{x}')\hat{\Psi}_{\mathbf{B}}(\mathbf{x}) \,,
\end{aligned}
\tag{1.19}
$$

where $\hat{\Psi}_{\mathbf{B}}(\mathbf{x})$ $[\hat{\Psi}_{\mathbf{B}}^\dagger(\mathbf{x})]$ destroys [creates] a spinless boson at position $\mathbf{x}$. Depending on the system parameters, the dimensionality, and below a critical temperature T_C it is standard knowledge that Bose-Einstein condensation takes place. The condensate fraction may be described by an anomalous expectation value $\Psi(\mathbf{x}) = \langle \hat{\Psi}_{\mathbf{B}}(\mathbf{x}) \rangle$, where $\langle \cdots \rangle$ is the thermal average at inverse temperature $\beta = 1/k_B T$ [63]. In general $\Psi(\mathbf{x}) \equiv |\Psi(\mathbf{x})| \exp(i\varphi(\mathbf{x}))$ may be a complex function in space, of course. The gradient of the phase $\nabla\varphi(\mathbf{x})$ determines the superfluid velocity of the condensate fraction [63] (a detailed derivation is found in appendix A). If the interaction is not too strong, the superfluid current is described by the phase-gradient of the superfluid order parameter in Bose-Einstein Condensates (BECs) [63].

$$
\mathbf{j} = |\Psi(\mathbf{x})|^2 \, \mathbf{v}(\mathbf{x}), \quad \mathbf{v}(\mathbf{x}) = \frac{\hbar}{m} \nabla\varphi(\mathbf{x}) \,,
\tag{1.20}
$$

where the superfluid order parameter is described by its absolute value and its complex phase $\Psi(\mathbf{x}) = |\Psi(\mathbf{x})| \exp(i\varphi(\mathbf{x})) \equiv \langle \hat{\Psi}_{\mathbf{B}}(\mathbf{x}) \rangle$. This fact highly restricts the motion of the gas. Since $\Psi(\mathbf{x})$ is a well defined function, one obtains

$$
\frac{m}{\hbar} \oint_C d\mathbf{s} \cdot \mathbf{v}(\mathbf{x}) = 2\pi n; \; n \in \mathbb{N} \,,
\tag{1.21}
$$

provided that C is a closed contour. States with $n \neq 0$ must have a singularity in $\varphi(\mathbf{x})$. These singularities are known as quantized vortices and represent excited states carrying energy and angular momentum [63]. In the following we will assume $n = 0$ for all closed contours in our system, leading to a non-singular function $\varphi(\mathbf{x})$ and, hence, to irrotational flow $\nabla \times \mathbf{v}(\mathbf{x}) = 0$.

We define the superfluid density as $\rho(\mathbf{x}) \equiv |\Psi(\mathbf{x})|$. Hence, the continuity equation writes (for not too strong interaction, see appendix A):

$$\frac{\partial}{\partial t}\rho(\mathbf{x}) + \mathbf{j}(\mathbf{x}) \approx 0 \ , \tag{1.22}$$

where (1.22) becomes a strict equality in the interaction-free case. In the following we show, that the use of (1.21) and $n = 0$ leads to a vanishing current density at thermal equilibrium and fixed boundary conditions which imply vanishing currents at the boundary. Fixed boundary conditions are adequate to describe trapped quantum gases, since the trapping potential ensures that there are no particles far away from the trap center. We use an integral in the spirit of a von Neumann-problem in electrostatics:

$$0 = \int_{\partial V} d\mathbf{F} \cdot [\varphi(\mathbf{x})\,\mathbf{j}(\mathbf{x})] = \int_V dV \nabla \cdot [\varphi(\mathbf{x})\,\mathbf{j}(\mathbf{x})] = \int_V dV\,\mathbf{j}(\mathbf{x}) \cdot \nabla\varphi(\mathbf{x}) = \frac{m}{\hbar} \int_V dV \left|\frac{\mathbf{j}(\mathbf{x})}{\Psi(\mathbf{x})}\right|^2 \ . \tag{1.23}$$

Hence, we obtain $\mathbf{v}(\mathbf{x}) = 0 \ \forall \mathbf{x} \in V$ and therefore we may choose $\Psi(\mathbf{x}) \in \mathbb{R} \ \forall \mathbf{x} \in V$. Hence, the motion of the superfluid vanishes at thermal equilibrium in a vortex-free state. In the presence of periodic boundary conditions a stationary current may indeed exist, since the left term in (1.23) does not vanish. If one assumes $n = 0$ the motion of the gas must satisfy:

$$\nabla \times \mathbf{j} = -2\,\mathbf{j} \times \nabla[\ln|\Psi(\mathbf{x})|] \quad \wedge \quad \nabla \cdot \mathbf{j} = 0 \tag{1.24}$$

or alternatively formulated for the velocity instead of the current

$$\nabla \times \mathbf{v}(\mathbf{x}) = 0 \quad \wedge \quad \nabla \cdot \mathbf{v}(\mathbf{x}) = -2\,\mathbf{v}(\mathbf{x}) \cdot \nabla[\ln|\Psi(\mathbf{x})|] \ . \tag{1.25}$$

In the next section we will generalize this statement in a similar way for fermions, which are the topic of interest in this thesis.

1.4.2   Superfluid currents in Fermionic systems

In the literature [68, 69] one often finds the same expression for the superfluid current in fermionic superfluidity as in BECs. The fermionic order parameter is just interpreted as $\hat{\psi}_\downarrow(\mathbf{x})\hat{\psi}_\uparrow(\mathbf{x}) \rightarrow \Psi_{HC}(\mathbf{x})$, in words, as a hard-core bosonic annihilator. The interpretation of $\mathbf{j} = \frac{\hbar}{m}|\Delta(\mathbf{x})|^2\nabla\varphi(\mathbf{x})$, which is often also found in papers or even in text books, is only partially correct. If one neglects the contribution arising from the Hamiltonian's interaction term one does not get a continuity equation in the spirit of (1.22). Instead one obtains (a detailed derivation is found in the appendix A):

$$\frac{\partial}{\partial t}|\Delta(\mathbf{x})|^2 + \nabla \cdot \mathbf{j} = \frac{\hbar}{im}\Delta^*(\mathbf{x})\left[\nabla_\mathbf{x} \cdot \nabla_{\mathbf{x}'}\Delta(\mathbf{x}, \mathbf{x}')\right]_{\mathbf{x}' \rightarrow \mathbf{x}} + \text{h.c.} \ , \tag{1.26}$$

where one has to use the non-diagonal elements $\Delta(\mathbf{x}, \mathbf{x}') = \langle\hat{\psi}_\downarrow(\mathbf{x})\hat{\psi}_\uparrow(\mathbf{x}')\rangle$, which cannot be interpreted as hard-core bosonic expectation value. Hence, an argument leading to an analogon of (1.23) must also use the non-diagonal terms in real-space, which is not the case in the standard expression for the current.

Therefore, we developed a new, generalized concept for the fermionic superfluid current. We introduce the $2d$-dimensional coordinate $\mathbf{y} \equiv (\mathbf{x}, \mathbf{x}')^T$. One obtains, if interaction terms are neglected (detailed motivation is found in appendix A):

$$\frac{\partial}{\partial t}|\Delta(\mathbf{y})|^2 + \nabla_{\mathbf{y}} \cdot \mathbf{j}_S \approx 0 \ , \tag{1.27}$$

where we have defined the $2d$-dimensional "supercurrent" $\mathbf{j}_S \equiv \frac{\hbar}{m}|\Delta(\mathbf{y})|^2 \nabla_{\mathbf{y}} \varphi(\mathbf{y})$ and $\Delta(\mathbf{y}) = |\Delta(\mathbf{y})| \exp[i\varphi(\mathbf{y})]$. It turns out that with this generalized concept one gets indeed the structure of the continuity equation back. The "$\approx$"-symbol in (1.27) arises from neglecting the interaction-part of the Hamiltonian, which can indeed be assumed to be small (see appendix A). In contrast to the bosonic Equation (1.22), one may not choose the system to be interaction-free, since in fermionic systems an attractive interaction is needed in order to obtain superfluidity. As a consequence, we obtain the same structure for the fermionic "supercurrent" in $2d$-dimensions formally as for the bosonic current in d-dimensions, and may therefore apply (1.23) formally, since at the boundary $\mathbf{y} \in \partial V$ the supercurrent must vanish at fixed boundary conditions. (It is sufficient that $\mathbf{x} \vee \mathbf{x}' \in \partial V$.) Hence, we may always choose $\varphi(\mathbf{y}) = 0$, since constant phases may always be gauged away by a global phase rotation, e.g.,

$$\hat{\psi}_{\downarrow}(\mathbf{x}) \to \exp(-i\varphi)\hat{\psi}_{\downarrow}(\mathbf{x}) \quad , \quad \hat{\psi}_{\uparrow}(\mathbf{x}') \to \hat{\psi}_{\uparrow}(\mathbf{x}') \ . \tag{1.28}$$

Note that steady sign changes in $\Delta(\mathbf{y})$ are still allowed, since they do not cause a current to occur. In sum we may therefore restrict our consideration to steady functions $\Delta(\mathbf{y}) \in \mathbb{R} \ \forall \mathbf{y}$. Note again, that sign changes in $\Delta(\mathbf{y})$ are still allowed.

In the literature a common ansatz for FFLO-ordering is [70, 57, 58, 71, 72]

$$\Delta(\mathbf{x}) = |\Delta| \exp(i\,\mathbf{q} \cdot \mathbf{x}) \ , \tag{1.29}$$

leading to a global superfluid current of $\mathbf{j} = \frac{\hbar}{m}|\Delta|^2\mathbf{q}$ in the sense of (1.26), especially for systems with superimposed optical lattices described by a Hubbard-model. Ansatzes of this type seem to work very well in translationally invariant systems with periodic boundary conditions. These translationally invariant results are then often embedded within the LDA [72] in order to describe trapped systems as they are used in actual experiments. These results are not in agreement with the predictions of (1.23). On the other hand, there are numerical calculations beyond LDA, restricting consideration on real order parameters for numerical simplicity [73, 74]. With our prediction (1.23) and with the calculations presented in the following chapters of this thesis we are able to demonstrate that ansatzes of the type of (1.29) are indeed unphysical in trapped systems and we fundamentally agree with the results presented in [73, 74]. We will also present thermodynamically stable complex solutions which may be interpreted as vortex excitations with $n \geq 1$ in the sense of (1.21).

1.4.3 Mass-imbalanced systems

In contrast to electronic systems different pseudospin-species may have different masses in ultracold atomic systems. E.g., "↑" may be interpreted as ^{40}K atoms and "↓" as ^{6}Li atoms. Hence, the kinetic term in the Hamiltonian has to be modified to

$$\mathcal{H}_K \to -\sum_{\sigma} \int d\mathbf{x} \, \frac{\hbar^2}{2m_{\sigma}}\hat{\psi}_{\sigma}^{\dagger}(\mathbf{x}) \triangle \hat{\psi}_{\sigma}(\mathbf{x}) \ . \tag{1.30}$$

This of course leads to modified versions of (1.26) and (1.27). Equation (1.26) does not hold any more and therefore, $\mathbf{j}$ may not be interpreted as a current anymore. There is no simple

generalization like replacing $2m \rightarrow m_\uparrow + m_\downarrow$. The "supercurrent" $\mathbf{j}_S$ needs only to be slightly modified as

$$\mathbf{j}_S \equiv \hbar |\Delta(\mathbf{y})|^2 \, (\mathcal{W} \, \nabla\varphi(\mathbf{y})) \; , \; \mathcal{W} \equiv \mathrm{diag}_{2d \times 2d} \left(\frac{1}{m_\downarrow}, \dots, \frac{1}{m_\downarrow}, \frac{1}{m_\uparrow}, \dots, \frac{1}{m_\uparrow} \right) \; . \qquad (1.31)$$

Since $\mathcal{W}$ is positively definite, Equation (1.23) can also be adopted for mass-imbalanced systems in this sense, so that vortex-free solutions may also be chosen to be real for mass-imbalanced systems.

1.4.4   Strong attraction limit

If the attractive interatomic interaction is strong, the condensation occurring may be understood rather as a BEC of molecules than as BCS superfluid at weak interaction. Under these circumstances the superfluid current indeed takes the bosonic form

$$\mathbf{j} \equiv \frac{\hbar}{m_\uparrow + m_\downarrow} |\Delta(\mathbf{x})|^2 \, \nabla\varphi(\mathbf{x}) \qquad (1.32)$$

in the sense of an effective theory. The effective mass $m_\uparrow + m_\downarrow$ corresponds to the mass of the bosonic molecules in contrast to Eq. (1.26). The expression introduced in (1.32) is found, e.g., in Ref. [69].

1.4.5   Application to Hubbard-type models

As we have shown in section 1.3, superimposing an optical lattice on the experimental setup leads to a simplified lattice Hamiltonian, namely the Hubbard model. The main reason for this is the fact that, if the optical lattice potential is sufficiently deep, only the lowest Bloch-band is occupied. We may express this by expanding the field operators via Wannier-functions as in Eq. (1.9). In the low filling regime only the lowest Bloch-band ($n = 0$) is occupied. Then the superfluid order parameter $\Delta(\mathbf{x}, \mathbf{x}')$ is mapped onto its discrete analogon $\Delta(\mathbf{i}, \mathbf{i}')$, where $\mathbf{i}$ represents a lattice vector, as follows:

$$\Delta(\mathbf{i}, \mathbf{i}') \equiv \langle \hat{c}_{\mathbf{i}\downarrow} \hat{c}_{\mathbf{i}'\uparrow} \rangle = \iint d\mathbf{x} \, d\mathbf{x}' w_{0\mathbf{i}\downarrow}(\mathbf{x}) w_{0\mathbf{i}'\uparrow}(\mathbf{x}') \, \Delta(\mathbf{x}, \mathbf{x}') \; . \qquad (1.33)$$

Since the Wannier-functions of the lowest lying orbital may be chosen to be real (see section 1.3), a real order parameter describing a system in continuous coordinates is automatically mapped onto a real discrete version. Hence, in a trapped system one can apply (1.23), so that the order parameter $\Delta(\mathbf{i}, \mathbf{i}')$ may also be chosen real, if one assumes that there are no vortices in the system. We will prove this statement in the following chapters on numerical examples.

1.4.6   Application to the repulsive-U model

The repulsive-U and the attractive-U Hubbard model are connected via a special particle-hole symmetry in bipartite lattices:

$$\hat{c}^\dagger_{\mathbf{i}\downarrow} \rightarrow (-1)^{\mathbf{i}} \, \hat{c}_{\mathbf{i}\downarrow} \quad , \quad \hat{c}^\dagger_{\mathbf{i}\uparrow} \rightarrow \hat{c}^\dagger_{\mathbf{i}\uparrow} \; , \qquad (1.34)$$

where we define $(-1)^{\mathbf{i}} \equiv -1$ on the A-sublattice and $(-1)^{\mathbf{i}} \equiv +1$ on the B-sublattice. This transformation does not change the kinetic term of the Hubbard Hamiltonian, since hopping takes place only between different sublattices. The numbering-operator of the "down"-spin

species is replaced by the hole-numbering-operator, while the numbering operator of the "up"-spin species remains unchanged.

This special particle-hole transformation leads to the new Hubbard Hamiltonian

$$\mathcal{H} \rightarrow -t \sum_{(\mathbf{ij}),\sigma} \hat{c}_{\mathbf{i}\sigma}^{\dagger} \hat{c}_{\mathbf{j}\sigma} + \sum_{\mathbf{i}\sigma} \left(\sigma V \mathbf{i}^2 - \mu_{\sigma}' \right) \hat{n}_{\mathbf{i}\sigma} - U \sum_{\mathbf{i}} \hat{n}_{\mathbf{i}\uparrow} \hat{n}_{\mathbf{i}\downarrow} + \text{const} , \qquad (1.35)$$

where $\mu_{\uparrow}' = -\mu_{\uparrow}$ and $\mu_{\downarrow}' = \mu_{\downarrow} + U$. The constant term contains no operators and is therefore physically inactive. Hence, the repulsive-U model with a spatially varying chemical potential is equivalent to the attractive-U model with a spatially varying Zeeman term.

The order parameters possibly occurring in both models are mapped onto each other, where the superfluid order parameter corresponds to an xy-antiferromagnetic parameter, and the CDW-order parameter corresponds to a z-antiferromagnetic parameter.

In order to apply the statement found in 1.4.1, we transform the repulsive-U Hubbard model with spatially varying trapping potential to the attractive model with spatially varying Zeeman term. If we assume again that there is no vortex in the system we obtain again the validity of Equation (1.23). Since the Zeeman term becomes large for lattice sites $\mathbf{i}$ far away from the trap center, there is no vacuum at the boundaries in the model after transformation (1.34). Nevertheless, the superfluid current in (1.23) must vanish in the surface-term, since for lattice sites at the boundaries one obtains

$$\langle \hat{n}_{\mathbf{i}\uparrow} \rangle = 0 \quad \text{and} \quad \langle \hat{n}_{\mathbf{i}\downarrow} \rangle = 1 , \qquad (1.36)$$

causing the outer region of the trap to be described by nearly pure states

$$|\mathbf{i}_{\partial V}\rangle = \hat{c}_{\downarrow}^{\dagger} |0\rangle \quad \Rightarrow \quad \Delta(\mathbf{i}) = \langle \hat{c}_{\mathbf{i}\uparrow} \hat{c}_{\mathbf{i}\downarrow} \rangle = 0 \quad \forall \mathbf{i} \in \partial V . \qquad (1.37)$$

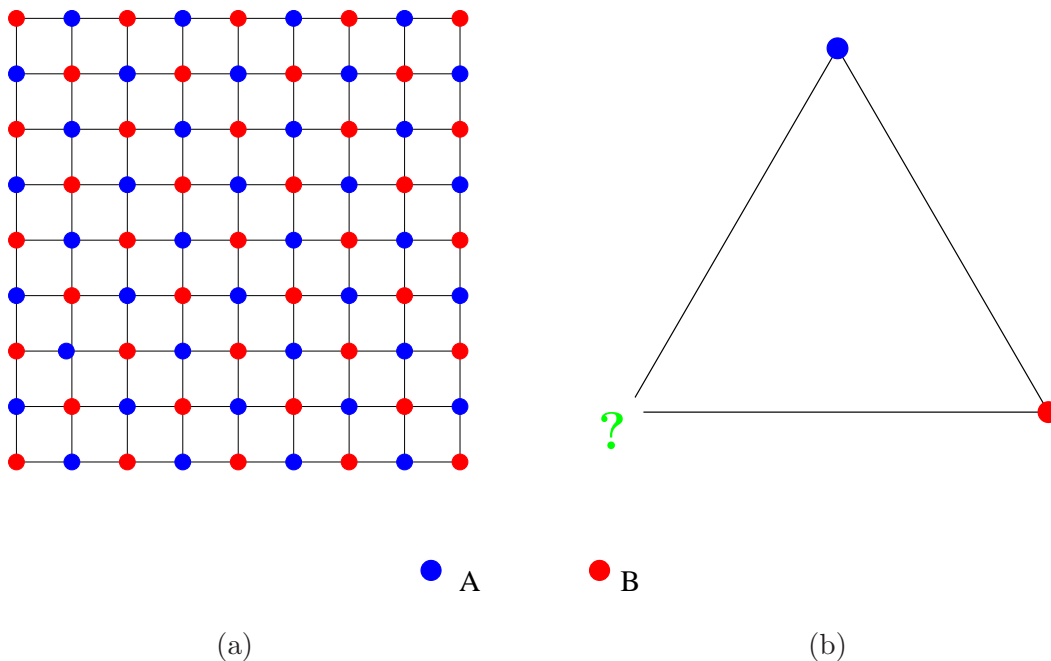Figure 1.2: Bipartite lattice versus non-bipartite lattice. (a) Example of a bipartite lattice: the square lattice. Superfluidity and antiferromagnetism may occur depending on the sign of the interaction. (b) Example of a non-bipartite lattice: The triangular lattice. While superfluidity is allowed in the attractive-U case the lattice is frustrated. Therefore long-ranged antiferromagnetism may not occur.

Spin comp.	$U > 0$	$U < 0$	Quantity
$\tilde{S}_1$	$\frac{1}{2}(-1)^{\mathbf{i}}\langle \hat{c}^{\dagger}_{\mathbf{i}\uparrow}\hat{c}_{\mathbf{i}\downarrow} + \hat{c}^{\dagger}_{\mathbf{i}\downarrow}\hat{c}_{\mathbf{i}\uparrow}\rangle$	$\frac{1}{2}\langle \hat{c}_{\mathbf{i}\uparrow}\hat{c}_{\mathbf{i}\downarrow} + \hat{c}^{\dagger}_{\mathbf{i}\downarrow}\hat{c}^{\dagger}_{\mathbf{i}\uparrow}\rangle$	$\mathfrak{Re}(\Delta)$
$\tilde{S}_2$	$\frac{i}{2}(-1)^{\mathbf{i}}\langle \hat{c}^{\dagger}_{\mathbf{i}\uparrow}\hat{c}_{\mathbf{i}\downarrow} - \hat{c}^{\dagger}_{\mathbf{i}\downarrow}\hat{c}_{\mathbf{i}\uparrow}\rangle$	$-\frac{i}{2}\langle \hat{c}_{\mathbf{i}\uparrow}\hat{c}_{\mathbf{i}\downarrow} - \hat{c}^{\dagger}_{\mathbf{i}\downarrow}\hat{c}^{\dagger}_{\mathbf{i}\uparrow}\rangle$	$\mathfrak{Im}(\Delta)$
$\tilde{S}_3$	$\frac{1}{2}(-1)^{\mathbf{i}}\langle \hat{n}_{\mathbf{i}\uparrow} - \hat{n}_{\mathbf{i}\downarrow}\rangle$	$\frac{1}{2}(-1)^{\mathbf{i}}\langle \hat{n}_{\mathbf{i}\uparrow} + \hat{n}_{\mathbf{i}\downarrow} - 1\rangle$	s

Table 1.1: Spatial components of the staggered magnetization in the repulsive model and their corresponding quantities in the attractive model, where s is the staggered density parameter of the CDW phase.

Hence, the current vanishes at the boundaries leading to a real order parameter in the transformed model. Transforming the Hamiltonian (1.35) back to the repulsive model leads to a staggered spin order parameter parallelly to a unique vector in the xy-plane according to Table 1.1.

In a balanced ($\mu_\uparrow = \mu_\downarrow$) system with repulsive U, the Hamiltonian is invariant under any spin-rotation leading to an effective SU(2)-symmetry. If one assumes an incommensurate phase lying, e.g., in the xz-plane, this could be rotated onto an incommensurate phase in the xy-plane. This would be in contrast with our statement that xy-antiferromagnetism must occur parallelly to a globally defined direction. Therefore, the spins are strictly aligned parallelly to a globally defined direction (affecting also the z-component, which was unaffected in the general case). We will readdress the results of this subsection in later numerical calculations.

Chapter 2

Translationally Invariant Systems

In order to understand trapped systems, it is useful to review translationally invariant systems first, which have been analyzed intensively during the last decades. Therefore, in this chapter, we present some basic results which are helpful in understanding the properties of trapped ultracold fermionic quantum gases. We explain the basic properties of the Hubbard Hamiltonian and some exact results within the saddle-point (Hartree-Fock) approximation. We introduce the phases which may occur in different parameter regions, especially when a system is spin imbalanced or away from half filling. Finally, we explain how the local density approximation (LDA) is used to obtain results for trapped systems on the basis of translationally invariant ones. In our work we did not use the LDA, but the LDA is used various times in the literature nevertheless. Hence, we introduce this method in order to show in later chapters why the LDA fails to describe trapped systems in a broad parameter region and especially in describing the results obtained in this work[1].

2.1 The interaction-free Hubbard model

For a better understanding of the Hubbard-model with interaction it is useful to discuss the exactly solvable Hubbard Hamiltonian without interaction ($U = 0$) first. For the translationally invariant case in the grand canonical ensemble the model Hamiltonian [see, e.g., Eq. (1.15)] simply reads

$$\mathcal{H} = -t \sum_{(\mathbf{ij}),\sigma} \hat{c}_{\mathbf{i}\sigma}^{\dagger} \hat{c}_{\mathbf{j}\sigma} - \sum_{\mathbf{i}\sigma} \mu_{\sigma} \hat{n}_{\mathbf{i}\sigma} \; . \tag{2.1}$$

The diagonalization of this simple tight-binding Hamiltonian may be done via a Fourier-transformation from real-space to $\mathbf{k}$-space (crystal momentum) on a hypercubic lattice [75]

$$c_{\mathbf{k}\sigma}^{\dagger} = \frac{1}{\sqrt{\mathcal{N}}} \sum_{\mathbf{i}} \exp(-i\,\mathbf{k}\cdot\mathbf{i})c_{\mathbf{i}\sigma}^{\dagger} \quad ; \quad c_{\mathbf{k}\sigma} = \frac{1}{\sqrt{\mathcal{N}}} \sum_{\mathbf{i}} \exp(i\,\mathbf{k}\cdot\mathbf{i})c_{\mathbf{i}\sigma} \quad , \tag{2.2}$$

where $\mathcal{N}$ is the total number of lattice sites. After the transformation the Hamiltonian (2.1) in d dimensions is diagonalized as

$$\mathcal{H} = \sum_{\mathbf{k}\sigma} \left[\varepsilon(\mathbf{k}) - \mu_{\sigma} \right] \hat{n}_{\mathbf{k}\sigma} \; , \; \varepsilon(\mathbf{k}) \equiv -2t \sum_{i=1}^{d} \cos(k_i) \; . \tag{2.3}$$

---

[1]Selected parts of this chapter have been published in T. Gottwald and P. G. J. van Dongen, Eur. Phys. J. B **61**, 277 (2008).
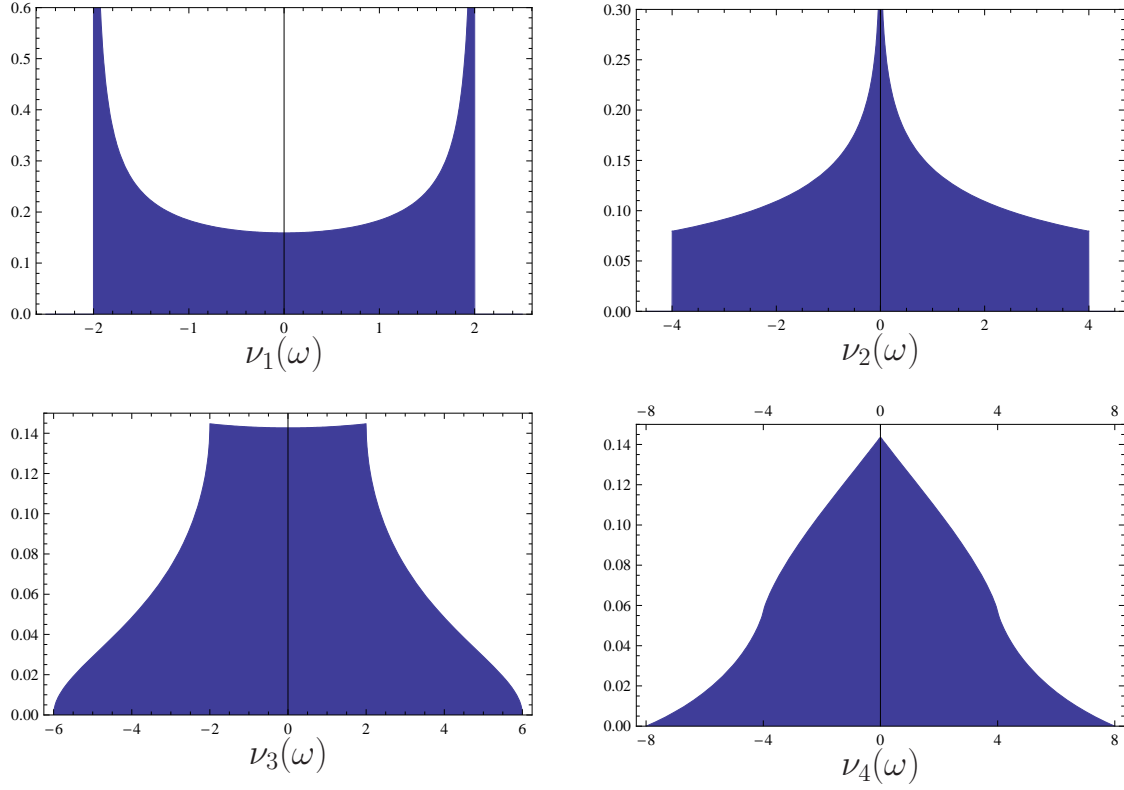
Figure 2.1: Interaction-free DOS $\nu_d(\omega)$ of the Hubbard model between one and four dimensions in units of t. The DOSs are nonzero for $|\omega| \leq W = 2dt$, where W is the half bandwidth. The van-Hove singularities have the exponent $d/2 - 1$ (multiplied with logarithmic functions at some positions for even d) and lie at even (odd) integer positions of ω for even (odd) dimensionality.

For further progress it is useful to introduce the d-dimensional density of states (DOS), especially when working in the thermodynamical limit (infinite spatial extention of the system), since Hamiltonian (2.3) does not depend on $\mathbf{k}$ explicitly.

$$\nu_d(\omega) \equiv \frac{1}{\mathcal{N}} \sum_{\mathbf{k}} \delta\left[\omega - \varepsilon(\mathbf{k})\right] \xrightarrow[\text{lim}]{\text{TD}} \frac{1}{(2\pi)^d} \int d\mathbf{k}\, \delta\left[\omega - \varepsilon(\mathbf{k})\right] \ , \tag{2.4}$$

With the help of the DOS d-dimensional $\mathbf{k}$-integrals can be reduced to one-dimensional ω-integrals. The DOSs in d-dimensions may be generally expressed analytically via Bessel functions as follows (see, e.g., [76, 77])

$$\nu_d(\omega) = \frac{1}{2\pi} \int_0^\infty dx\, [J_0(x)]^d \cos\left(\frac{\omega x}{2}\right) \ . \tag{2.5}$$

The DOSs for $d = 1 - 4$ are presented in Figure (2.1).

With the help of the interaction-free DOS, calculations for the translationally invariant Hubbard model may be drastically simplified in their numerical evaluation, as we shall see in the following sections.

2.2 Physical motivation for ordering types

In this section we just want to give the reader some physical intuition for the possible phases occurring in the Hubbard model starting from the following simple argument. The basic Hubbard Hamiltonian reads, when including interaction and assuming half filling (chemical potential not shown) as follows:

$$\mathcal{H} = -t \sum_{(\mathbf{ij}),\sigma} \hat{c}_{\mathbf{i}\sigma}^\dagger \hat{c}_{\mathbf{j}\sigma} + U \sum_{\mathbf{i}} \hat{n}_{\mathbf{i}\uparrow} \hat{n}_{\mathbf{i}\downarrow} \ . \tag{2.6}$$

At $U = 0$ we have presented the interaction-free model above. This model is diagonal in $\mathbf{k}$-space and at half filling each lattice site is singly occupied. In the interaction-free case one obtains for the double occupancy

$$\langle \hat{n}_{\mathbf{i}\uparrow} \hat{n}_{\mathbf{i}\downarrow} \rangle = \frac{1}{4} \ \forall \ \mathbf{i} \ , \tag{2.7}$$

since the spin-species are uncorrelated. The inclusion of an interaction, $U > 0$ ($U < 0$) tends to decrease (increase) the double occupancies. Of course, the interaction term is diagonal in real-space and not in $\mathbf{k}$-space. In the ground-state both non-commuting terms have to be minimized together. In the thermodynamical limit this can lead to spontaneous symmetry breaking. For $U > 0$ and $t = 0$ (no kinetic terms) the ground-state is achieved by having exactly one fermion per site regardless which spin-orientation the particle has, e.g. a ferromagnet with all spins in "↑" position would be such a configuration. On the other hand the ferromagnet does by no means minimize the kinetic term. The competition of both terms may lead to an antiferromagnetic state minimizing the sum of both terms occurring in the Hamiltonian (2.6). A similarly simple argument suggests that the ground state at $U < 0$ is a superfluid state, a charge density wave (CDW) or a mixture of both.

2.3 The Hubbard model at weak coupling

One may use the saddle-point approximation, in order to analyze antiferromagnetic ($U > 0$) or superfluid ($U < 0$) phases at weak coupling. Since the attractive and the repulsive case are equivalent in a translationally invariant system (see section 1.4.6), it basically suffices to treat one of both cases. Therefore, we always show our statements for one of both cases. Since existing literature treats $U > 0$ and $U < 0$ as well, we switch between both, in order to avoid redundant statements.

Generally, in order to perform calculations at weak coupling, one has to decouple the interaction term. In this chapter we restrict consideration to a first order expansion in U. In chapter 5 we show the effects arising when including terms of the order U^2. In first order of perturbation theory, the interaction is split into two parts, namely the Hartree- and the Fock-terms [78]

$$\mathcal{H}_U \quad = \quad U \, \hat{n}_{\mathbf{i}\uparrow} \hat{n}_{\mathbf{i}\downarrow} \rightarrow \mathcal{H}_H + \mathcal{H}_F \tag{2.8}$$

$$\mathcal{H}_H \quad = \quad U \left(\langle \hat{n}_{\mathbf{i}\uparrow} \rangle \hat{n}_{\mathbf{i}\downarrow} + \langle \hat{n}_{\mathbf{i}\downarrow} \rangle \hat{n}_{\mathbf{i}\uparrow} - \langle \hat{n}_{\mathbf{i}\uparrow} \rangle \langle \hat{n}_{\mathbf{i}\downarrow} \rangle \right) \tag{2.9}$$

$$\mathcal{H}_F \quad = \quad U \left(\langle \hat{c}_{\mathbf{i}\uparrow}^\dagger \hat{c}_{\mathbf{i}\downarrow} \rangle \hat{c}_{\mathbf{i}\downarrow}^\dagger \hat{c}_{\mathbf{i}\uparrow} + \hat{c}_{\mathbf{i}\uparrow}^\dagger \hat{c}_{\mathbf{i}\downarrow} \langle \hat{c}_{\mathbf{i}\downarrow}^\dagger \hat{c}_{\mathbf{i}\uparrow} \rangle - \langle \hat{c}_{\mathbf{i}\uparrow}^\dagger \hat{c}_{\mathbf{i}\downarrow} \rangle \langle \hat{c}_{\mathbf{i}\downarrow}^\dagger \hat{c}_{\mathbf{i}\uparrow} \rangle \right) \ , \ (U > 0) \tag{2.10}$$

$$\mathcal{H}_F \quad = \quad U \left(\langle \hat{c}_{\mathbf{i}\uparrow}^\dagger \hat{c}_{\mathbf{i}\downarrow}^\dagger \rangle \hat{c}_{\mathbf{i}\downarrow} \hat{c}_{\mathbf{i}\uparrow} + \hat{c}_{\mathbf{i}\uparrow}^\dagger \hat{c}_{\mathbf{i}\downarrow}^\dagger \langle \hat{c}_{\mathbf{i}\downarrow} \hat{c}_{\mathbf{i}\uparrow} \rangle - \langle \hat{c}_{\mathbf{i}\uparrow}^\dagger \hat{c}_{\mathbf{i}\downarrow}^\dagger \rangle \langle \hat{c}_{\mathbf{i}\downarrow} \hat{c}_{\mathbf{i}\uparrow} \rangle \right) \ , \ (U < 0) \ . \tag{2.11}$$

Hence, the Hartree-terms may cause z-antiferromagnetism or charge-density waves (CDW), respectively, while the Fock-terms may cause xy-antiferromagnetism or superfluidity, respectively. The thermal averages $\langle \cdots \rangle$ have, of course, to be determined self-consistently. In the thermodynamical limit ($\mathcal{N} \rightarrow \infty$), a self-consistent treatment via numerics fails, if no assumptions about the structure of these quantities are made, since the number of lattice sites is infinite.

In this thesis, the most important feature of the repulsive Hubbard model is antiferromagnetism, which is equivalent to CDW- and superfluid states in the attractive model. At half filling ($\mu_\uparrow = \mu_\downarrow = U/2$, exactly one particle per site) it is mathematically exactly shown that an antiferromagnet is the ground state of the balanced Hubbard mean field model at $U > 0$ [79]. In order to calculate the order parameter, one may assume, e.g., a z-antiferromagnet with the ansatz

$$\langle \hat{n}_{\mathbf{i}\sigma} \rangle = \frac{1}{2} \left[1 + (-1)^{\mathbf{i}} \, m\sigma \right] \, , \, m \in [-1, +1] \, , \tag{2.12}$$

where m is the order parameter describing the staggered magnetization in z-direction and $(-1)^{\mathbf{i}}$ is $+1$ if $\mathbf{i}$ is on the A-sublattice and -1 if $\mathbf{i}$ is on the B-sublattice. The order obtained in (2.12) may be rotated in any direction and may be afterwards transformed to the attractive balanced model at half filling, leading to a charge density wave (CDW) or to a superfluid state with a uniformly defined gap called Bardeen-Cooper-Schrieffer (BCS) state [see Table (1.1)]. Putting Eq. (2.12) in the Hartree-Fock Hamiltonian, makes a simple diagonalization possible via a Fourier-transformation and a subsequent Bogoliubov-transformation in $\mathbf{k}$-space. An alternative solution is the direct diagonalization in real-space. For systems away from half filling or for systems including a Zeeman term, there are no exact statements as performed in Ref. [79]. Incommensurate states are predicted for the repulsive case [80]. These are equivalent to the Fulde-Ferrel-Larkin-Ovchinnikov (FFLO) [81, 82] states in the attractive model. In the following, we will present calculations done in $\mathbf{k}$-space found in the literature and compare them to calculations done in real-space within this work.

2.3.1   Formalism in k-space

A usual way for treating the attractive Hubbard model at weak coupling is found in Refs. [83, 70, 72, 84, 85]. In this approach, the particle densities are assumed to be constant and the order parameter is assumed to be a plane wave

$$n_{\mathbf{i}\sigma} \rightarrow n_\sigma \, , \tag{2.13}$$

$$\Delta(\mathbf{i}) \rightarrow |\Delta| \exp(i\mathbf{q} \cdot \mathbf{i}) \, . \tag{2.14}$$

This ansatz leads to the Hamiltonian (after Fourier-transformation to $\mathbf{k}$-space):

$$\begin{aligned}
\mathcal{H} \quad \rightarrow \quad & \sum_{\mathbf{k}} \left\{ [\varepsilon(\mathbf{k}) - \tilde{\mu}_\uparrow] \, \hat{c}^\dagger_{\mathbf{k}\uparrow} \hat{c}_{\mathbf{k}\downarrow} + [\varepsilon(\mathbf{k}) - \tilde{\mu}_\downarrow] \, \hat{c}^\dagger_{\mathbf{k}\downarrow} \hat{c}_{\mathbf{k}\downarrow} \right. \\
+ \quad & \left. U|\Delta| \left[\hat{c}^\dagger_{\mathbf{q/2}+\mathbf{k},\uparrow} \hat{c}^\dagger_{\mathbf{q/2}-\mathbf{k},\downarrow} + \hat{c}_{\mathbf{q/2}-\mathbf{k},\downarrow} \hat{c}_{\mathbf{q/2}+\mathbf{k},\uparrow} \right] - U \left(|\Delta|^2 + n_\uparrow n_\downarrow \right) \right\} \, .
\end{aligned} \tag{2.15}$$

The operator-like terms of $\mathcal{H}_H$ have been included in the effective chemical potentials $\tilde{\mu}_\sigma \equiv \mu_\sigma + U n_{\bar{\sigma}}$. This step is only possible if the occupation numbers are assumed to be constant and if one is interested rather in calculations at fixed particle numbers than in calculations at fixed chemical potentials. However, the authors of Ref. [83] neglect the term "$n_\uparrow n_\downarrow$" in their calculation for some unknown reason. Defining the following quantities leads analytically to

a diagonal form of the Hamiltonian (via a Bogoliubov transformation):

$$
E_{\mathbf{k},\mathbf{q},\pm} \equiv \frac{\tilde{\mu}_\downarrow - \tilde{\mu}_\uparrow}{2} + \frac{\varepsilon(\mathbf{k} + \frac{\mathbf{q}}{2}) - \varepsilon(-\mathbf{k} + \frac{\mathbf{q}}{2})}{2} \tag{2.16}
$$

$$
\pm \sqrt{\left(\frac{\varepsilon(\mathbf{k} + \frac{\mathbf{q}}{2}) + \varepsilon(-\mathbf{k} + \frac{\mathbf{q}}{2})}{2} - \frac{\tilde{\mu}_\downarrow + \tilde{\mu}_\uparrow}{2}\right)^2 + (U|\Delta|)^2} \; ,
$$

$$
u_{\mathbf{k},\mathbf{q}}^2 \equiv \frac{1}{2}\left(1 + \frac{\xi_{\mathbf{k},\mathbf{q}}}{\sqrt{\xi_{\mathbf{k},\mathbf{q}}^2 + (U|\Delta|)^2}}\right) \; , \tag{2.17}
$$

$$
v_{\mathbf{k},\mathbf{q}}^2 \equiv \frac{1}{2}\left(1 - \frac{\xi_{\mathbf{k},\mathbf{q}}}{\sqrt{\xi_{\mathbf{k},\mathbf{q}}^2 + (U|\Delta|)^2}}\right) \; , \tag{2.18}
$$

$$
u_{\mathbf{k},\mathbf{q}} v_{\mathbf{k},\mathbf{q}} \equiv \frac{U|\Delta|}{2\sqrt{\xi_{\mathbf{k},\mathbf{q}}^2 + (U|\Delta|)^2}} \; . \tag{2.19}
$$

The Hamiltonian (2.15) is diagonalized via the coefficients $u_{\mathbf{k},\mathbf{q}}$ and $v_{\mathbf{k},\mathbf{q}}$ of the matrix

$$
\mathcal{U} = \begin{pmatrix} u_{\mathbf{k},\mathbf{q}} & v_{\mathbf{k},\mathbf{q}} \\ -v_{\mathbf{k},\mathbf{q}} & u_{\mathbf{k},\mathbf{q}} \end{pmatrix} \quad ; \quad \begin{pmatrix} \hat{c}_{\mathbf{k}+\mathbf{q}/\mathbf{2},\uparrow} \\ \hat{c}_{-\mathbf{k}+\mathbf{q}/\mathbf{2},\downarrow}^\dagger \end{pmatrix} = \mathcal{U} \begin{pmatrix} \hat{\gamma}_{\mathbf{k},\mathbf{q},+} \\ \hat{\gamma}_{\mathbf{k},\mathbf{q},-}^\dagger \end{pmatrix} \tag{2.20}
$$

and, furthermore, we define

$$
\xi_{\mathbf{k},\mathbf{q}} \equiv \frac{\varepsilon(\mathbf{k} + \frac{\mathbf{q}}{2}) + \varepsilon(-\mathbf{k} + \frac{\mathbf{q}}{2}) - \tilde{\mu}_\uparrow - \tilde{\mu}_\downarrow}{2} \; . \tag{2.21}
$$

The diagonalized Hamiltonian takes the form ($n_\uparrow n_\downarrow$-term neglegted according to Ref. [83])

$$
\mathcal{H}_{\mathrm{DIAG}} = \sum_{\mathbf{k},\lambda=\pm} \lambda E_{\mathbf{k},\mathbf{q},\lambda} \hat{\gamma}_{\mathbf{k},\mathbf{q},\lambda}^\dagger \hat{\gamma}_{\mathbf{k},\mathbf{q},\lambda} + \sum_{\mathbf{k}} \left[E_{\mathbf{k},\mathbf{q},-} + \varepsilon\left(-\mathbf{k} + \frac{\mathbf{q}}{2}\right) - \tilde{\mu}_\downarrow - U|\Delta|^2\right] \; . \tag{2.22}
$$

The self-consistency equation for the superfluid order parameter reads

$$
|\Delta| = \frac{U|\Delta|}{\mathcal{N}} \sum_{\mathbf{k}} \frac{f_\beta(E_{\mathbf{k},\mathbf{q},-}) - f_\beta(E_{\mathbf{k},\mathbf{q},+})}{2\sqrt{\xi_{\mathbf{k},\mathbf{q}}^2 + (U|\Delta|)^2}} \; , \tag{2.23}
$$

where $f_\beta(x)$ is the Fermi function at inverse temperature β. Of course, the normal phase $\Delta = 0$ is always a solution. Since the particle numbers are absorbed in the chemical potentials one does not have to obtain them self-consistently. They are determined as

$$
n_\sigma = \frac{1}{\mathcal{N}} \sum_{\mathbf{k}} u_{\mathbf{k},\mathbf{q}}^2 f_\beta(\sigma E_{\mathbf{k},\mathbf{q},\sigma}) + v_{\mathbf{k},\mathbf{q}}^2 f_\beta(\sigma E_{\mathbf{k},\mathbf{q},-\sigma}) \; , \tag{2.24}
$$

where σ has to be evaluated as $\uparrow \equiv +$ and $\downarrow \equiv -$ and Equation (2.24) may be used to determine the chemical potentials. With this formalism, for fixed n_σ and β, one may search for the solution minimizing the Helmholtz-free energy. Within this procedure one has to scan values of $\mathbf{q}$, which is usually chosen parallelly to the x-direction (strictly speaking this is only allowed for rotationally invariant dispersion relations $\varepsilon(\mathbf{k})$, but the error is assumed to be small). Choosing $\mathbf{q} \neq \mathbf{0}$ does not allow the self-consistency equations to be simplified with the help of the non-interacting DOS, as it is the case for $\mathbf{q} = \mathbf{0}$. One has to perform d-dimensional summation or integration over $\mathbf{k}$, depending on whether one is interested in finite or infinite sized systems.

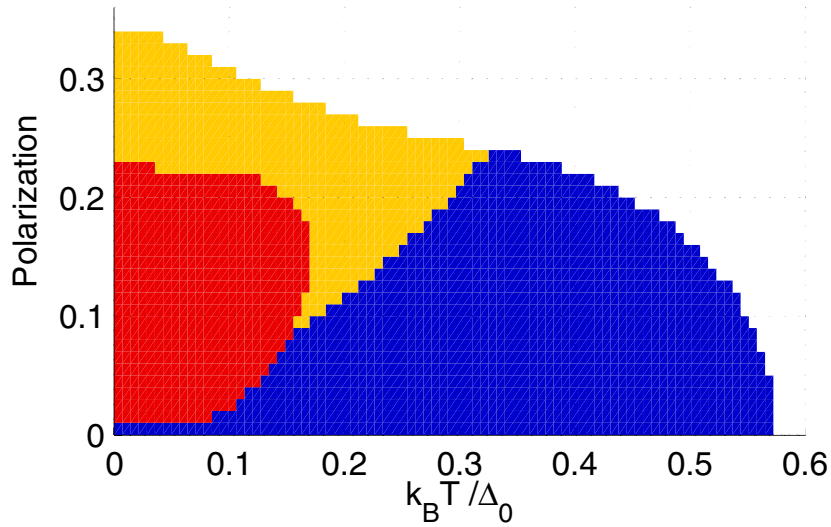The phase diagram of the Hamiltonian (2.15) is shown in Figure (2.2). Four different phases are found:

Figure 2.2: Phase diagram of the FFLO mean-field Hubbard Hamiltonian at half filling taken from Ref. [70]. The blue area indicates the breached pair (BP) phase (BCS in the balanced system), the red area the phase-separated (PS) state, the yellow area the FFLO-phase and white indicates the normal phase. Since this phase diagram is obtained by numerical sampling in the T/P-plane (with Δ_0 being the size of the BCS-gap at $T = 0$ and $P = 0$), the boundaries of the phases appear serrated due to finite computational resources.

- The normal phase described by a vanishing order parameter $\Delta(\mathbf{i}) = 0$.

- The BP-phase described by a real and positive order parameter. At vanishing magnetization (called polarization in the plot), this phase corresponds to the standard BCS-phase. Note that at non-vanishing magnetization, this phase cannot occur in the ground state or at sufficiently low temperatures ($T \ll U\Delta_0$, where $U\Delta_0$ is the BCS-gap of the unmagnetized system in the ground state).

- The FFLO-state, which is characterized by $|\Delta| \neq 0$ and $\mathbf{q} \neq \mathbf{0}$.

- The phase-separated state consists of spatial regions with a normal phase and of a region with a BCS-phase. Note that this phase cannot occur at fixed chemical potentials. It occurs, when there are no chemical potentials μ_σ leading to the given fixed particle numbers. Due to the canceling of degeneracies due to the harmonic potential in trapped systems, we do not have to consider this phase any more in the sense it is treated here.

The results obtained in Ref. [70] can be used to make predictions for trapped systems within the LDA, as explained later in this chapter. Especially finding the role of the FFLO-state in trapped systems within an exact treatment of the trapping potential is one key issue of this thesis.

2.3.2   Formalism in real-space

The Bogoliubov-de Gennes formalism, used to treat spatially inhomogeneous systems beyond LDA, may, of course, also be used to treat translationally invariant system (program explained
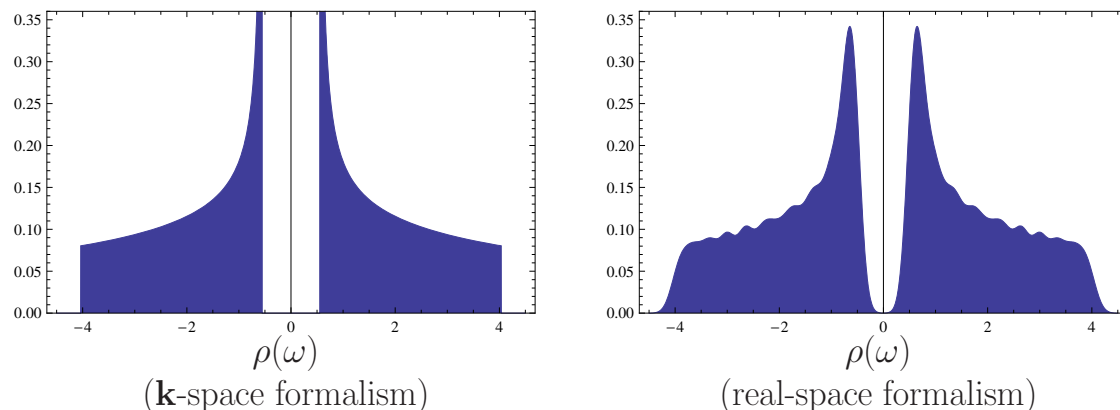
Figure 2.3: Comparison of the DOS of a BCS-state obtained within **k**-space formalism to the DOS obtained within real-space formalism on a 30×30 lattice for a half-filled spin-balanced system at $U = -2.4$ and $\beta = 15$ in units of t. The real-space DOS has been obtained according to formula (3.15) with $\sigma = 0.2$. While the van Hove-singularities diverge with an exponent of $-1/2$ in the left panel, there is a sharp maximum in the right one. The gap is smeared out in the real-space formalism and the carrier of the DOS is qualitatively the same.

in the appendix C). In this section, we treat a translationally invariant system at attractive U with periodic boundaries in the real-space formalism in order to compare the results to the ones obtained in the **k**-space formalism. The advantage of the real-space formalism is that there are no assumptions made on the structure of the parameters $n_{\mathbf{i}\sigma}$ and $\Delta(\mathbf{i})$. In real-space, the mean-field Hamiltonian at attractive interaction is given as:

$$
\begin{aligned}
\mathcal{H} &= -t \sum_{(\mathbf{ij}),\sigma} \hat{c}_{\mathbf{i}\sigma}^{\dagger} \hat{c}_{\mathbf{j}\sigma} + \sum_{\mathbf{i}\sigma} \left(U \langle \hat{n}_{\mathbf{i}\bar{\sigma}} \rangle - \mu_{\sigma} \right) \hat{n}_{\mathbf{i}\sigma} \\
&+ U \sum_{\mathbf{i}} \left(\Delta(\mathbf{i}) \hat{c}_{\mathbf{i}\uparrow}^{\dagger} \hat{c}_{\mathbf{i}\downarrow}^{\dagger} + \Delta^{*}(\mathbf{i}) \hat{c}_{\mathbf{i}\downarrow} \hat{c}_{\mathbf{i}\uparrow} - |\Delta(\mathbf{i})|^{2} - \langle \hat{n}_{\mathbf{i}\uparrow} \rangle \langle \hat{n}_{\mathbf{i}\downarrow} \rangle \right) ,
\end{aligned}
\tag{2.25}
$$

with $\Delta(\mathbf{i}) \equiv \langle \hat{c}_{\mathbf{i}\downarrow} \hat{c}_{\mathbf{i}\uparrow} \rangle$. At this point, we use the formalism explained later in chapter 3. The symmetries and further properties of this matrix formalism are explained there, since that chapter contains the more important results of this thesis. Here, we perform just a comparison to results found in the literature in order to show that **k**-space+LDA formalism is not very well adequate to describe trapped systems treated extensively in this thesis in chapter 3.

The first result we present here is the comparison of a spin-balanced system at half filling treated once in **k**-formalism for infinite extension and treated in real-space formalism in Figure (2.3). Qualitatively the DOSs obtained in both formalisms are mainly the same. The symmetry and the BCS-gap are present in both panels. The van Hove singularities are replaced by maxima in the real-space version. The real-space version predicts the same structure of the order parameter (after a special particle-hole transformation) as the exactly known result (2.12). From this point of view the real-space formalism seems to be a good approximation to systems in the thermodynamical limit.

Of course, it is of interest to compare the results for the FFLO-state presented above to states obtained in the real-space formalism. As explained above, a typical ansatz for the FFLO phase is $\Delta(\mathbf{i}) = |\Delta| \exp(i\mathbf{q} \cdot \mathbf{i})$. Putting such an ansatz in a real-space iteration does not lead to a complex solution for $\Delta(\mathbf{i})$, unfortunately. Nevertheless, it is possible to realize FFLO-states within this formalism. Therefore, we perform a unitary transformation based on the idea that one can always choose $\Delta(\mathbf{i})$ to be real by choosing a complex hopping amplitude
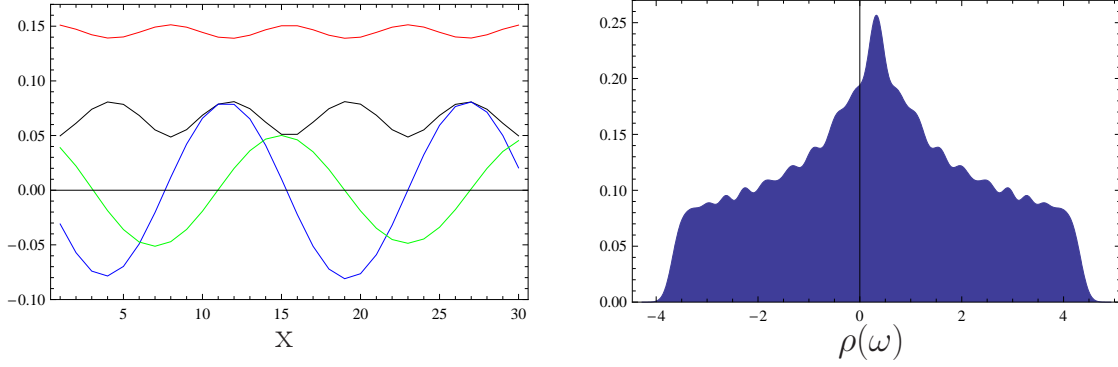
Figure 2.4: Left panel: magnetization (red), real part (blue) imaginary part (green) and absolute value (black) of the superfluid order parameter in an FFLO-state obtained in the real-space formalism. The system parameters are chosen to be $U = -2.4$, $\mu = -1.2$, $\Delta\mu = 1.4$ and $\beta = 15$ in units of t. The size of the square lattice is 30×30 and the boundaries are periodic. Right panel DOS of the system presented in the left panel.

in the Hamiltonian. Assuming to have a complex solution $\Delta(\mathbf{i}) = |\Delta(\mathbf{i})| \exp[i\varphi(\mathbf{i})]$, one can transform

$$
\begin{aligned}
\hat{c}_{\mathbf{i}\uparrow} &\rightarrow \hat{c}_{\mathbf{i}\uparrow} \\
\hat{c}_{\mathbf{i}\downarrow} &\rightarrow \exp[-i\,\varphi(\mathbf{i})]\,\hat{c}_{\mathbf{i}\downarrow} \ .
\end{aligned}
\tag{2.26}
$$

This leads directly to the modified Hamiltonian

$$
\begin{aligned}
\mathcal{H} \ \rightarrow \ &- \sum_{(\mathbf{ij}),\sigma} t\Big(\delta_{\sigma\uparrow} + \delta_{\sigma\downarrow} \exp\{i[\varphi(\mathbf{i}) - \varphi(\mathbf{j})]\}\Big)\hat{c}^{\dagger}_{\mathbf{i}\sigma}\hat{c}_{\mathbf{j}\sigma} + \sum_{\mathbf{i}\sigma} \Big(U\langle\hat{n}_{\mathbf{i}\bar\sigma}\rangle - \mu_{\sigma}\Big)\hat{n}_{\mathbf{i}\sigma} \\
&+ \ U\sum_{\mathbf{i}} \Big[|\Delta(\mathbf{i})|\Big(\hat{c}^{\dagger}_{\mathbf{i}\uparrow}\hat{c}^{\dagger}_{\mathbf{i}\downarrow} + \hat{c}_{\mathbf{i}\downarrow}\hat{c}_{\mathbf{i}\uparrow}\Big) - |\Delta(\mathbf{i})|^2 - \langle\hat{n}_{\mathbf{i}\uparrow}\rangle\langle\hat{n}_{\mathbf{i}\downarrow}\rangle\Big] \ .
\end{aligned}
\tag{2.27}
$$

Since the phase shift is constant for the simple plain wave FFLO-ansatz, we simply use a constant (non $\mathbf{i}$- or $\mathbf{j}$-dependent) complex hopping amplitude for one spin-species and a real and positive one for the other in order to obtain convergence. After convergence, the phase is transformed back to $\Delta(\mathbf{i})$.

A typical FFLO-state obtained in the real-space formalism is presented in Figure (2.4). It turns out that the magnetization $m_{\mathbf{i}} \equiv \langle\hat{n}_{\mathbf{i}\uparrow} - \hat{n}_{\mathbf{i}\downarrow}\rangle$ and the real and imaginary parts of the order parameter appear to be $\mathbf{i}$-dependent. The total particle density depends only weakly on $\mathbf{i}$. Remarkably, the solution obtained does not necessarily have the same FFLO-vector $\mathbf{q}$ as originally put into the transformation (2.26). Numerically, it depends on the phase of the "$\downarrow$"-hopping amplitude whether one obtains a solution or not. Regardless whether the FFLO-vector $\mathbf{q}$ is commensurate with the lattice size or not, one may obtain a converging solution of the form presented in Figure (2.4). Trying different $\mathbf{q}$-values leads either to the same physical results or to bad convergence behavior. We cannot establish a rule predicting a priori whether convergence occurs or not.

The DOS of the FFLO state presented in Figure (2.4) does not have a visible gap. Since the DOS of a finite size system is discrete and the continuous form has been reached by artificial broadening [see formula (3.15)], we cannot determine whether a gap exists or not.

A comparison between the **k**-space and the real-space formalism yields the following similarities:

- If a particle imbalance is turned on, one may obtain an inhomogeneous wave-like oscillating order parameter which we identify with the FFLO-state in the real-space formalism.

- The absolute value of the order parameter is decreased down to a value of $\sim 25\%$ to the value of the balanced system with the same parameters.

The following differences are found:

- The magnetization shows an oscillatory behavior, too, with half the wavelength of the superfluid order parameter.

- The order parameter does not obey $\Delta(\mathbf{i}) = |\Delta| \exp(i\mathbf{q} \cdot \mathbf{i})$. A rule similar to $\Delta(\mathbf{i}) = \alpha \cos(\mathbf{q} \cdot \mathbf{i}) + i\gamma \sin(\mathbf{q} \cdot \mathbf{i})$, $\alpha \neq \gamma$, seems to be valid instead.

- A consequence of the previous issue is that the absolute value oscillates with the same wavelength as the magnetization, i.e., $|\Delta(\mathbf{i})| \neq$ const.

- Since the system presented in Figure (2.4) is half filled, there are states with the same grand potential with an oscillating total particle density (CDW) and superfluidity. The wavelength of the oscillating total particle density would be the same as the one of $\Delta(\mathbf{i})$, i.e., the double of the wavelength of the magnetization.

In summary, we may conclude that the structure of an FFLO-state differs from the results obtained in the **k**-space formalism, since there are no assumptions made on the structure of $n_{\mathbf{i}\sigma}$ and $\Delta(\mathbf{i})$. Of course, it is an open question whether the differences shown are physical or an effect of the finite size of the system. Since the focus of this work does not lie on translationally invariant systems, we stop further argumentation at this point. The results found here have been demonstrated first in order to show that one has to be careful with ansatz-solutions and second since we intend to use these results to highlight difficulties with the LDA-approach presented later in this chapter.

2.3.3 Role of the boundary conditions

In classical solid state physics, where the Hubbard model has been discussed since 1963, it is common praxis to assume periodic boundary conditions, as we have done above in this chapter. In fact, in the thermodynamical limit, the boundary conditions do not play a role at all. In the context of ultracold quantum gases, however, the systems do have a small size. For the purpose of treating experimentally realistic systems, one has to include the harmonic trapping potential, as discussed later in this thesis. Nevertheless, in this chapter the trapping potential has been neglected so far. Hence, we want to study the difference between systems with fixed and periodic boundary conditions with special emphasis on BCS- and FFLO-phases.

In Figure (2.5) results for a balanced system at half filling are shown. Here, the symmetry breaking is of BCS type, of course. For periodic boundary conditions the superfluid order parameter is a constant, since in the BCS-phase at periodic boundary conditions each lattice site is equivalent. For fixed boundary conditions lattice sites are not equivalent in general. The nearer the lattice site is to the boundary, the higher the order parameter is. It is maximal at the corner positions. Heuristically, this may be explained by the fact that due to the missing neighboring lattice sites the effective U/t value is higher at the boundary (three neighbors
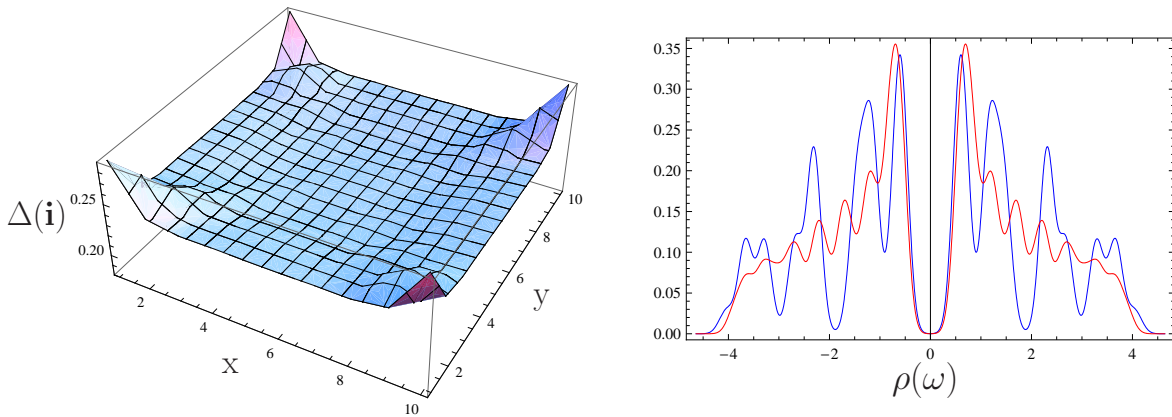
Figure 2.5: Left panel: superfluid order parameter on a small (10×10) square lattice with fixed boundary conditions. The system parameters are $U = -2.4$ and $\beta = 100$ in units of t. The system is half filled and spin balanced. Right panel DOS of the system presented in the left panel (red) and DOS of a system with the same parameters but periodic boundary conditions (blue). The order parameter at periodic boundaries is constant and, therefore, not shown.

instead of four) and even higher in the corners (two neighbors). The amplitude of the order parameter in the middle of the system at fixed boundaries corresponds approximatively to the constant one and periodic boundaries. This fact is also shown in the same shape of the gap in the two DOSs. The DOS at fixed boundaries is smeared out away from the Fermi edge in contrast to the one at periodic boundaries, since switching to fixed boundaries cancels degeneracies existing in the completely translationally invariant system.

In summary, the physics of the small 10×10 system does not depend strongly on the boundary conditions at half filling and spin-balance. This is completely different for an FFLO-state as presented in Figure (2.4). Turning off rapidly or smoothly (e.g., by lowering the hopping over the boundaries during the iteration steps) leads to the loss of the FFLO-phase. Either one ends up in a normal system or the iteration cycle does not converge, at least in all the calculations we have tried regarding this topic. We view this point as an confirmation of the result found in section 1.4.5, namely that the order parameter is a real function of **i** at fixed boundaries, if no vortices are present in the system. We did not search for real wave-like solutions in systems without trapping potential. Real solutions for systems with the experimentally relevant trapping potentials are shown in chapter 3. Since, if the trapping potential is turned on, systems with repulsive interaction strength cannot be simply mapped onto systems with attractive interaction, as it is the case in this chapter, we treat the case $U > 0$ in chapter 4 separately.

2.3.4   Spin-dependent hopping

A slightly different solution emerges, if hopping is spin-dependent ($t \rightarrow t_\sigma$, e.g., $t_\uparrow > t_\downarrow$). The basic difference arising, if $U = 0$, is that away from half filling an imbalance occurs even at $\mu_\uparrow = \mu_\downarrow$. If filling is higher than half, the "$\downarrow$"-spins represent the majority species, while, if filling is lower than half, the magnetization has the opposite sign. If one turns on an attractive interaction at high filling, assumes a constant real $\Delta(\mathbf{i})$ and constant $n_{\mathbf{i}\sigma}$ and proceeds analogously to section 2.3.1, one may find a real order parameter coexisting with a
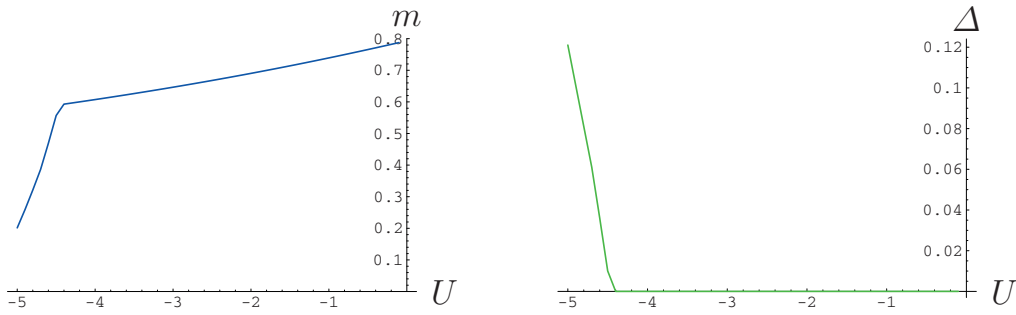
Figure 2.6: Magnetization and superfluid order parameter in a translationally invariant system in the ground state as a function of U. The particle number has been fixed to $n \equiv \frac{1}{2}(n_\uparrow + n_\downarrow) \approx 0.18$ and the hopping amplitudes are $t_\uparrow = 1$ and $t_\downarrow = 0.5$. This figure has been published also in Ref. [86].

non-zero magnetization in the ground state. Results are shown in Figure (2.6). Nevertheless, we are more interested in trapped systems and will therefore discuss spin-dependent hopping more extensively in chapters 3 and 4.

2.4 Trapping potentials and LDA

A treatment of a physical situation requires the inclusion of the trapping potential in the Hamiltonian, which reads in the most general form

$$\mathcal{H}_V = \sum_{\mathbf{i}\sigma} V_\sigma(\mathbf{i})\, \hat{n}_{\mathbf{i}\sigma} \ . \tag{2.28}$$

In this thesis, we restrict consideration to harmonic spin-independent potentials $V_\sigma(\mathbf{i}) = V\mathbf{i}^2$. There are basically two ways to treat the harmonic potential. First, one may treat the potential exactly within the real-space formalism used above and discussed extensively in chapters 3 and 4. Here, the treatment of the space dependent potential is natural in the sense that the local chemical potential $\mu_\sigma(\mathbf{i}) \equiv \mu_\sigma - V(\mathbf{i})$ is treated exactly anyway. A second way to treat the trapping potential is the LDA [or sometimes called Thomas Fermi approximation (TFA)]. In the LDA one assumes the trapping potential to vary slowly in real-space with the consequent assumption that each lattice site behaves as a translationally invariant system with the constant chemical potential

$$\mu_{\sigma,\mathrm{LDA}} \equiv \mu_\sigma(\mathbf{i}) \ . \tag{2.29}$$

Hence, the trapped system with $\mathcal{N}$ lattice sites is mapped on $\mathcal{N}$ independent translationally invariant systems. Each single problem is then solved, e.g., with the $\mathbf{k}$-space formalism presented above. After solving the $\mathcal{N}$ independent problems, the trapped system is reconstructed as a mosaic of translationally invariant systems. In this way especially the sizes $n_{\mathbf{i}\sigma}$ and $\Delta(\mathbf{i})$ (or $S_{\mathbf{i}+}$ for repulsive attraction strengths) are calculated.

The LDA is a satisfactory method for the description of unordered phases as the paramagnetic metallic phase and the paramagnetic Mott-insulator [30, 28]. There are no qualitative differences in the results between the exact and the LDA calculations. When describing systems with broken symmetries, however, the following problems are immediately obvious:

- It is not clear which type of lattice size has to be used for the calculation of the $\mathcal{N}$ independent lattice sizes. There are basically three variants: Systems with infinite extension, the size $\mathcal{N}$ of the full problem or the typical extension of the region of the phase occurring. Different sizes are used in the literature, but a priori there is no evidence which one describes the system best.

- In most cases, the single translationally invariant problems are treated within **k**-space formalism, as explained above, with constant occupation numbers $n_{\mathbf{i}\sigma} \to n_\sigma$. There is no stringent reason for using this formalism. Using the real-space formalism presented above predicts **i**-dependent occupation numbers although the system is translationally invariant. Hence, it is not clear which of those numbers has to be put in the LDA-solution at the end of the algorithm.

- As the last point, the **i**-dependence enters the LDA via $\mu_\sigma(\mathbf{i})$. Hence, an explicit dependence on **i** (for fixed $|\mathbf{i}|$) is a priori not possible in the LDA. Hence, all the quantities predicted in the LDA appear as $n[\mu(\mathbf{i})] \equiv n(|\mathbf{i}|)$ instead of $n(\mathbf{i})$.

For these reasons, one can say a priori that the use of the LDA is problematic, when treating superfluid or antiferromagnetic systems. In fact, these problems will be confirmed in the following chapters where we present results taking exactly into account the trapping potential.

Chapter 3

Trapped Superfluid Fermi-Mixtures

In this chapter we analyze the properties of ultracold Fermi mixtures on optical lattices at attractive interaction strengths. As emphasized in chapter 1 the relevant Hubbard Hamiltonian may be written as:

$$\mathcal{H} = -t \sum_{(\mathbf{ij}),\sigma} \hat{c}^\dagger_{\mathbf{i}\sigma} \hat{c}_{\mathbf{j}\sigma} + \sum_{\mathbf{i}\sigma} (\mathbf{i} \cdot V \cdot \mathbf{i} - \mu_\sigma)\, \hat{n}_{\mathbf{i}\sigma} + U \sum_{\mathbf{i}} \hat{n}_{\mathbf{i}\uparrow} \hat{n}_{\mathbf{i}\downarrow} \ . \tag{3.1}$$

For the sake of completeness, we first reproduce results for balanced systems, which are already well understood in the literature. Then we present results for imbalanced systems first with real and afterwards with complex order parameters. We present the thermodynamically stable solutions for these systems and show the role of vortices in complex solutions. Although the Hartree terms of the interaction are often neglected in the literature [73, 74], we show that they play an important role for the description of trapped systems. We compare calculations retaining with calculations neglecting those terms. Furthermore, we present results with spin-dependent hopping, which may be a physically relevant, e.g., if the masses of the pseudospin-species are unequal. As the last point of this chapter we present LDA-results taken from the literature and we compare them to our results obtained by exactly treating the trapping potential in order to test the quality of the frequently used LDA-approximation.

3.1 The saddle-point approximation

Since it is a major goal of this thesis to understand the phase diagram and especially the spatial structure of the superfluid order parameter $\Delta(\mathbf{i})$ of the model (3.1), which was not well understood until now, we treat this model within the saddle-point approximation. As explained in chapter 2, the saddle-point approximation defines a good starting point for the description of fermionic superfluidity. We decompose the interaction-term as follows:

$$\hat{n}_{\mathbf{i}\uparrow} \hat{n}_{\mathbf{i}\downarrow} \to \langle \hat{n}_{\mathbf{i}\uparrow} \rangle \hat{n}_{\mathbf{i}\downarrow} + \langle \hat{n}_{\mathbf{i}\downarrow} \rangle \hat{n}_{\mathbf{i}\uparrow} - \langle \hat{n}_{\mathbf{i}\uparrow} \rangle \langle \hat{n}_{\mathbf{i}\downarrow} \rangle + \Delta(\mathbf{i}) \hat{c}^\dagger_{\mathbf{i}\uparrow} \hat{c}^\dagger_{\mathbf{i}\downarrow} + \Delta^*(\mathbf{i}) \hat{c}_{\mathbf{i}\downarrow} \hat{c}_{\mathbf{i}\uparrow} - |\Delta(\mathbf{i})|^2 \ , \tag{3.2}$$

where $\langle \ldots \rangle$ denotes the thermal average at inverse temperature $\beta \equiv 1/k_B T$ and $\Delta(\mathbf{i}) \equiv \langle \hat{c}_{\mathbf{i}\downarrow} \hat{c}_{\mathbf{i}\uparrow} \rangle$. The values of $\langle \hat{n}_{\mathbf{i}\sigma} \rangle$ and $\Delta(\mathbf{i})$ are obviously not a priori known and have to be determined self-consistently. In order to do this, we rewrite the saddle-point version of the Hamiltonian (3.1) in a matrix form as follows:

$$\mathcal{H} = \begin{pmatrix} \hat{\mathbf{c}}^\dagger_\uparrow \\ \hat{\mathbf{c}}_\downarrow \end{pmatrix}^T_{2\mathcal{N}} \begin{pmatrix} H_{0\uparrow} & \boldsymbol{\Delta} \\ \boldsymbol{\Delta}^* & -H_{0\downarrow} \end{pmatrix}_{2\mathcal{N} \times 2\mathcal{N}} \begin{pmatrix} \hat{\mathbf{c}}_\uparrow \\ \hat{\mathbf{c}}^\dagger_\downarrow \end{pmatrix}_{2\mathcal{N}} \ , \tag{3.3}$$

where we have defined the $\mathcal{N}$-dimensional vectors

$$
\hat{\mathbf{c}}_{\sigma} \equiv \begin{pmatrix} \hat{\mathbf{c}}_{1\sigma} \\ \vdots \\ \hat{\mathbf{c}}_{\mathcal{N}\sigma} \end{pmatrix} \quad , \quad \hat{\mathbf{c}}_{\sigma}^{\dagger} \equiv \begin{pmatrix} \hat{\mathbf{c}}_{1\sigma}^{\dagger} \\ \vdots \\ \hat{\mathbf{c}}_{\mathcal{N}\sigma}^{\dagger} \end{pmatrix} \quad , \tag{3.4}
$$

with lattice sites described by scalar numbers rather then vectors. The $\mathcal{N} \times \mathcal{N}$-matrices $H_{0\sigma}$ and $\mathbf{\Delta}$ are defined as

$$
\begin{aligned}
H_{0\sigma,ij} &\equiv \delta_{ij}\left(\lambda U \langle \hat{n}_{i\bar{\sigma}} \rangle - \mu_{\sigma} + V_i\right) - \left(\delta_{||i-j||,1} + \xi \delta_{ij,\mathrm{B}}\right) t \quad \text{and} \tag{3.5} \\
\mathbf{\Delta}_{ij} &\equiv U \delta_{ij} \Delta(i) , \tag{3.6}
\end{aligned}
$$

where $\delta_{||i-j||=1}$ is 1 if i and j are nearest neighbors and 0 otherwise and $\delta_{ij,\mathrm{B}}$ is 1 if i and j are connected over the system boundaries and 0 otherwise. The parameter $0 \le \lambda \le 1$ is used to control the Hartree term contribution and ξ is used to set the boundary conditions ($\xi = 0$: fixed, $\xi = 1$: periodic).

Hence, it suffices to diagonalize the matrix appearing in (3.3) numerically. The thermal averages $\langle \hat{n}_{\mathbf{i}\sigma} \rangle$ and $\Delta(\mathbf{i})$ are determined as:

$$
\langle \hat{n}_{\mathbf{i}\sigma} \rangle = \sum_{s=1}^{2\mathcal{N}} |u_{\mathbf{i}s,\sigma}|^2 f_{\beta}(\sigma E_s) \tag{3.7}
$$

$$
\Delta(\mathbf{i}) = \sum_{s=1}^{2\mathcal{N}} u_{\mathbf{i}s,\uparrow} u_{\mathbf{i}s,\downarrow}^* f_{\beta}(E_s) , \tag{3.8}
$$

where $f_{\beta}(x) \equiv [1 + \exp(\beta x)]^{-1}$ is the Fermi function, $u_{\mathbf{i}s,\sigma}$ are the components of the unitary transformation diagonalizing the matrix in (3.3) and E_s is the s-th eigenvalue of (3.3). Furthermore, σ is interpreted as $\uparrow \equiv +$ and $\downarrow \equiv -$. Of course, the quantities in (3.7) and (3.8) have to be determined self-consistently (a brief description of the program doing so is found in the appendix (C)). An evaluation of (3.7) and (3.8) always yields values which are physically accessible. Since a hermitian matrix can always be diagonalized by a unitary matrix and $0 \le f_{\beta}(x) \le 1$ it follows that

$$
\sum_{s=1}^{2\mathcal{N}} |u_{\mathbf{i}s,\sigma}|^2 = 1 \quad \Rightarrow \quad 0 \le \langle \hat{n}_{\mathbf{i}\sigma} \rangle \le 1 , \tag{3.9}
$$

and it immediately follows (derivation found in (B.1))

$$
\sum_{s=1}^{2\mathcal{N}} u_{\mathbf{i}s,\uparrow} u_{\mathbf{i}s,\downarrow}^* = 0 \quad \Rightarrow \quad |\Delta(\mathbf{i})| \le \frac{1}{2} . \tag{3.10}
$$

This property is independent of the parameters in the Hamiltonian matrix in $\mathcal{H}$.

3.1.1   Different solution types

In this real-space representation, the average values $n_{\mathbf{i}\sigma} \equiv \langle \hat{n}_{\mathbf{i}\sigma} \rangle$ and $\Delta(\mathbf{i})$ have to be determined self-consistently. At first we address the question whether there is one unique solution for fixed parameters. In $d \ge 3$ under certain assumptions (see chapter (2)) we have been able to show that there are exactly two different solutions for translationally invariant systems.

The situation will appear to be more complicated if the trapping potential V is included exactly.

Equation (3.8) is obviously trivially solved if one assumes $\Delta(\mathbf{i}) = 0 \,\forall\, \mathbf{i}$, since the matrix (3.3) becomes block-diagonal in this case, and therefore also the unitary transformation, diagonalizing it, is block-diagonal. The consequence is that in the sum (3.8) we have $u_{\mathbf{i}s,\uparrow} = 0$ or $u_{\mathbf{i}s,\downarrow} = 0$ so that the complete sum vanishes and, hence, this self-consistency equation is trivially fulfilled. This scenario describes the normal phase of the gas, and competing superfluid phases have to be compared with it energetically in order to determine the thermodynamically stable phase.

An reduction of complexity of the superfluid phase is brought on by the assumption of a real superfluid order parameter $\Delta(\mathbf{i}) = \Delta^*(\mathbf{i})$. In this case, the unitary transformation diagonalizing Hamiltonian (3.3) is orthogonal, and, therefore, (3.8) is trivially fulfilled in its imaginary part. As a consequence, it is obviously simpler to obtain real solutions for $\Delta(\mathbf{i})$ numerically. As we showed in Equation (1.22) for systems with a trapping potential, it suffices to analyze real order parameters, for the special case of vortex-free solutions.

3.1.2 Symmetries of the Hamiltonian

In order to understand the possible phases occurring in trapped Fermi gases, it is essential to understand the symmetry properties of Hamiltonian (3.3). The first basic symmetry that may occur is the symmetry of the spectrum. If one assumes $\Delta\mu \equiv \mu_\uparrow - \mu_\downarrow = 0$ and $n_{\mathbf{i}\uparrow} = n_{\mathbf{i}\downarrow}$, Hamiltonian (3.3) is a matrix of the form:

$$\mathcal{H} = \begin{pmatrix} \mathcal{A} & \mathcal{B}^* \\ \mathcal{B} & -\mathcal{A} \end{pmatrix}, \tag{3.11}$$

with $\mathcal{A}^\dagger = \mathcal{A} = \mathcal{A}^T$ and $\mathcal{B}^T = \mathcal{B}$. Since the matrix (3.11) is similar to

$$\mathcal{H}' = \begin{pmatrix} 0 & \mathbb{1} \\ -\mathbb{1} & 0 \end{pmatrix} \mathcal{H} \begin{pmatrix} 0 & -\mathbb{1} \\ \mathbb{1} & 0 \end{pmatrix} = \begin{pmatrix} -\mathcal{A} & -\mathcal{B} \\ -\mathcal{B}^* & \mathcal{A} \end{pmatrix}, \tag{3.12}$$

we get from the eigenenergy condition $\det(\mathcal{H} - \omega\mathbb{1}) = 0$

$$0 = \det(\mathcal{H} - \omega\mathbb{1}) = \begin{vmatrix} \mathcal{A} - \omega\mathbb{1} & \mathcal{B}^* \\ \mathcal{B} & -\mathcal{A} - \omega\mathbb{1} \end{vmatrix} = \begin{vmatrix} -\mathcal{A} - \omega\mathbb{1} & -\mathcal{B} \\ -\mathcal{B}^* & \mathcal{A} - \omega\mathbb{1} \end{vmatrix} \tag{3.13}$$

$$= (-1)^{2\mathcal{N}} \begin{vmatrix} \mathcal{A} + \omega\mathbb{1} & \mathcal{B} \\ \mathcal{B}^* & -\mathcal{A} + \omega\mathbb{1} \end{vmatrix} = \begin{vmatrix} \mathcal{A} + \omega\mathbb{1} & \mathcal{B}^* \\ \mathcal{B} & -\mathcal{A} + \omega\mathbb{1} \end{vmatrix} = \det(\mathcal{H} + \omega\mathbb{1}).$$

Hence, the spectrum is symmetric in this case, irrespective of the details of the solution. If one turns on the particle number imbalance $\mu_\uparrow \neq \mu_\downarrow$, this symmetry is lost. However, if one neglects the Hartree terms in the saddle-point approximation, as the authors of [73] and [74] have done, the spectrum is just shifted by $\Delta\mu/2 = (\mu_\uparrow - \mu_\downarrow)/2$. In this case, Hamiltonian (3.11) may be rewritten as

$$\mathcal{H} \to \mathcal{H} + \frac{\Delta\mu}{2}\mathbb{1}, \tag{3.14}$$

leading just to a shift $\omega \to \omega - \Delta\mu/2$. If the Hartree terms are included, this symmetry is completely lost in the imbalanced case, since they induce a space-dependent Zeeman term, which is not diagonal in the sense of (3.11).

A further symmetry property is the symmetry of the underlying lattice and the external potential. Both the lattice and the external potential are symmetric under $\pi/2$ rotations

(a)   (b)
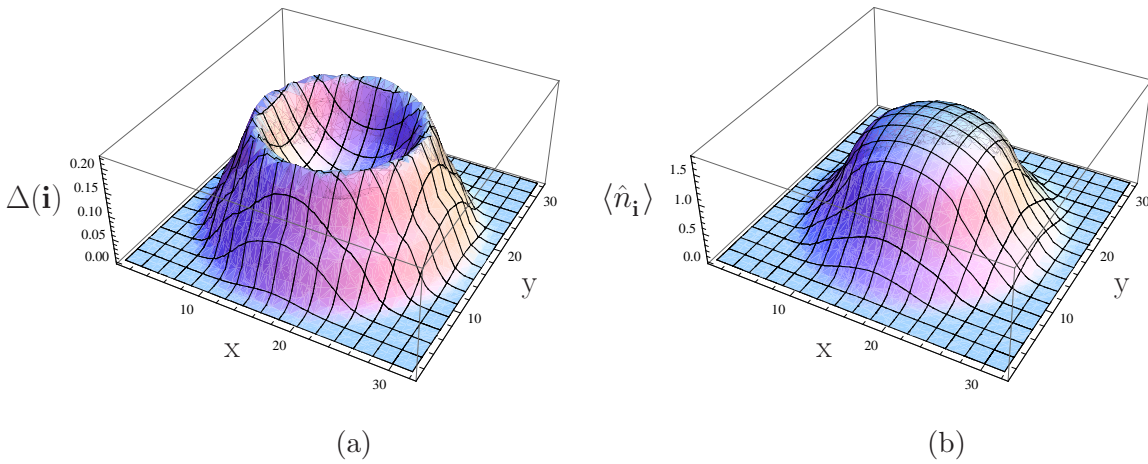
Figure 3.1: Superfluid order parameter $\Delta(\mathbf{i})$ and particle density $\langle \hat{n}_{\mathbf{i}} \rangle$ on a 32×32 square lattice in the high-filling regime. The system parameters are chosen to be $U = -2.5$, $V = 0.025$, $\mu = 0.5$ and $\beta = 1000$ in units of t.

around the z-axis of the system in real-space. A priori, one would also expect the observables $n_\sigma(\mathbf{i})$ and $|\Delta(\mathbf{i})|$ to have those symmetries. As we will find later in numerical calculations, this symmetry may become spontaneously broken.

If one turns the interaction off ($U = 0$), all eigenstates obviously respect the rotational symmetry of the trapping potential. A priori, one would expect the same if the interaction was turned on ($U < 0$). As we will see in the following section, this is not necessarily true, in particular in a system with a spin-imbalance.

3.2 Solutions with real order parameter

The results of this section are obtained under the explicit assumption that the superfluid order parameter is real. We show solutions for both balanced and unbalanced systems as well. The values of the trapping parameters are chosen such as to yield a realistic description of the typical experimental conditions.

3.2.1 Balanced systems

Balanced systems ($\Delta\mu = 0$) have been discussed in the literature (e.g. in [73]). For translationally invariant systems, it is believed that the order parameter $\Delta(\mathbf{i})$ can without loss of generality be chosen to be a real positive number which does not depend on $\mathbf{i}$. We show some results for trapped balanced systems in Figures (3.1)-(3.3). For trapped systems, assuming a real order parameter, it is also believed that the order parameter can be chosen to be a positive number. This is confirmed by our numerical results.
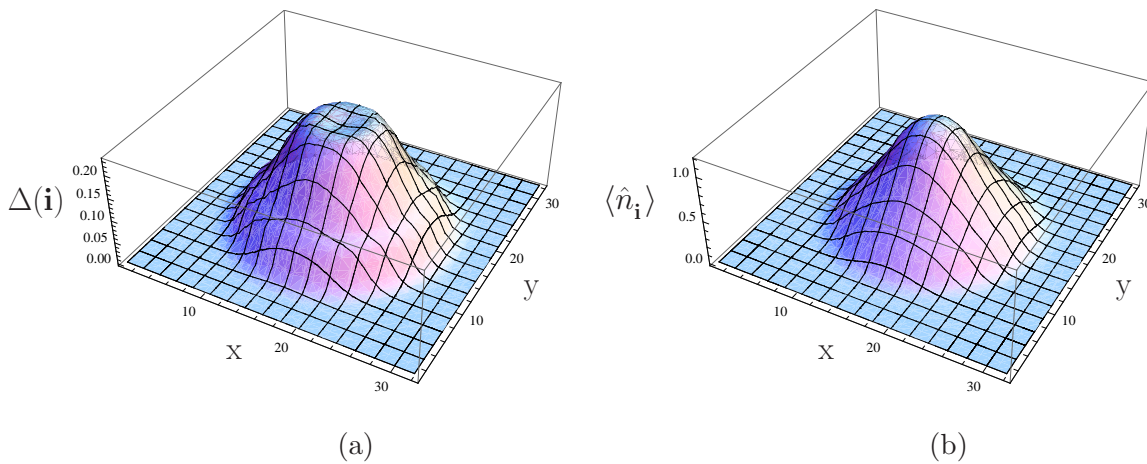
(a)   (b)

Figure 3.2: Superfluid order parameter $\Delta(\mathbf{i})$ and particle density $\langle \hat{n}_\mathbf{i} \rangle$ on a 32×32 square lattice in the low-filling regime. The system parameters are chosen to be $U = -2.5$, $V = 0.025$, $\mu = -1.0$ and $\beta = 1000$ in units of t.
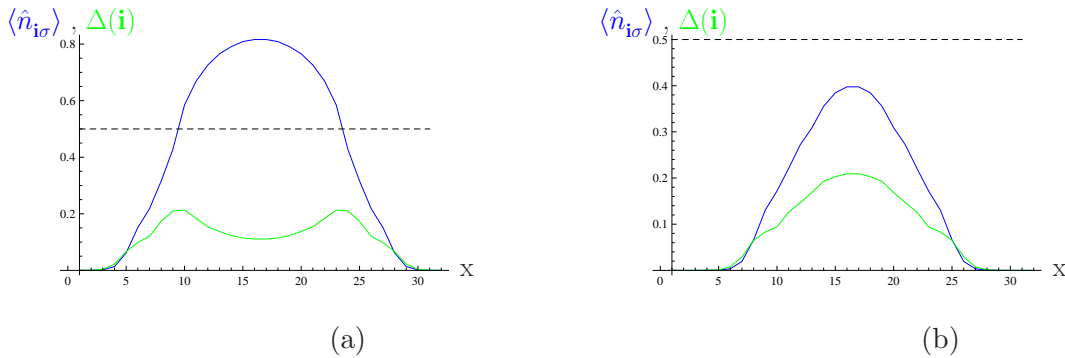

(a)   (b)

Figure 3.3: Particle densities and superfluid order parameter at y-position 12. In (a)/(b) the parameters are chosen to be as in Figure (3.1)/(3.2). The superfluid order parameter obeys the LDA-distribution; in particular, it is maximal in the region of half filling.

For balanced systems the LDA, which is an approximation to the full Hartree-Fock equations, is known to be adequate for the description of, e.g., the particle distribution and the superfluid order parameter as a function of $\mathbf{i}$. In addition to these quantities, we present the spectrum (density of states) of a balanced system. In order to obtain a suitable graphical representation, the delta functions of the discrete spectrum have been broadened to Gaussians according to

$$\rho(\omega) \equiv \frac{1}{2\mathcal{N}\sigma\sqrt{\pi}} \sum_{s=1}^{2\mathcal{N}} \exp\left[-\left(\frac{\omega - E_s}{\sigma}\right)^2\right], \tag{3.15}$$

where E_s are the eigenenergies.

The spectrum presented in Figure (3.4) is symmetric, in agreement with Eq. (3.13). The gap around the Fermi edge ($\omega = 0$) is interpreted as the BCS-gap analogously to translationally invariant systems. Since in translationally invariant systems $\Delta(\mathbf{i})$ does not depend on $\mathbf{i}$ the gap has the size $\omega_{\text{GAP}} = 2U\Delta$ (see chapter (2)). In a trapped system the definition of the gap must be formulated more generally as

$$\omega_{\text{GAP}} \equiv 2\min_s|E_s|, \tag{3.16}$$

which leads to the correct result for translationally invariant systems. The size of the gap
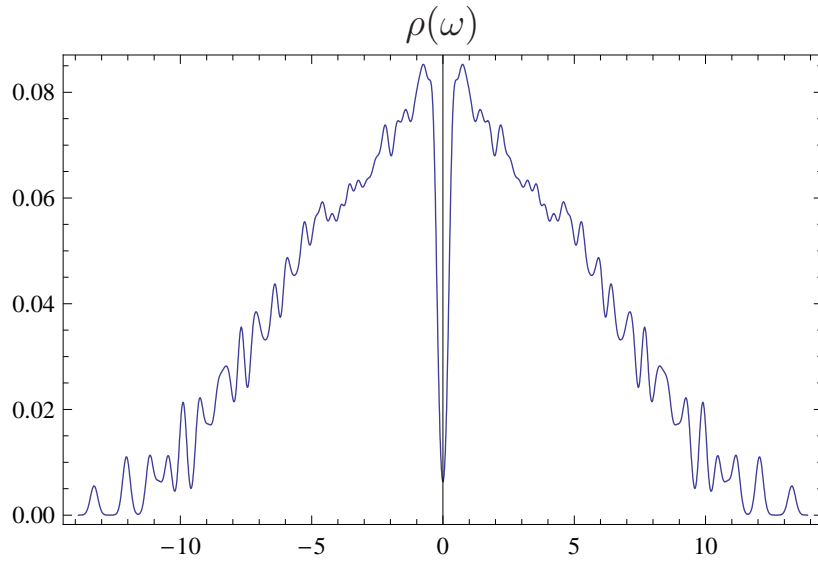
Figure 3.4: Normalized density of states $\rho(\omega)$ of the system described in Figure (3.1), where the discrete eigenenergies have been broadened according to Eq. (3.15) with $\sigma = 0.2$. The size of the gap is determined to be $\omega_{\mathrm{GAP}} \approx 0.57$.

ω_{GAP} plays an important role in rf-spectroscopy experiments and it will play a role in the following part of this thesis.

3.2.2   Imbalanced systems

If one turns on the imbalance ($\Delta\mu \neq 0$), to first approximation the whole spectrum is shifted according to Eq. (3.14). For these reasons, at sufficiently low temperatures (exact statement in the ground state), there exists a solution for which the system configuration will hardly (not at all in the ground state) differ from the balanced one if one chooses $\Delta\mu \leq \omega_{\mathrm{GAP}}$. Nevertheless, one will find different competing solutions. These differ via their grand potential defined as

$$\Omega \equiv -\frac{1}{\beta} \sum_{s=1}^{2\mathcal{N}} \ln\left[1 + \exp\left(-\beta\, E_s\right)\right] + U \sum_{\mathbf{i}} \left[\langle \hat{n}_{\mathbf{i}\uparrow} \rangle \left(1 - \langle \hat{n}_{\mathbf{i}\downarrow} \rangle\right) - |\Delta(\mathbf{i})|^2\right] \qquad (3.17)$$

according to the matrix-definition of the Hamiltonian in (3.3). In the ground state ($\beta \to \infty$) Eq. (3.17) reduces to

$$\Omega \to \sum_{s=1}^{2\mathcal{N}} E_s \Theta(-E_s) + U \sum_{\mathbf{i}} \left[\langle \hat{n}_{\mathbf{i}\uparrow} \rangle \left(1 - \langle \hat{n}_{\mathbf{i}\downarrow} \rangle\right) - |\Delta(\mathbf{i})|^2\right] \, . \qquad (3.18)$$

The thermodynamically stable solution is the one minimizing (3.17). We will present systems with different imbalance strengths at different fillings in Figures (3.5)-(3.8); in particular, the spectra are shown in Figure (3.6). In the case of different competing solutions we always present only the solution lowering the grand potential.

An important point is the geometrical structure of the solutions found. According to Hamiltonian (3.1) the particle density $n_{\mathbf{i}}$, the magnetization $m_{\mathbf{i}}$, and the superfluid order parameter $\Delta(\mathbf{i})$ fulfill the same symmetry as the Hamiltonian itself. If one turns the interaction

off ($U = 0$), one obtains trivially $\Delta(\mathbf{i}) = 0$ and, thus, a spherically symmetric distribution for $n_{\mathbf{i}}$ and $m_{\mathbf{i}}$. A priori, one would expect the same symmetry for $n_{\mathbf{i}}$ and $m_{\mathbf{i}}$ if the interaction is attractive ($U < 0$). However, we find that this symmetry does not occur for all parameter configurations. For balanced systems we always find a unique solution which does fulfill this symmetry. In imbalanced systems this depends on the chosen parameters. The parameters, deciding whether a solution is rotationally symmetric or not, are the filling in the trap center and the imbalance strength. If the filling in the trap center is low ($n_C \lesssim 1.8$) one always finds an order parameter with a radially symmetric structure as shown, e.g., in Figure (3.8). While in the balanced case the superfluid order parameter may be chosen to be positive, sign changes in the radial direction occur in the imbalanced case. The magnetization is maximal in the region where $\Delta(\mathbf{i})$ changes its sign. In the high-filling regime ($n_C \gtrsim 1.8$) the radial symmetry is not valid anymore. Sign changes may also occur along the azimuthal direction. Results are shown in Figure (3.5). In Figure (3.5) (a)-(c) results for a low imbalance are shown. As one can see in (a) and (b), the order parameter and the magnetization break the $\pi/2$-rotational symmetry leading to a preferred axis, on which the system is magnetized. In Figure (3.5) (d)-(f), results for a higher imbalance strength are shown. Here, only the argument of the superfluid order parameter breaks the $\pi/2$-rotational symmetry, while its absolute value and the magnetization do not. Little peaks in the magnetization are visible in the region where the order parameter changes its sign in azimuthal direction. Nevertheless, these peaks are relatively small when compared with the "background" magnetization. If one increases the imbalance more, the superfluidity breaks down, and one ends up in the normal phase with $\Delta(\mathbf{i}) = 0 \ \forall \ \mathbf{i}$. Results for this case are shown in Figure (3.7). No symmetry is broken at all.

Furthermore, we present the spectral function for these different parameter regions in Figure (3.6). In the balanced case, the spectrum is a symmetric function of ω as shown in Figure (3.4) having the BCS-gap at the Fermi edge. Turning on the imbalance $\Delta\mu$ shifts the spectrum as explained in Equation (3.14) at first. But, since the spectrum is determined self-consistently, too, it changes its features with increasing imbalance, especially the shape and the depth of the gap at the Fermi edge. By comparing the spectra presented in Figures (3.4) and (3.6), one can see that, in the balanced system, the spectrum is symmetric at $\omega = 0$ and that it has one deep and relatively broad gap. In the imbalanced cases the spectrum is not symmetric according to Equation (3.13). The superfluid gap basically remains, while it is drastically reduced in its depth. In the normal phase [Figure (3.6)(c)] there is no gap at the Fermi edge at all.

The most important questions to be discussed in connection with the results presented in this section are their experimental realization and the comparison to already existing literature. As emphasized above, one of the most common methods used to treat the trapping potential $V(\mathbf{i})$ is the LDA [71, 72, 84, 53, 56]. In the LDA-formalism, results breaking the rotational invariance are not obtainable, since each lattice site is treated independently from each other. Therefore, the occupation number, the magnetization and the superfluid order parameter depend only on the value of $V(\mathbf{i})$, and not on the position $\mathbf{i}$ itself. Hence, while the LDA works very well for balanced systems, it completely fails in describing imbalanced ones.

A still not completely answered question in the literature is how to detect the superfluid magnetic phase. One method which seems to be suitable for the detection of the states found in this work is in-situ imaging [16, 17, 18]. In-situ imaging works especially well for a two-dimensional system, since the images directly represent a plane and are not a sum over several planes like in three dimensions. Since the magnetization may be measured directly with spin-selective methods, it may be used as evidence for this unconventional superfluidity

shown, e.g., in Figure (3.5)(b). Within these parameter settings, the magnetized region lies on a preferred axis whose direction is chosen by spontaneous symmetry breaking. In contrast to the magnetization, the total particle density does not show any features which could be used for an experimental detection of superfluidity. An experimental realization of such a state would strongly confirm our results which are based on theoretical work.
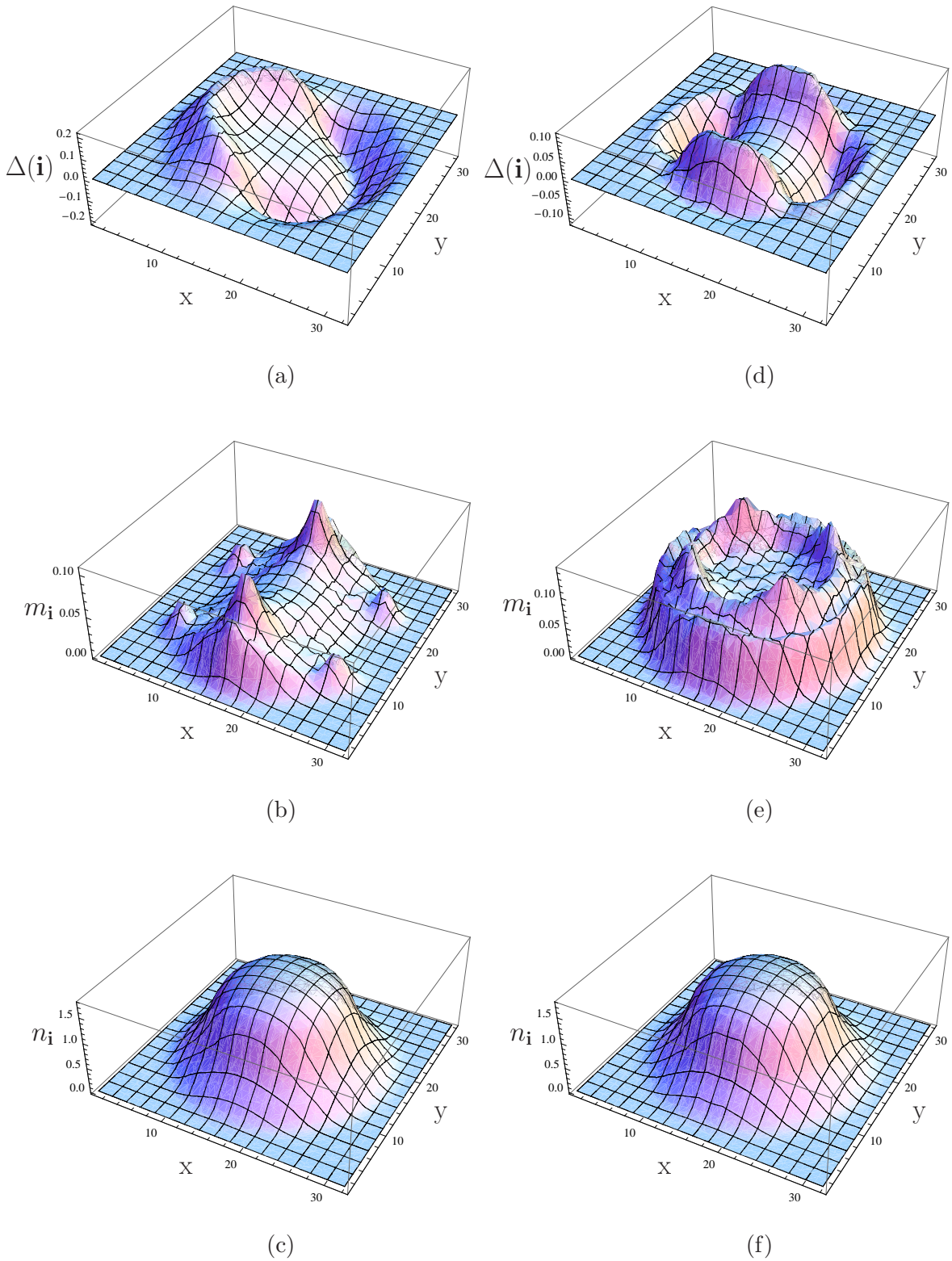
(a)

(d)

(b)

(e)

(c)

(f)

Figure 3.5: Superfluid order parameter, magnetization and particle densities of a thermodynamically stable unbalanced state on a 32×32 square lattice in the high-filling regime. The parameters are the same as in Figure (3.1) with exception of the imbalance parameter which is chosen to be (a)-(c) $\Delta\mu = 0.6$ and (d)-(f) $\Delta\mu = 1.0$.
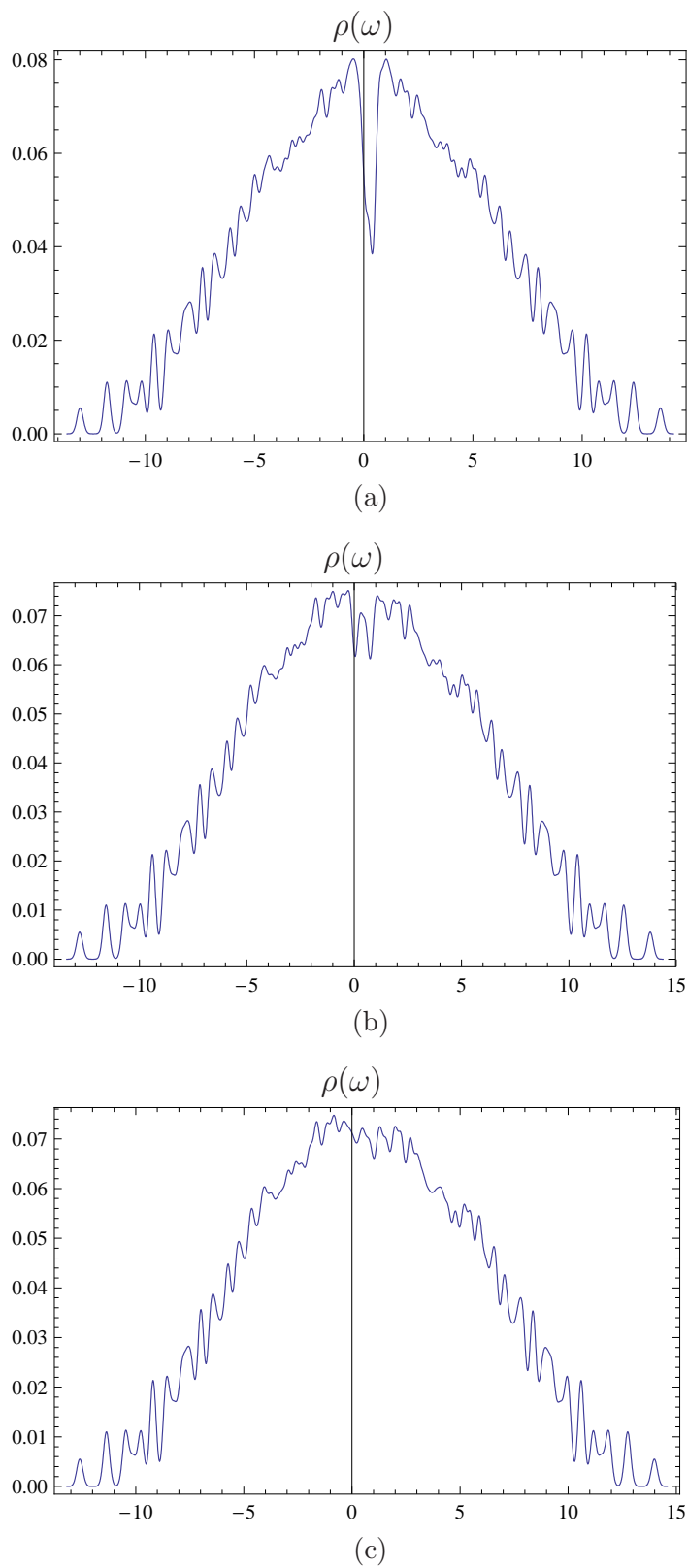
Figure 3.6: Normalized density of states $\rho(\omega)$ of the system described in Figure (3.1). The discrete eigenenergies have been broadened according to Eq. (3.15) with $\sigma = 0.2$.

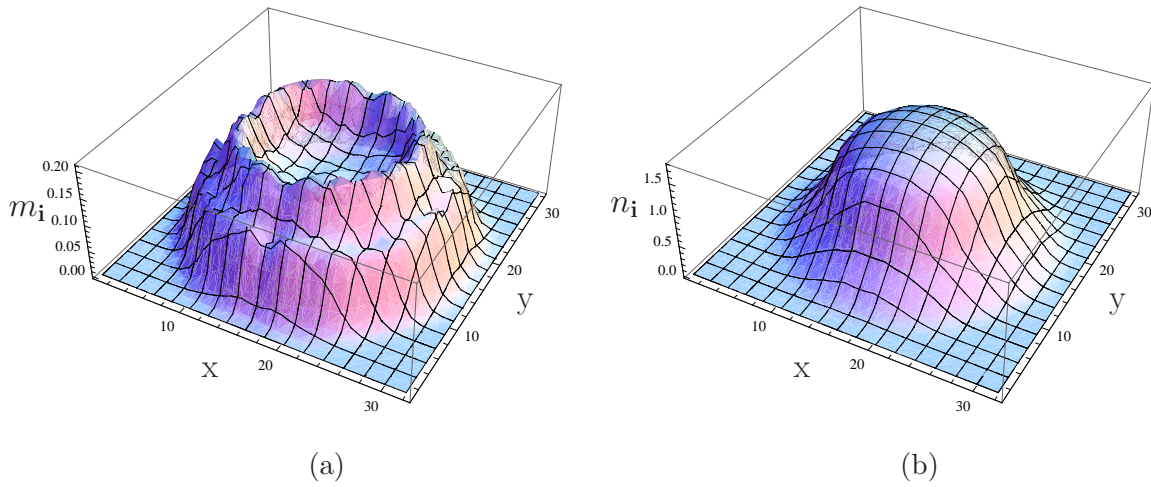(a)   (b)

Figure 3.7: Magnetization (a) and particle density (b) of a thermodynamically stable unbalanced state on a 32×32 square lattice in the high-filling regime. The parameters are the same as in Figure (3.1) with exception of the imbalance parameter which is chosen $\Delta\mu = 1.4$. The superfluid order parameter $\Delta(\mathbf{i})$ vanishes and is therefore not shown.

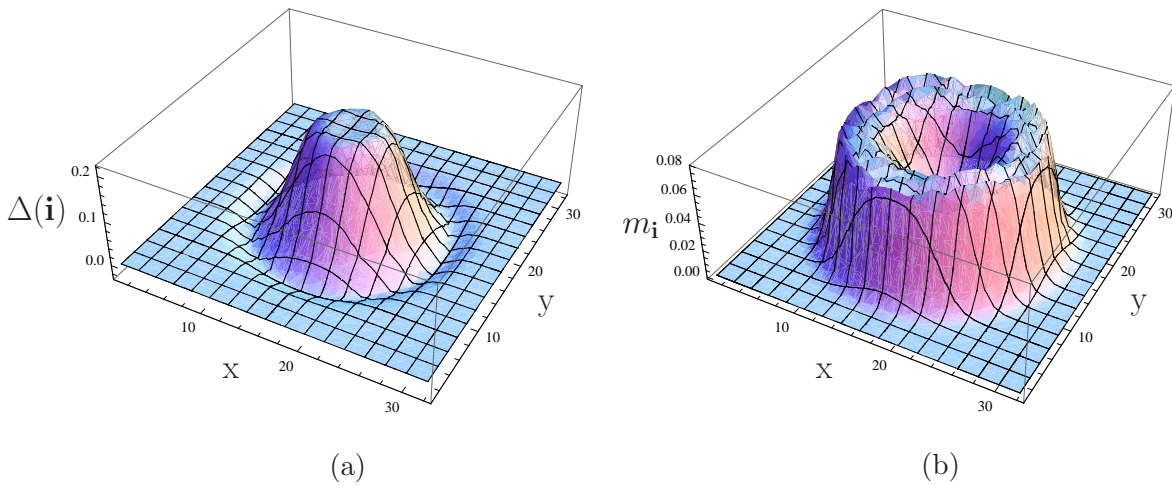(a)   (b)

Figure 3.8: Superfluid order parameter (a) and magnetization (b) of a thermodynamically stable unbalanced state on a 32×32 square lattice in the low-filling regime. The parameters are chosen to be be $U = -2.5$, $V = 0.025$, $\mu = -1.0$, $\Delta\mu = 0.6$ and $\beta = 1000$ in units of t.

3.3 Solutions with complex order parameter

In this section, we present numerically stable solutions with a complex order parameter $\Delta(\mathbf{i})$. As suggested in (1.4.2), a complex solution must have at least one vortex at equilibrium, analogously to the situation in bosonic condensates, where vortices are one of the most important types of excitations. Numerical results are shown in Figures (3.9) - (3.13). Solutions containing vortices for unmagnetized systems are presented in Figure (3.9) with the corresponding spectra shown in Figure (3.10). We found self-consistent solutions with a vortex number up to $m = 3$ in the parameter regime shown in this section. There is no prominent effect of the vortex visible in the particle densities, and the dependence of the absolute value of the superfluid order parameter is weak. In the spectral function one can see that the superfluid gap at the Fermi edge ($\omega = 0$) decreases with increasing vortex quantum number. As a consequence, the numerical and the thermodynamic stability decreases with increasing vortex number m. Turning on the imbalance of the system still allows the complex solutions which are presented in Figures (3.11) for $\Delta\mu = 0.2$ and in Figure (3.12) for $\Delta\mu = 0.4$. In the weaker imbalanced case, solutions with $m \leq 2$ survive numerically; for the stronger imbalanced case, only the $m = 1$ solution is stable. For stronger magnetizations we do not find any more vortex-solutions in this parameter regime. Recapitulating, the imbalance and the existence of vortices weaken the numerical stability of a superfluid solution. Both effects together lead to a small regime where a magnetized vortex can occur.

Interestingly, we found solutions containing vortices only in the high-filling regime (nearly full occupation in the trap center). A heuristic explanation for this situation is the following. In the high-filling regime, the order parameter $\Delta(\mathbf{i})$ is nearly zero anyway, regardless whether the order parameter is real or complex. If the filling is lower, a vortex would nevertheless require the order parameter to be zero in the center. As we have seen in Figure (3.9), the structure of $|\Delta(\mathbf{i})|$ does only weakly depend on the vortex number m, so that the required deformation of the structure seems to lead to a numerical instability of any vortex-solution.

The physical importance of the vortex-solutions is the following: The solutions with a real order parameter always have a lower grand-potential. This was already suspected in (1.4.2). Hence, the vortex-solutions must be interpreted as excitations carrying angular momentum. As already known from experiments in the lattice-free situation [15], a superfluid fermionic gas generates vortices in the BCS-regime if it is rotated. Since vortices carry angular momentum, we find the same conclusion for our situation in the optical lattice. As also found experimentally in [15], superfluidity breaks down if one increases the population imbalance. We find the same conclusion: the mechanism of a rotating fermionic superfluid is similar in the absence and in the presence of an optical lattice. The main difference in the interpretation of the motion is that one has a free rotation of particles in the lattice-free case, while one has a phase-coherent site-to-site tunneling process in our case. Furthermore, the vortex excitations are self-consistent solutions of our saddle-point Hamiltonian. Therefore, the states presented in this section do not have any time evolution, which is not generally the case. In contrast to a lattice-free situation the core of the vortex has non-vanishing particle density, only the superfluid order parameter is zero. This is due to the fact that we are in a one-band situation according to our Hamiltonian and this is in contrast to lattice-free systems, where one has a large number of bands occupied.
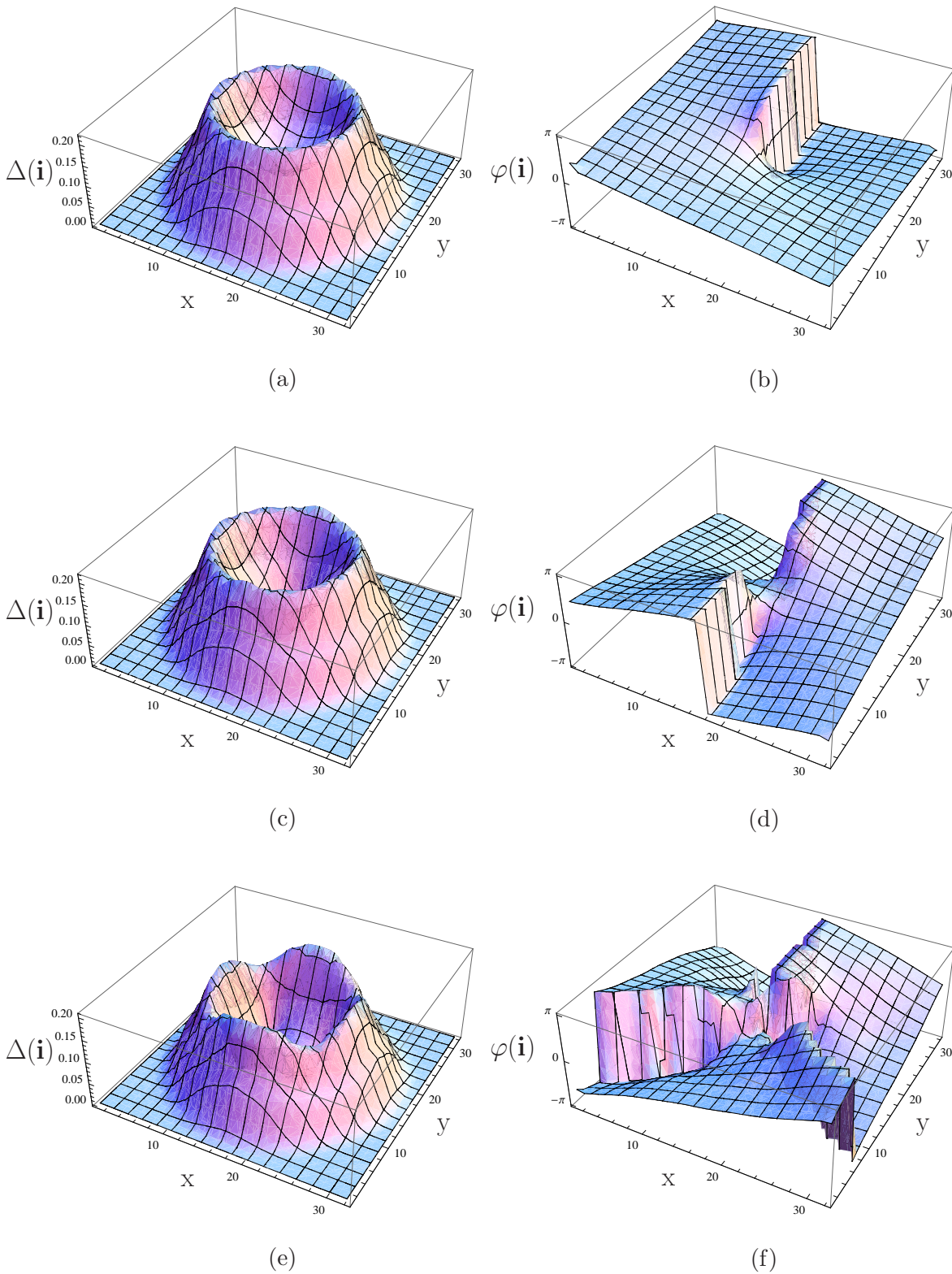
Figure 3.9: Absolute value and argument of the superfluid order parameter in vortex-type solutions. The vortex number is chosen to be $m = 1$ for (a)-(b), $m = 2$ for (c)-(d) and $m = 3$ for (e)-(f). The system parameters are chosen to be as in Figure (3.1).
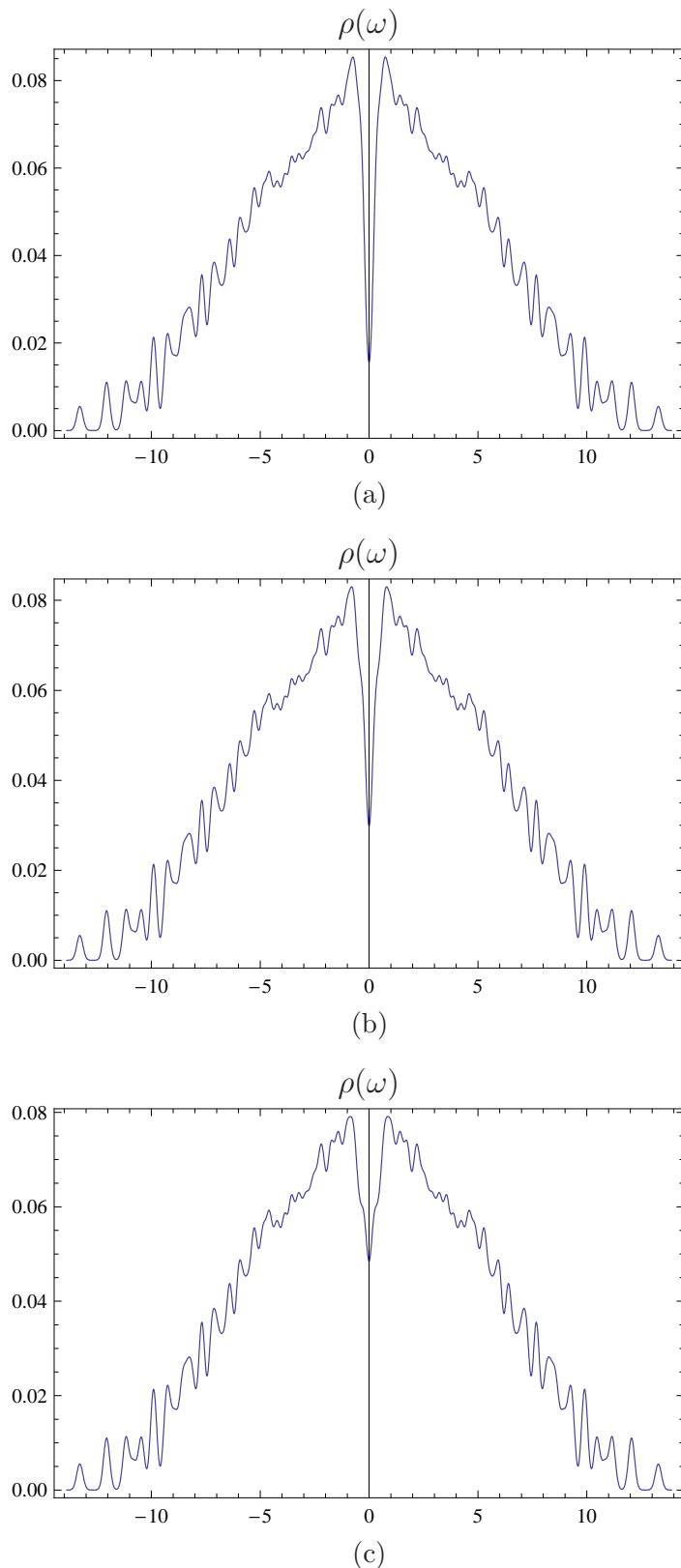
(a)

(b)

(c)

Figure 3.10: Normalized density of states $\rho(\omega)$ of the systems described in Figure (3.9). The vortex number is chosen to be (a) $m = 1$, (b) $m = 2$ and (c) $m = 3$. Since the system is unmagnetized, the spectra are symmetric according to Eq. (3.13).
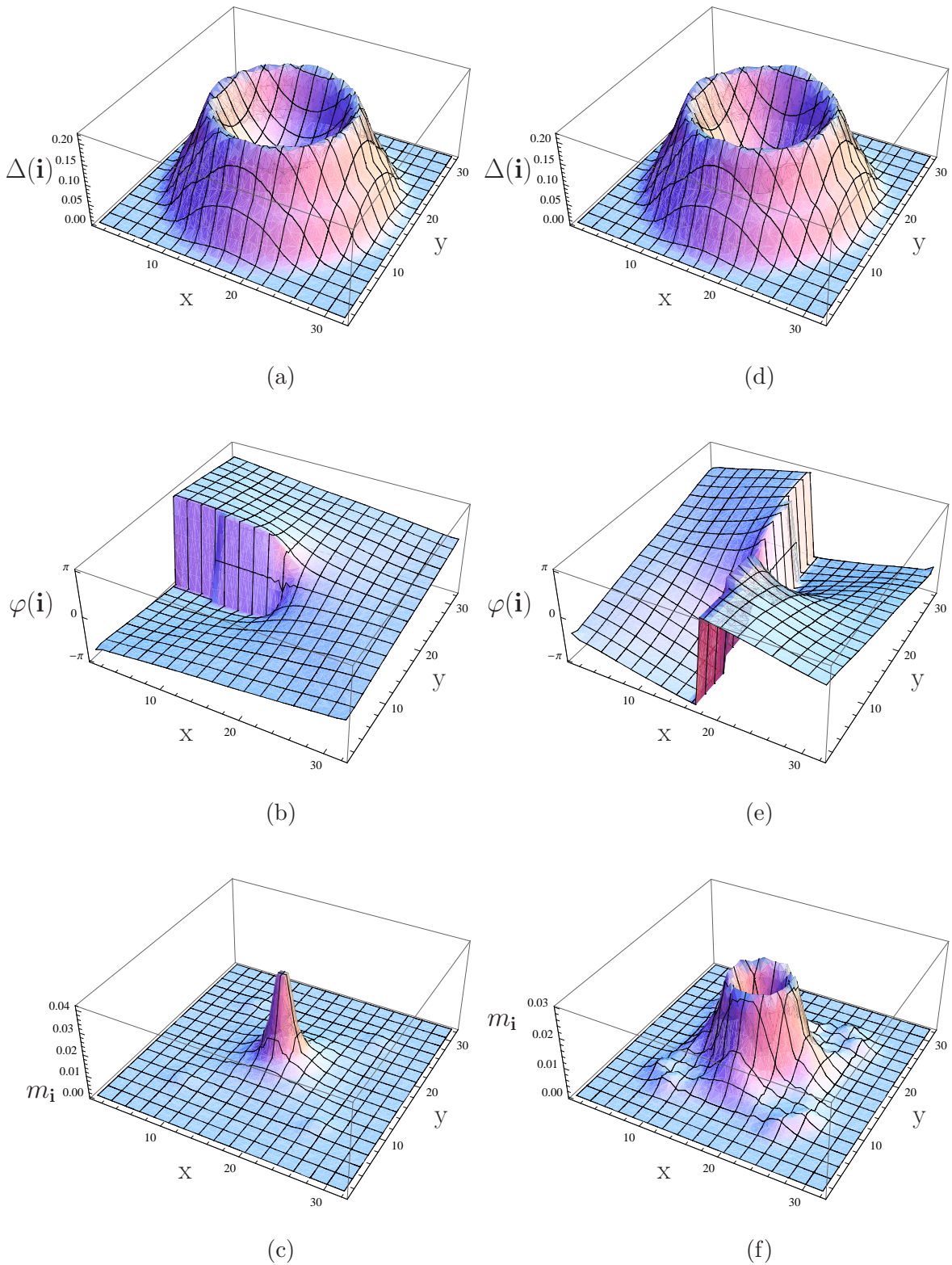
Figure 3.11: Superfluid order parameter $\Delta(\mathbf{i})$ and magnetization of vortex solutions with vortex numbers $m = 1$ (a)-(c) and $m = 2$ (d)-(f). The system parameters are chosen to be as in Figure (3.1) with the exception of $\Delta\mu = 0.2$.
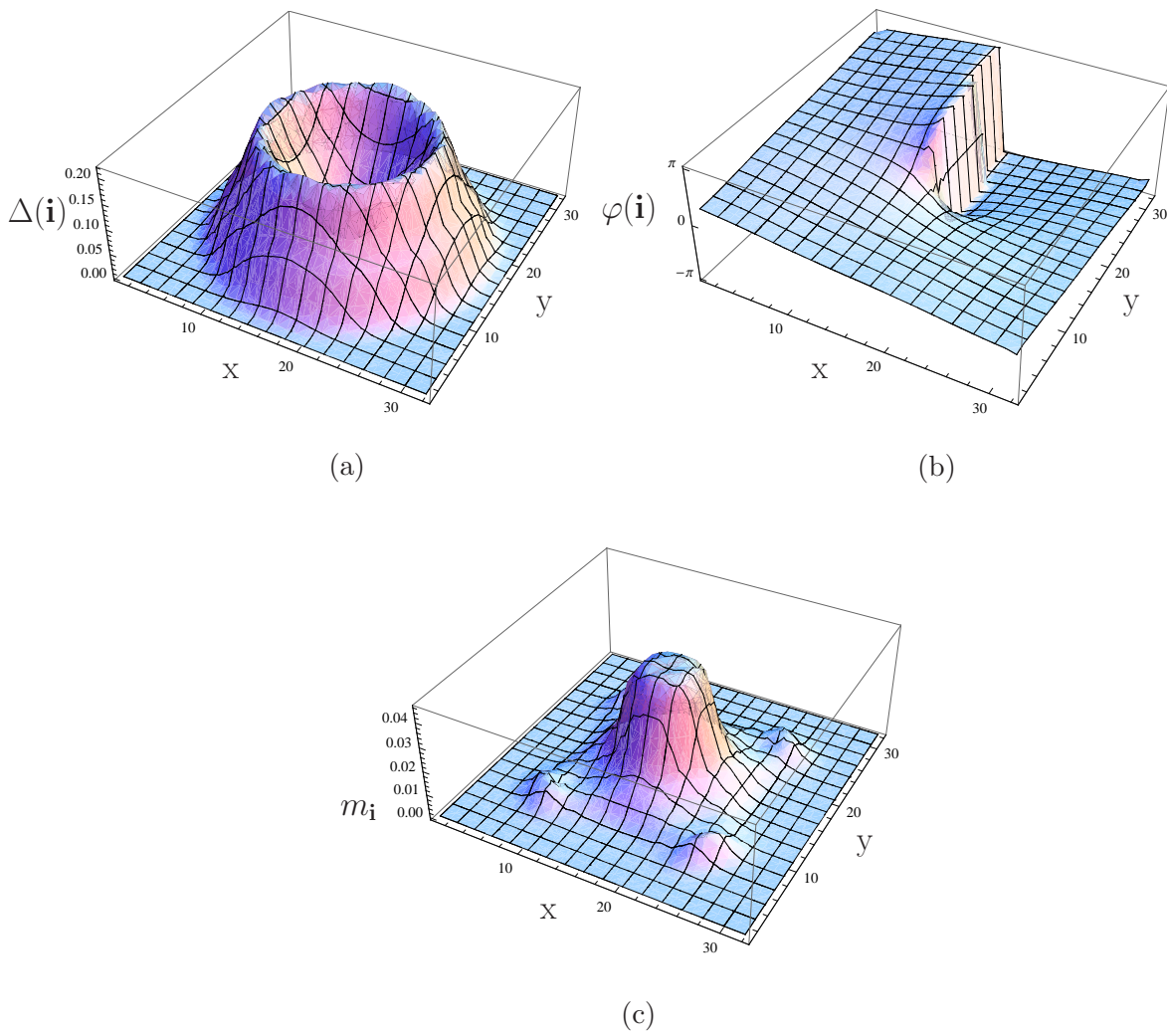
(a)

(b)

(c)

Figure 3.12: Superfluid order parameter $\Delta(\mathbf{i})$ and magnetization of a vortex solution with vortex number $m = 1$. The system parameters are chosen to be as in Figure (3.1) with the exception of $\Delta\mu = 0.4$.
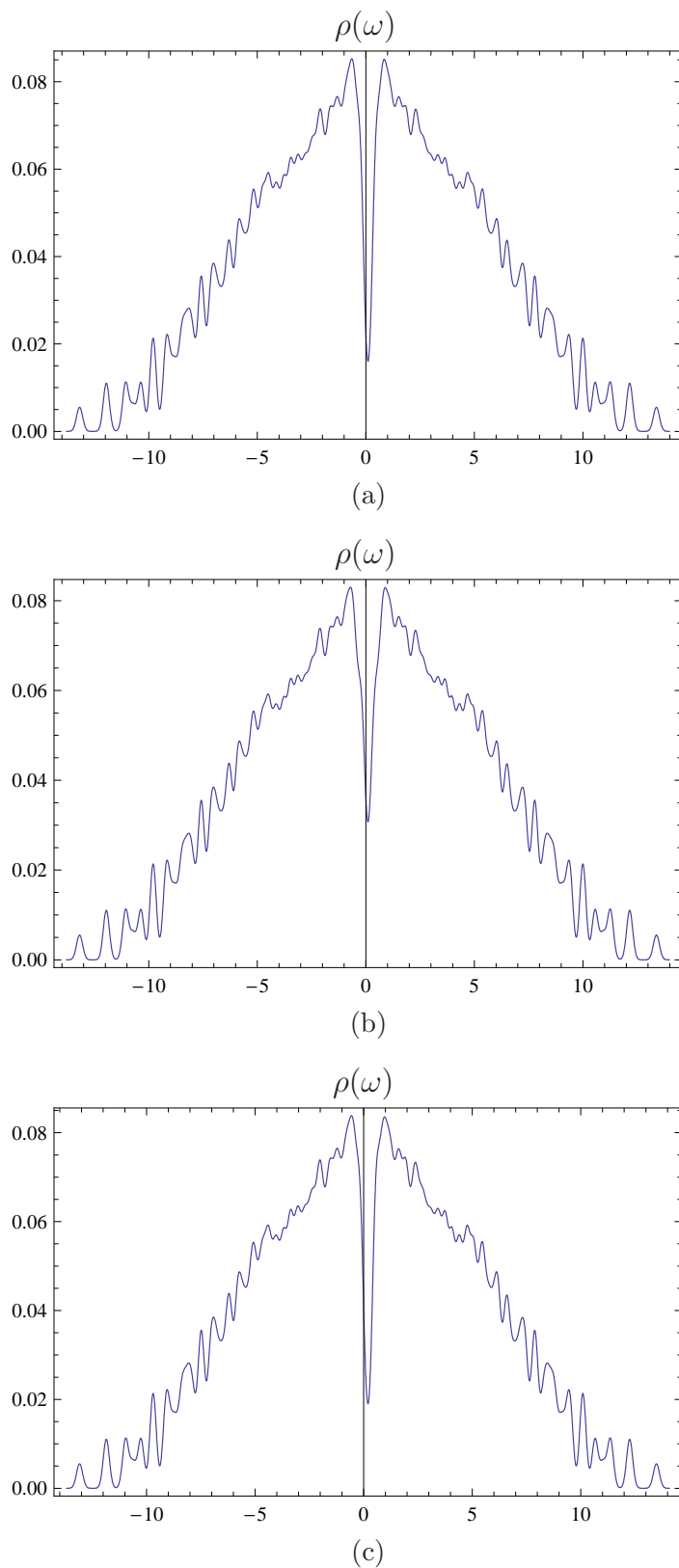
Figure 3.13: Normalized density of states $\rho(\omega)$ of the systems described in Figures (3.11) and (3.12). The spectra correspond to the parameter settings of (a): Figure (3.11) (a)-(c), (b): Figure (3.11) (d)-(f) and (c): Figure (3.12).

3.4   Role of the Hartree terms

In this section, we emphasize the role of the Hartree terms of our saddle-point Hamiltonian. In the literature (see, e.g., Refs. [73, 74]), the Hartree terms of the interaction

$$\mathcal{H}_{U,\text{Hartree}} = U \left(\langle \hat{n}_{\mathbf{i}\uparrow} \rangle \hat{n}_{\mathbf{i}\downarrow} + \langle \hat{n}_{\mathbf{i}\downarrow} \rangle \hat{n}_{\mathbf{i}\uparrow} - \langle \hat{n}_{\mathbf{i}\uparrow} \rangle \langle \hat{n}_{\mathbf{i}\downarrow} \rangle \right) \tag{3.19}$$

are typically neglected in order to reduce the computational effort even though, numerically, they are of the same magnitude as the pairing-terms. While in the balanced case ($\Delta\mu = 0$) the Hartree terms only deform the trapping potential $V(\mathbf{i})$, in the imbalanced case they cause an additional space dependent Zeeman term having globally the opposite sign of $\Delta\mu$.

   In this section, we perform calculations both including and neglecting the Hartree terms. In order to make our results comparable with the previous literature, we choose $U = -4$ in units of t, as the authors of Ref. [74] do, even though the interaction is then of the same size as the half bandwidth. Higher order corrections play a role in this parameter regime, but our aim is to emphasize the importance of the Hartree terms in the spatially inhomogeneous case. The remaining system parameters are also chosen similarly as in Ref. [74]. In this section, we again restrict consideration to real superfluid order parameters.

   Numerical results with neglected Hartree terms are presented in Figures (3.14)-(3.18). Since the results for the high- and low-filling regimes do not differ qualitatively in the sense of the structure of the superfluid order parameter from the results with Hartree terms included, we only treat what in Ref. [74] is called the medium-filling regime $n_{\text{Center}} \approx 1$. In Figure (3.14) the balanced case is shown. Again we obtain a positive superfluid order parameter. The imbalanced system with a low magnetization [Figure (3.15)(a)-(c)] still has similar features as a system with Hartree terms included. One obtains a single sign change in $\Delta(\mathbf{i})$ in radial direction. In the region where this sign change takes place a magnetized ring occurs. If one increases the imbalance [Figure (3.15)(d)-(f)], a phase with an oscillatory superfluid order parameter and magnetization occurs, which is described as the main feature of the medium-filling regime in Ref. [74]. The region where this phase is stable is at least drastically reduced when the Hartree terms are included. A highly oscillating magnetization automatically induces a space-dependent Zeeman term with its sign opposite to $\Delta\mu$, thus reducing the magnetization in a self-consistent calculation. Results with Hartree terms included are shown in Figure (3.19). The calculations including the Hartree terms cannot be compared with the previous ones at the same values of μ and $\Delta\mu$, of course. Since $U < 0$, it is necessary to reduce μ and to increase $\Delta\mu$ in order to obtain approximatively the same total particle numbers for both spin-species if one wants to keep them fixed. These results are shown in Figure (3.19)(a)-(c). As a result, the Hartree terms drastically compress the region, where the lattice sites are occupied. Keeping the particle numbers approximatively fixed leads to an increase of the filling in the center from $n_{\text{Center}} \approx 1.3$ to $n_{\text{Center}} \approx 1.9$. This leads to a strong deformation of the spatial structure of $\Delta(\mathbf{i})$ and $m_{\mathbf{i}}$. The superfluid order parameter still has sign changes along the azimuthal direction, but its shape is not strongly oscillating. It decreases down to $\sim 1\%$ of the maximal value in the center of the trap. The magnetization is strongly smeared out. There are only a few small peaks in the region where $\Delta(\mathbf{i})$ changes its sign (relative height: $\sim 75\%$ with Hartree terms, $\sim 165\%$ without Hartree terms).

   Obviously, with the results presented above, the filling in the center of the trap is far away from 1, so that one must answer the question whether the highly oscillatory phase occurs at a lower filling if the Hartree terms are included. Hence, we also present results for lower filling in Figure (3.19)(d)-(f). Here, the filling at the center is $n_{\text{Center}} \approx 1.6$. This is also not very close to 1.3, like in the case where we obtain highly oscillatory behavior in the system without

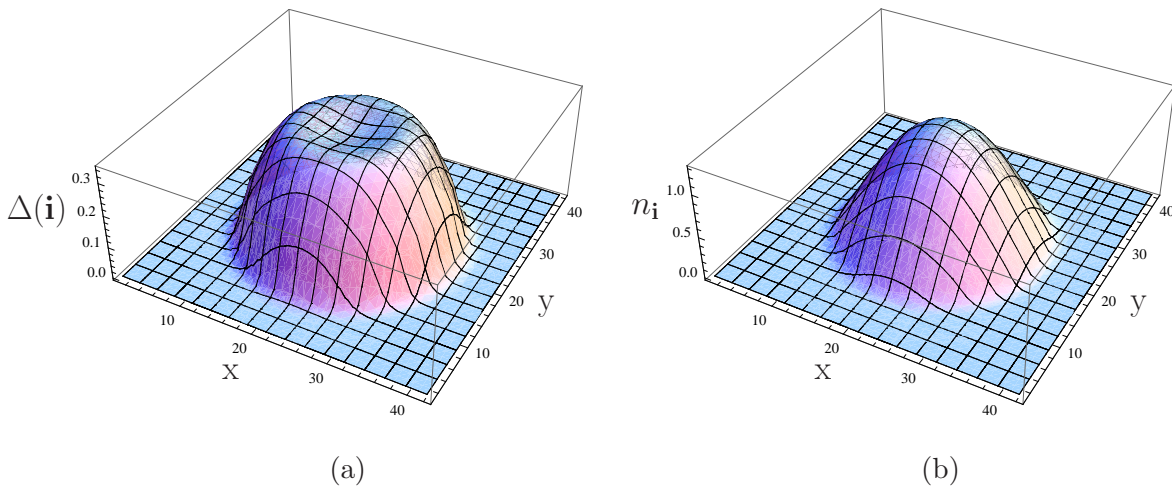(a)   (b)

Figure 3.14: Superfluid order parameter and particle distribution of a balanced mixture on a
42×42 lattice at parameters $U = -4$, $V = 0.025$, $\mu = 1.0$ and $\beta = 1000$ in units of t. The
Hartree terms have been neglected in this calculation.

Hartree terms, but a further reduction of the filling leads to a too low number of particles
in the system, which is not useful and leads to severe numerical instabilities. Nevertheless,
in Figure (3.19)(d)-(f) one may observe that there are only sign changes in radial direction,
as it is the case in the low-filling regime presented in Ref. [74] or in section (3.2) of this
work. An additional sign change occurs and, hence, a double-ring structure is visible in the
magnetization with each ring lying in the spatial region where the sign change in $\Delta(\mathbf{i})$ occurs.
In conclusion, we did not find the highly oscillatory phase when including the Hartree terms
in our calculations.

Another interesting feature is the shape of the spectral functions belonging to our con-
figurations. These are presented in Figures (3.17) and (3.18) for our results with neglected
Hartree terms, and in (3.20) for our results with Hartree terms included. Analogously to all
previous spectra, the spectra without Hartree terms have a gap at the Fermi edge, if super-
fluidity occurs. A comparison of Figures (3.18) and (3.20) reveals that keeping the Hartree
terms also smears out the spectra. Especially the sharp maxima in vicinity of the gap, visible
in Figure (3.18), are strongly decreased. The widths of the gaps basically maintain their size.
Note that the spectra in (3.17) and (3.18) are symmetric around $\omega = \Delta\mu/2$ as a consequence
of Equation (3.14), while inclusion of the Hartree terms leads to a space-dependent Zeeman
shift and consequently to a shift of the spectral weight in negative ω-direction and to a loss
of this symmetry. The spectrum presented in (3.17) is the spectrum of the non-interacting
system, since the normal phase $[\Delta(\mathbf{i}) = 0]$ is equivalent to $U = 0$ if the Hartree terms are
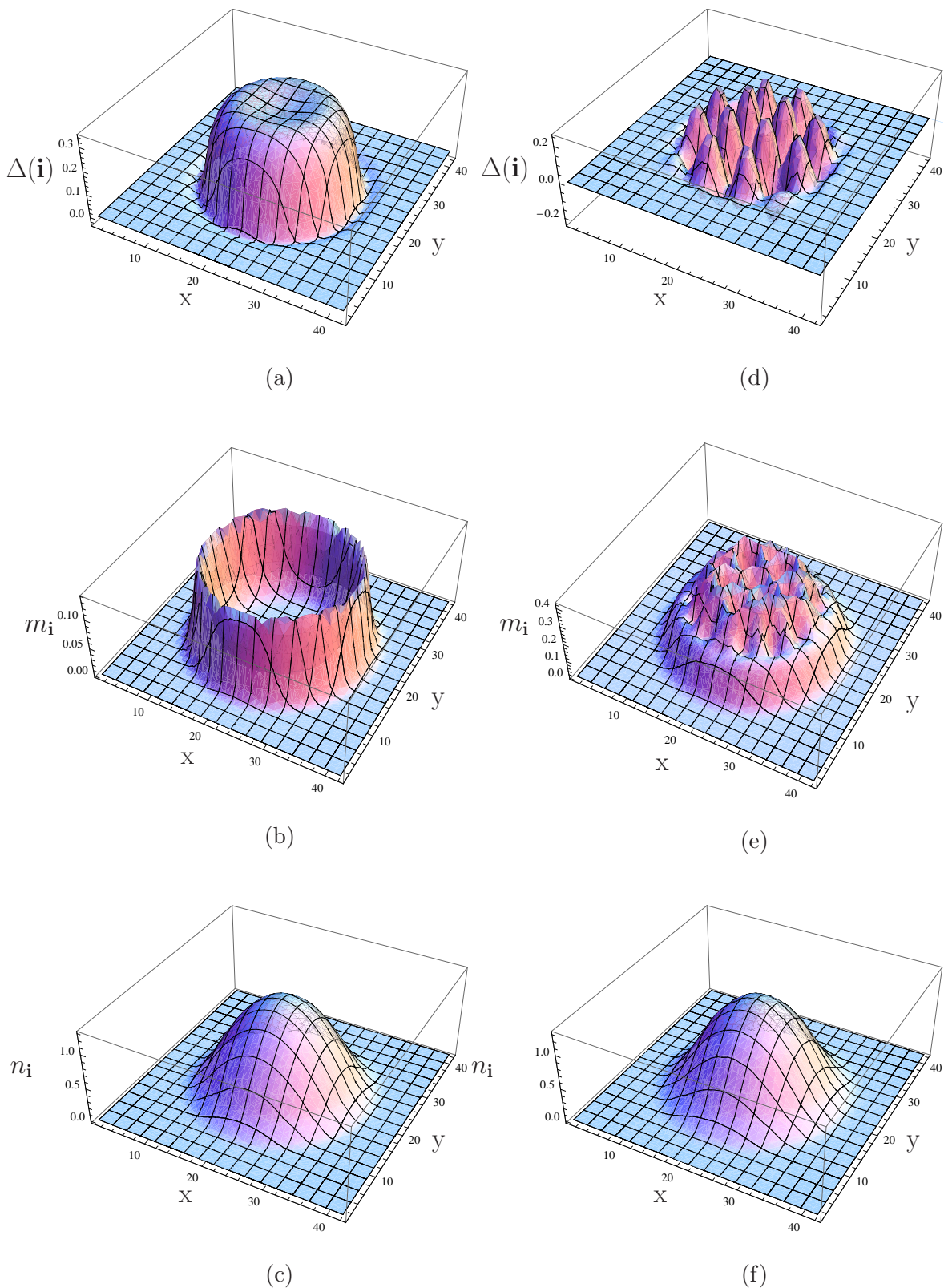neglected. In the normal phase, one does not obtain any gap-like behavior.

Figure 3.15: Superfluid order parameter, magnetization and particle distribution of imbalanced mixtures on a 42×42 lattice at parameters $U = -4$, $V = 0.025$, $\mu = 1.0$, $\beta = 1000$ and (a)-(c) $\Delta\mu = 1.2$, (d)-(f) $\Delta\mu = 1.8$ in units of t. The Hartree terms have been neglected in this calculation.

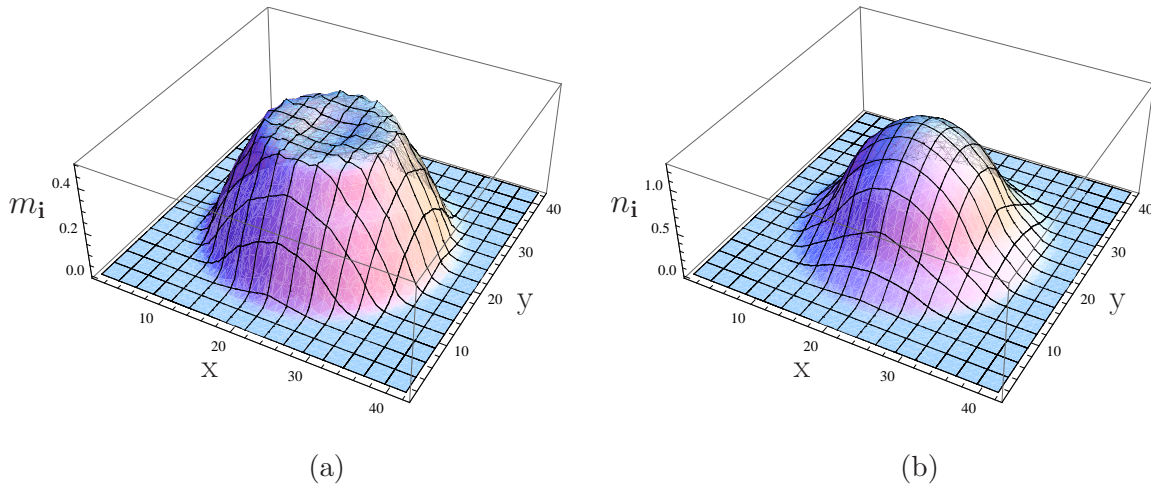(a)   (b)

Figure 3.16: Magnetization and particle distribution of an imbalanced non-superfluid mixture on a 42×42 lattice at parameters $U = -4$, $V = 0.025$, $\mu = 1.0$, $\beta = 1000$ and $\Delta\mu = 2.8$ in units of t. The Hartree terms have been neglected in this calculation.

(a)

Figure 3.17: Normalized density of states $\rho(\omega)$ of the system described in Figure (3.16). The discrete eigenenergies have been broadened according to Eq. (3.15) with $\sigma = 0.35$.
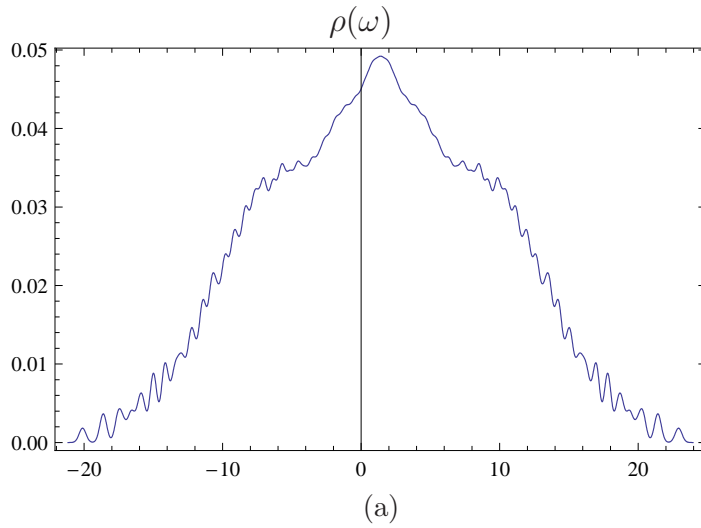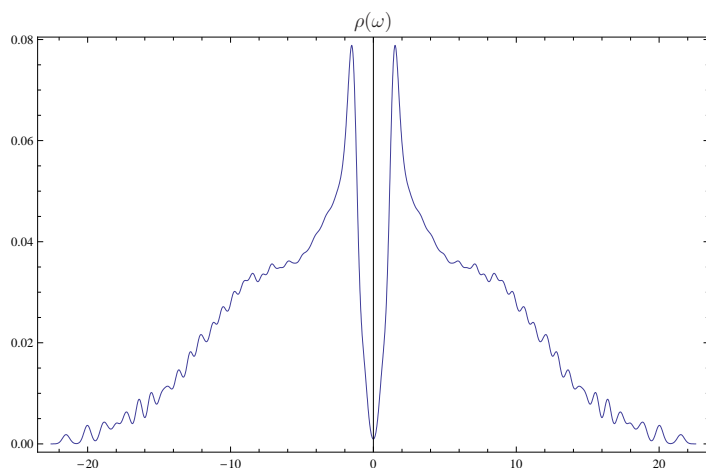
(a)
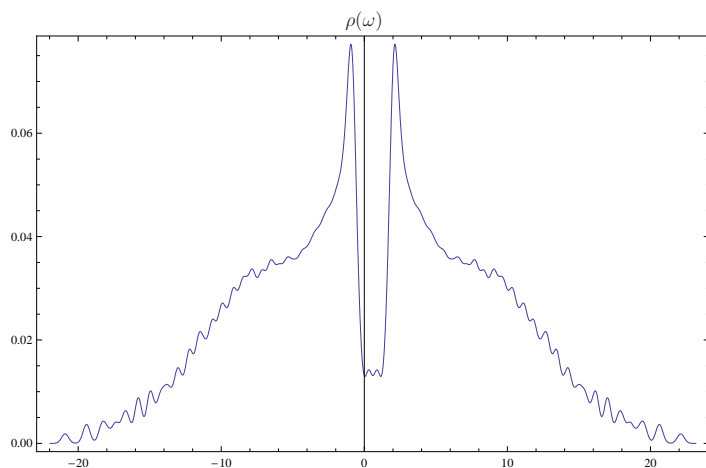
(b)

(c)

Figure 3.18: Normalized densities of states $\rho(\omega)$ of the systems described in Figures (a) (3.14), (b) (3.15) (a)-(c) and (c) (3.15) (d)-(f). The discrete eigenenergies have been broadened according to Eq. (3.15) with $\sigma = 0.35$.

Figure 3.19: Superfluid order parameter, magnetization and particle distribution of imbalanced mixtures on a 42×42 lattice at parameters $U = -4$, $V = 0.025$, $\beta = 1000$, (a)-(c) $\mu = -0.5$ and $\Delta\mu = 2.4$, (d)-(f) $\mu = -1.0$ $\Delta\mu = 2.0$ in units of t. The Hartree terms have been included in this calculation.
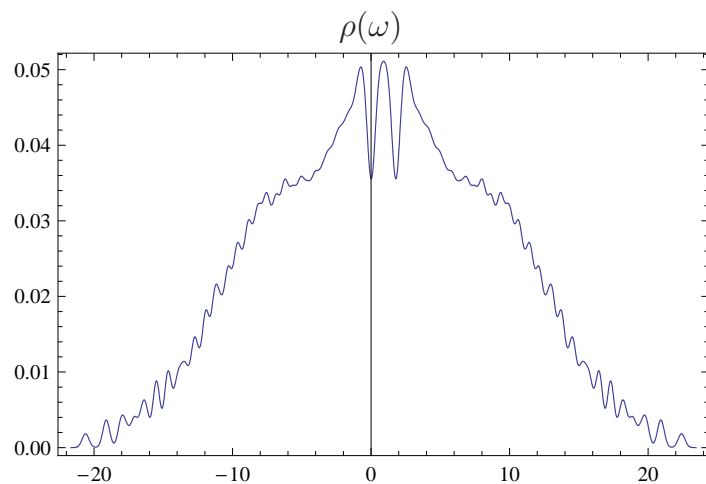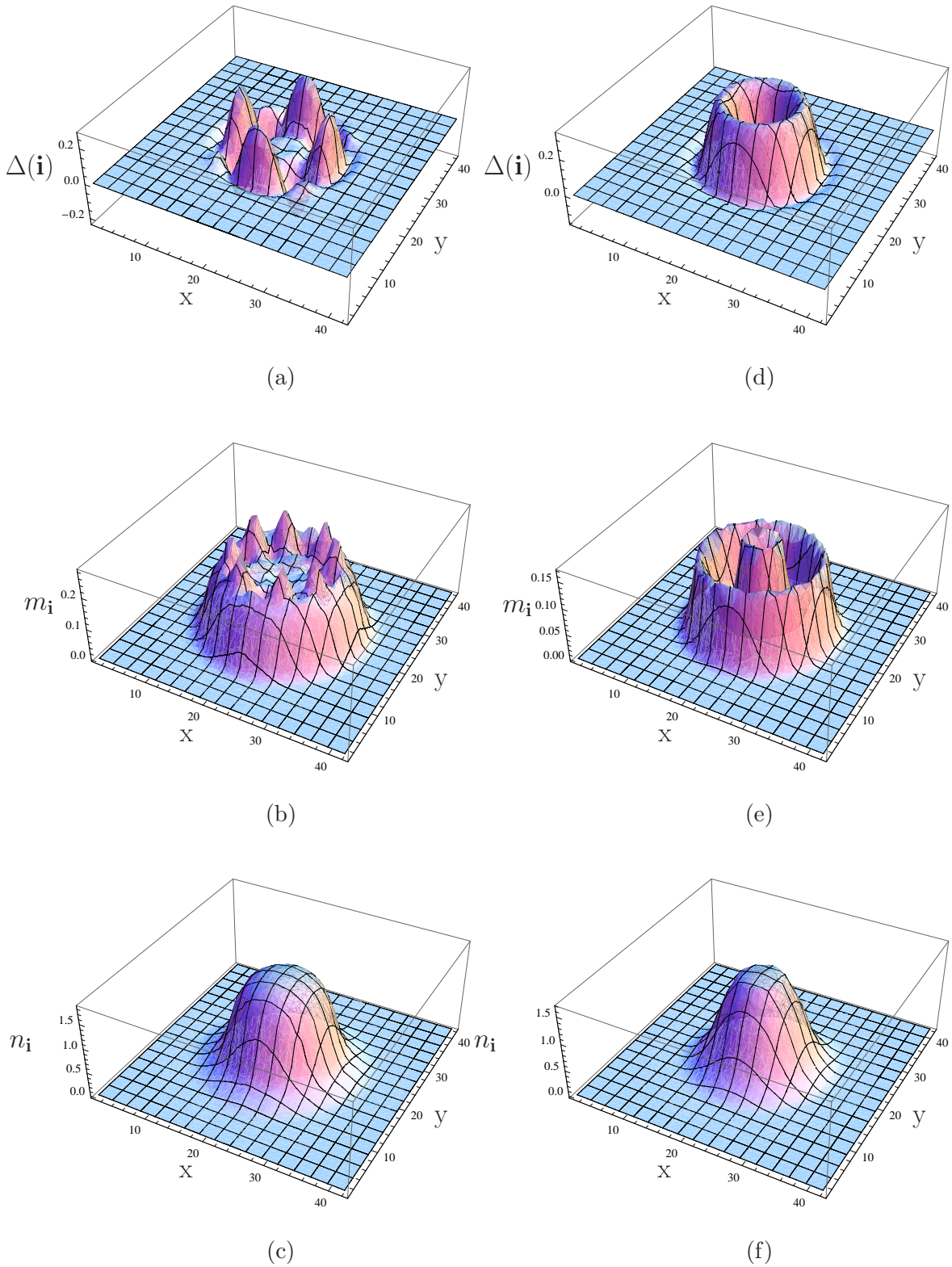
$$\rho(\omega)$$

(a)

$$\rho(\omega)$$

(b)
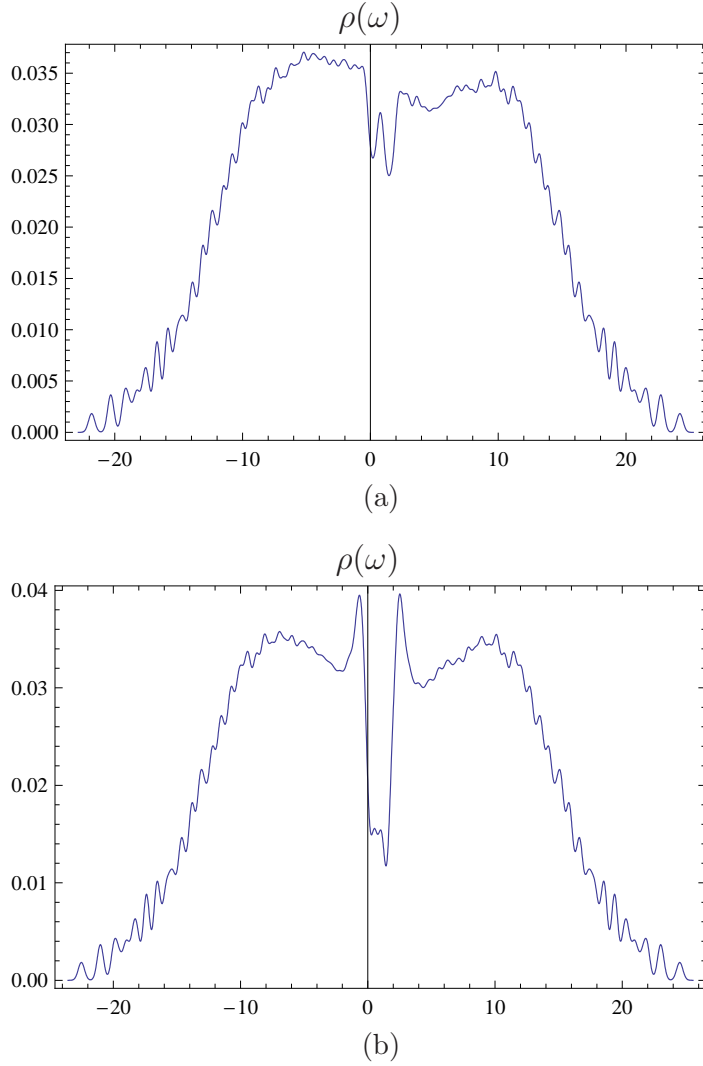
Figure 3.20: Normalized densities of states $\rho(\omega)$ of the systems described in Figures (a) (3.19) (a)-(c) and (b) (3.19) (d)-(f). The discrete eigenenergies have been broadened according to Eq. (3.15) with $\sigma = 0.35$.

3.5   General structure and convergence behavior

Of course, one is interested in general statements and universal laws regarding the superfluid (im)balanced Fermi-mixtures. Since we are performing numerical calculations, it is quite difficult to extract exact statements from the set of self-consistency equations describing our systems. Analytical methods such as, e.g., a Fourier-transformation, are not adequate to solve the exact treatment of the trapping potential beyond LDA, as demonstrated in chapter (2). A few exact analytical statements derived from the general properties of the underlying Hamiltonian (3.1) and the resulting self-consistency equations (3.7) and (3.8) have been outlined at the beginning of this chapter. In this section we build a bridge between the real-valued solutions found in section (3.2) and the complex-valued ones presented in section (3.3) in the high-filling regime.

In order to obtain any solution breaking the rotational symmetry one has to use values

for $\Delta(\mathbf{i})$ and $n_{\mathbf{i}\sigma}$ which already break this symmetry, otherwise the rotational symmetry is conserved for all iterations according to Hamiltonian (3.1) in the saddle-point approximation (exception: numerical errors may break the symmetry automatically and lead to a bad convergence behavior). The authors of Ref. [74] claim to be able to break the symmetry using random numbers, however the implementation of this approach into our program could not reproduce this effect. Instead, if we want to obtain real solutions, we use the input

$$\Delta_0(\mathbf{i}) \equiv \mathrm{Random}(|\mathbf{i}|) * \cos[m\,\phi(\mathbf{i})] \quad , \quad \phi(\mathbf{i}) \equiv \mathrm{atan}\left(\frac{i_2}{i_1}\right) \;, \qquad (3.20)$$

where $\phi(\mathbf{i})$ is the azimuthal angle of the coordinates in real-space and $\mathrm{Random}(|\mathbf{i}|) \in [0, 1/2]$ are homogeneously distributed random numbers, and if we want to obtain complex ones, we use analogously

$$\Delta_0(\mathbf{i}) \equiv \mathrm{Random}(|\mathbf{i}|) * \exp[im\,\phi(\mathbf{i})] \;. \qquad (3.21)$$

If the self-consistency cycle converges, the symmetry used as input is conserved in these cases. As a result we obtain, e.g., the broken $\pi/2$-rotational symmetry and the vortex-solutions presented above. Reviewing our results with real order parameters under this point of view reveals that these solutions have the structure of a linear combination of vortex-solutions. If one defines, analogously to the two-dimensional one-particle rotationally symmetric problem, a number for the total angular momentum m, it becomes obvious that in fact the solutions with vortices may be understood in this sense. Analogously to a BEC, they carry angular momentum. The real solutions have the same structure as a linear combination of m and $-m$. While a global phase rotation does not influence the absolute value of the order parameter in the complex case, the real solution has minima and maxima in azimuthal direction, which explains the angle-dependence of the magnetization, which is not found in the complex case. This also explains, why these non-rotationally symmetric solutions occur only in the high-filling regime. Since a vortex requires the order parameter to vanish in its core, no vortex will occur in the trap center if filling is far away from full filling. This effect should be restricted to systems with a superimposed strong optical lattice as a consequence of the one-band physics. Without the lattice, the order parameter is maximal in the trap center [53]. It is also remarkable that the solutions with a highly oscillating order parameter found in Ref. [74] and found in this work in Figure (3.19)(a)-(c) do not belong to any $m > 0$ class although the order parameter has sign-changes in radial direction.

Furthermore, it is worth mentioning that the convergence of our algorithm is optimal if one has a balanced system or if the system is normal. Both superfluid and magnetized systems require the 3-4 fold number of iteration steps in order to converge. It is not always possible to compare the grand potential difference between a superfluid and the corresponding normal state at the same parameters if the Hartree terms are included. For translationally invariant systems, this is no problem (see chapter (2)). Since we are not making any assumptions on the order parameter, numerical errors may tend to stabilize the CDW-phase if one assumes $\Delta(\mathbf{i}) = 0$, or the algorithm simply does not converge. The CDW-phase may be a numerical solution of the self-consistency equations, but the competing superfluid solution will always have a lower grand potential at symmetric hopping. Therefore, the CDW-phase is unphysical here.

3.6 Spin-dependent hopping

As discussed in the introduction, the hopping-term in the Hamiltonian may be spin-dependent. In this section, we perform calculations for this case. As argued in chapter 2, in a translationally invariant system at half filling with $\Delta\mu = 0$ and $t_\uparrow \neq t_\downarrow$, the ground state of a system

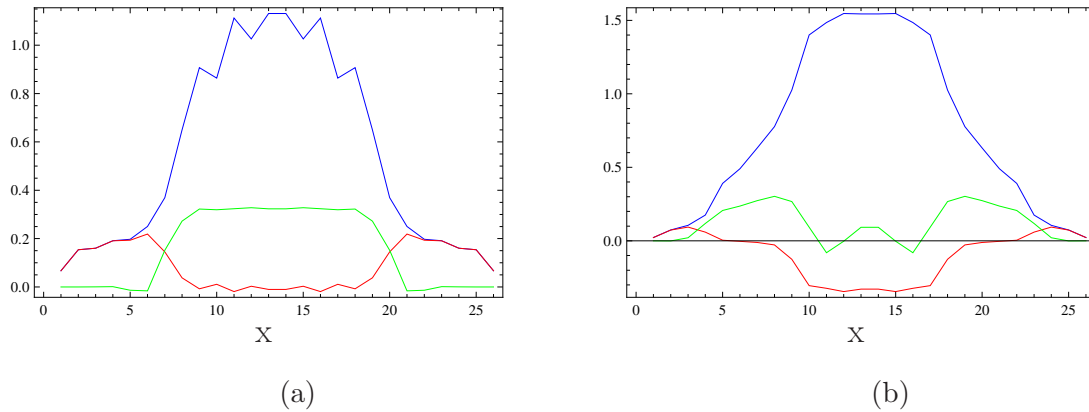|	
(a)	(b)

Figure 3.21: Superfluid order parameter (green), magnetization (red) and particle density (blue) on a 26×26 square lattice. The system parameters are chosen to be $U = -2.4$, $V = 0.01$, $\mu = -1.1$, $\beta = 1000$, $t_\downarrow = 0.3$ and (a) $\Delta\mu = 0$ (b) $\Delta\mu = -1.4$ in units of $t_\uparrow$.

is definitely not superfluid. A CDW-phase occurs instead, even at a minimal imbalance in the hopping-terms. Hence, we want to see what happens when the trapping potential V and a Zeeman term $\Delta\mu \neq 0$ is present. In the following, we always assume $t_\downarrow < t_\uparrow$.

At first, a view on the modified Hamiltonian (3.1) is useful. Formally the Hamiltonian for spin-dependent hopping still keeps the same form, with the replacement $t \rightarrow t_\sigma$. It is a priori clear that the symmetry relation for the DOS (3.13) needs not to be valid, since the structure of the derived Hamilton-matrix does not have the form of (3.11). Hence, a symmetric DOS does not necessarily occur at any value of $\Delta\mu$. The difference in the hopping-terms may cause an imbalance at $\Delta\mu = 0$. This becomes clear with the use of a simple LDA argument, as follows: the bandwidths of the two spin-species are different, and the chemical potential is space-dependent. Hence, at half filling ($\mu(\mathbf{i}) = U/2$) no particle imbalance is expected. At fillings lower than half the "↑"-species represents the majority-spin, while at lower fillings it represents the minority-spin. This leads to a space-dependent magnetization, which may have a sign change as function of $\mathbf{i}$. These arguments will be confirmed in our numerical results.

In order to decide whether a system is in a CDW- or in a superfluid state or even in a mixture, we always perform our calculations with the starting conditions $\Delta(\mathbf{i}) = 0$, and compare the grand potential with results for the condition $\Delta(\mathbf{i}) \neq 0$. Typical results are shown in Figures (3.21) and (3.22). Although our calculations were performed at strong asymmetry, the pure CDW-state never minimized the grand potential. In Figure (3.21)(a) a system with $\Delta\mu = 0$ is presented. Note that here superfluidity and CDW-behavior occur as well. The CDW-behavior is visible in the spatial oscillation of the total particle density. The total particle density is not a monotonic function of $\mathbf{i}$ here. The superfluid order parameter is positive in the region where its absolute value is not negligible in comparison to its maximum $[|\min\{\Delta(\mathbf{i})\}|/\max\{\Delta(\mathbf{i})\} \approx 8\%]$. In Figure (3.21)(b) we have chosen $\Delta\mu = -1.4$ and obtained an approximatively balanced system. Here, the CDW-behavior vanishes, and a pure superfluid state appears to be thermodynamically stable. Although the system is nearly balanced, significant sign changes occur in $\Delta(\mathbf{i})$. In this case, one obtains $|\min\{\Delta(\mathbf{i})\}|/\max\{\Delta(\mathbf{i})\} \approx 53\%$. So we conclude that sign changes in the superfluid order parameter are rather a feature of $\Delta\mu \neq 0$ than a consequence of a particle number imbalance, in general. At symmetric hopping, as shown above, one obtains automatically a balanced system at $\Delta\mu = 0$. Hence, in this case the sign change in $\Delta(\mathbf{i})$ is always associated with a particle imbalance.
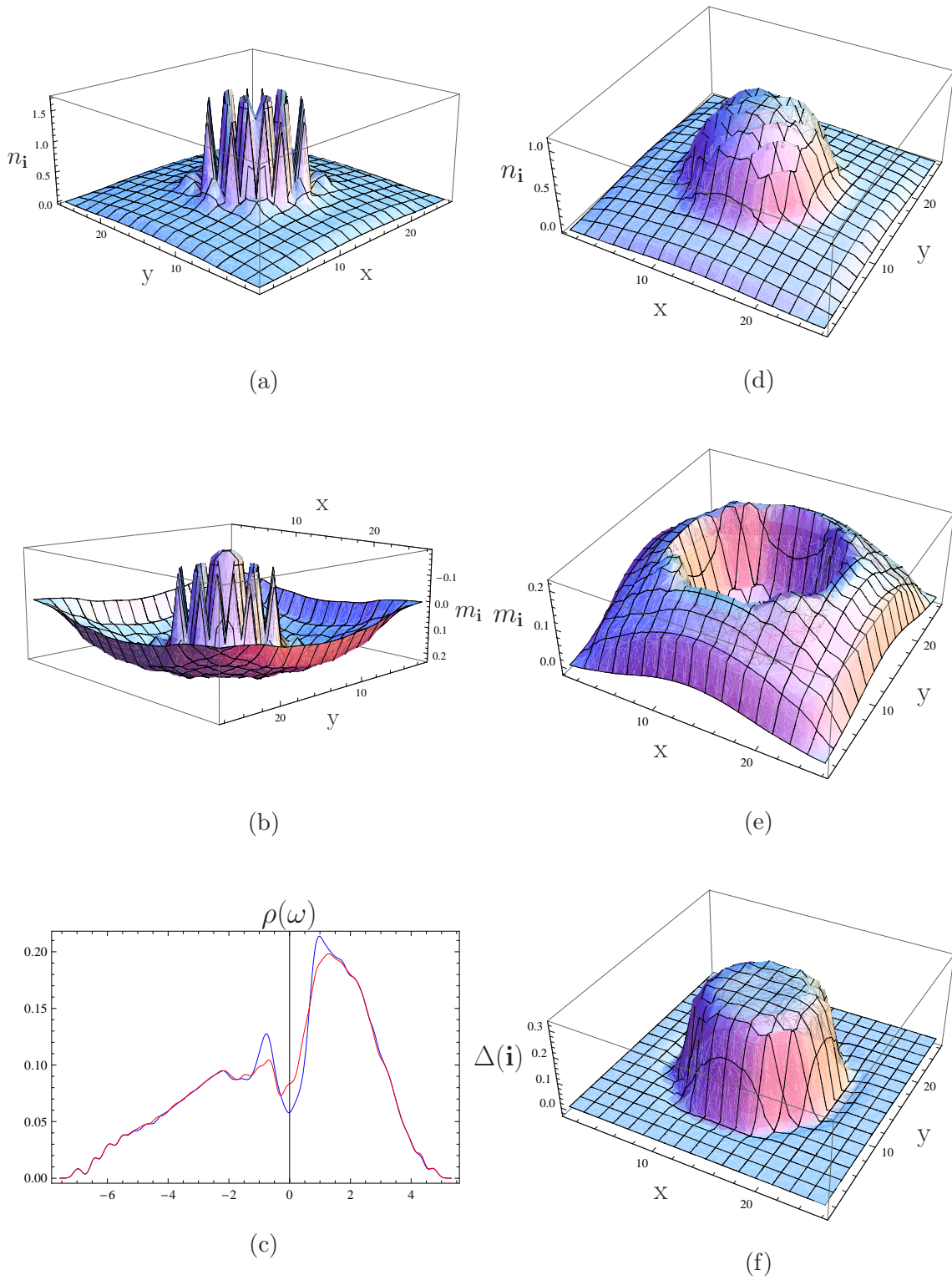
Figure 3.22: Comparison of numerically stable superfluid to a CDW-state on a 26×26 lattice. The system parameters are $U = -2.4$, $V = 0.01$, $\mu = -1.1$, $\Delta\mu = 0$, $\beta = 1000$ and $t_\downarrow = 0.3$ in units of $t_\uparrow$. In (a)+(b) the CDW-phase is presented, and in (d)-(f) the superfluid one. In (c) the DOSs of both systems are shown. The red (blue) curve corresponds to the CDW (superfluid) phase. Superfluidity minimizes the grand potential at this parameter setting.

Further numerical investigations did not yield a thermodynamically stable CDW-phase in a trapped system. A comparison of the DOSs of the superfluid and the CDW-state [Figure (3.22)(c)] reveals that in this parameter regime we are far away from having a non-superfluid state to minimize the grand potential. The minimum in the DOS of the superfluid at the Fermi edge is much deeper than that of its competing phase, and the spectral weight of deeply bound states (negative energy in the plot) is obviously higher. One would have to further increase the hopping asymmetry in order to stabilize the non-superfluid phase. Note here that the Hartree-Fock approximation becomes bad at very strong hopping imbalance. The on-site second order diagrams (explained extensively in chapter 5), which include fluctuations neglected here for the narrow band, are $\mathcal{O}(U^2/t_\sigma)$. Hence they diverge at sufficiently small $t_\downarrow$. Also, the convergence behavior becomes drastically bad in Hartree-Fock if one decreases $t_\downarrow$ further. Maybe this is why we did not find a thermodynamically stable CDW-phase. We gave up the search for a thermodynamically relevant CDW-state, because at the moment there is no interest documented in literature for finding CDW-states experimentally. Nevertheless, we describe the features of a trapped CDW-phase since it is, of course, in the positive sense of "academic interest".

A typical CDW-configuration is shown in Figure (3.22). In (a) the total particle density and in (b) the magnetization is shown. Both quantities reveal the staggered features of the broken $\mathbb{Z}_2$-symmetry. Although antiferromagnetism is known to occur only in systems with repulsive on-site interaction strength, the combination of the attraction between the particles and the imbalance arising due to the hopping-asymmetry leads to an effective staggered magnetization in z-direction. Since we treat antiferromagnetism extensively for the repulsive-U model in chapter 4, we refer to that chapter emphasizing the importance of the experimental detection schemes assuming z-antiferromagnetism described there. From this point of view, the CDW-phase may be an interesting topic for an experimental realization.

3.7 Comparison to LDA results

As the last point in this chapter we present results from the literature obtained in the LDA-approximation in order to compare them with the results obtained in this work from an exact treatment of the trapping potential. As mentioned above, the LDA is not capable of describing a trapped imbalanced system qualitatively correctly. A typical LDA-distribution of particle numbers and values of the superfluid order parameter, taken from Ref [72], are shown in Figure (3.23). As explained in chapter 2, in those LDA-results complex ansatzes for translationally invariant systems of the type $\Delta(\mathbf{i}) = |\Delta| \exp(i\,\mathbf{q} \cdot \mathbf{i})$ have been used in order to make predictions for trapped systems. Of course, it suffices to present LDA-results in the two-dimensional representation since there is no azimuthal dependence on the trapping potential $[\mu(\mathbf{i}) = \mu(|\mathbf{i}|)]$ in a rotationally invariant harmonic trap. There are similarities and differences between the LDA- and the exact results. The similarities are the following:

- The spatial dependence of the total particle densities do not display any features arising from spontaneous symmetry-breaking.

- Superfluidity and polarization "repell" each other. Spatial regions with a high absolute value of the superfluid order parameter are by trend lower magnetized than regions with a low $|\Delta(\mathbf{i})|$.

- Results for balanced systems reveal exactly the same qualitative features with a real and positive superfluid order parameter, which is maximal in the region of half filling.

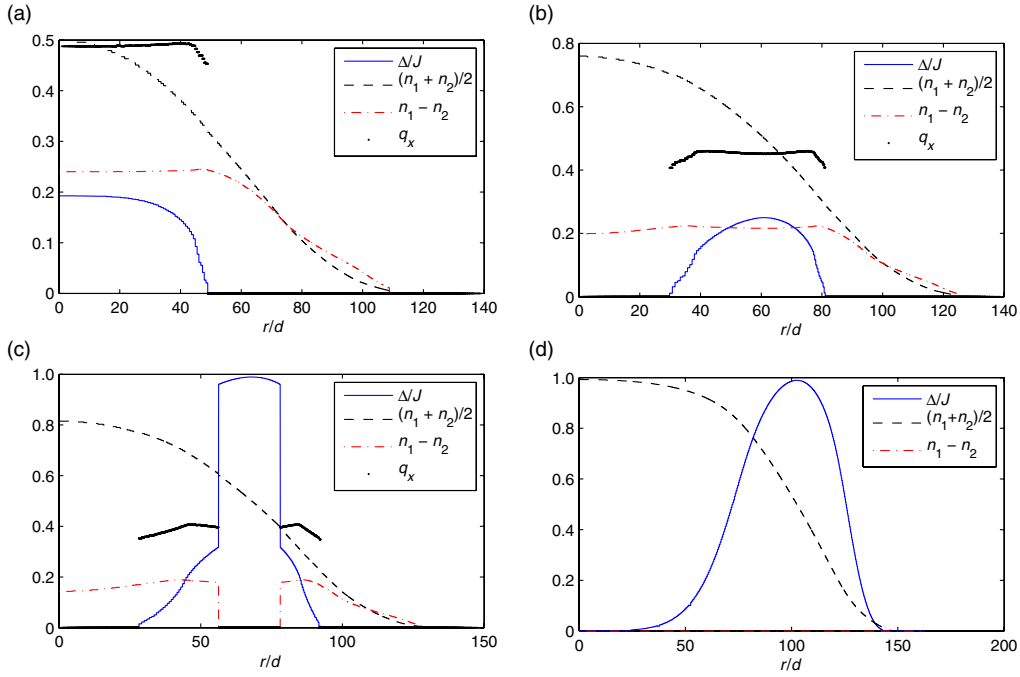The differences of the results obtained in the two methods are drastic:

Figure 3.23: LDA-results taken from Ref [72]. In the plots, the total particle densities, the magnetization, and the values of the superfluid order parameter $|\Delta|$ and of $\mathbf{q}$, used as an ansatz, are shown. In (a), the density in the trap center is $n_{\text{Center}} \approx 0.5$, while in (b)-(d), the density is higher. In (c), $\Delta\mu$ is smaller than the gap of the balanced superfluid at half filling. In (d), the system is unpolarized. Regions with $|\Delta| = 0$ are in a normal phase, regions with $|\Delta| \neq 0$ and $\mathbf{q} = 0$ correspond to a BCS-phase, and regions with $\mathbf{q} \neq 0$ to an FFLO phase. Phase separation appears within the LDA-approach.

- As we have shown numerically above and argued on the basis of analytical arguments in chapter 1, in the exact solution, the superfluid order parameter is a real-valued function of $\mathbf{i}$. This fact is not visible in the LDA-approach. In the exponential ansatz, used in the LDA, solutions containing simultaneously an imbalance and a real order parameter are not numerically stable. As we have seen from the exact results, it is indeed possible, that a real order parameter coexists with magnetization.

- There are no sharp edges between different phases in the exact solution. All observables appeared to be smooth functions in real-space.

- The strict phase separation presented in Figure (3.23)(c) is an artifact of the LDA-method. Also, the minima in the absolute value $|\Delta(\mathbf{i})|$ do not occur in the LDA-results. At weak polarization strengths, the regions around those minima coincide with the maxima of the magnetization.

- The most drastical defect of LDA is the absence of the azimuthal dependence of all relevant sizes, which is important at high filling. In this case, as we have shown above, a vortex-antivortex pair lies in the trap center leading to configurations of the order parameter and the magnetization which break the trapping symmetry spontaneously. Hence, especially the results presented in Figure (3.23)(b) and (3.23)(c) are questionable.

- Furthermore, it is not possible to obtain spectral functions within the LDA-formalism, as presented in this work.

So we may conclude, that the LDA is only capable to describe qualitatively correctly balanced systems and normal (non-superfluid) systems. At least the total particle densities are described qualitatively correctly within the LDA.

Until now, there is no literature treating spin-dependent hopping in combination with LDA. In this case, the LDA would fail even more drastically in describing the physically correct states occurring in a trapped system. Just in order to mention this point, the LDA would, e.g., predict a CDW-phase in the half-filled region at $\Delta\mu = 0$, and a superfluid one in regions with a different filling (see results of chapter 2). As seen above, exact treatment of the trapping potential yields completely different results with a more complicated structure of the superfluid order parameter and the magnetization.

Chapter 4

Trapped Antiferromagnetic Systems

Recently the repulsive-U fermionic Hubbard-type model was realized experimentally. E.g., the Mott metal-insulator transition has been observed experimentally [29, 30]. The experimental results of the authors cited above are in very good qualitative and quantitative agreement with previous theoretical predictions performed using the Hubbard model with exact treatment of the trapping potential [28]. Now that the Mott-transition is well understood for ultracold fermionic quantum gases, the next milestone is the experimental realization of an antiferromagnet [30, 47, 48]. It is not possible to reach sufficiently low temperatures at the moment experimentally.

In this chapter, we treat the repulsive-U Hubbard model again within the saddle-point approximation. While recent papers [45, 46] restrict consideration to antiferromagnetic states where antiferromagnetism may only occur in one direction in pseudospin space (z-antiferromagnetism), we allow the magnetic order parameter to adopt any direction[1]. The results are presented as follows: first we present the connection to superfluidity and the attractive-U model via a special particle-hole transformation. We explain the similarities and the differences between these systems. Then we present numerical results obtained in the saddle-point approximation for different magnetic configurations and discuss possibilities for experimental detection of the antiferromagnetic state. After that we compare the results with the ones obtained for the attractive-U models, and discuss basic similarities and differences between trapped and translationally invariant systems. Finally, we present the effects of spin-dependent hopping and show why the local density approximation (or Thomas-Fermi approximation) fails drastically in describing trapped antiferromagnetic systems.

4.1 Connection to the attractive-U model

As explained in the introduction, the relevant Hamiltonian describing the system at repulsive interaction is formally the same as in the attractive (1.34) case with exception of the opposite sign of the interaction. As shown in (1.34), a special particle-hole transformation converts the attractive and repulsive interaction into each other. Therefore, as shown in (1.34), in translationally invariant systems it suffices to treat one of the two interaction signs. Once those results have been found, e.g., for the attractive case, the particle-hole transformation yields results for the repulsive one. However, in our case the trapping potential $V(\mathbf{i})$ complicates the situation. While, on the one side, $V(\mathbf{i})$ may be interpreted as a space-dependent chemical potential, $V(\mathbf{i})$ acts as a space-dependent Zeeman term on the other side. Hence,

---

[1]Selected parts of this chapter have been published in: T. Gottwald and P. G. J. van Dongen, Phys. Rev. A **80**, 033603 (2009), selected for the October 2009 issue of Virtual Journal of Atomic Quantum Fluids

in order to understand antiferromagnetism on the repulsive side, new calculations have to be performed.

The results presented in this chapter are obtained with the help of a special particle-hole transformation [see Eq. (1.34)]. Our code internally converts the chemical potentials μ_σ into μ'_σ in the sense of Eq. (1.34) and performs calculations on a system with attractive interaction strength and $\sigma V(\mathbf{i})$ as a space-dependent Zeeman term. The results are transformed back after convergence.

4.2   Structure of the magnetic ordering

In order to treat antiferromagnetism it is convenient to rewrite the interaction part of the saddle-point Hamiltonian in terms of spin operators (see chapter 2 for the Hartree-Fock decoupling and chapter 3 for the Hamiltonian including the trapping potential):

$$\mathcal{H}_{U,\text{HF}} = U \sum_{\mathbf{i}} \left(2\langle \hat{n}_{\mathbf{i}} \rangle \hat{n}_{\mathbf{i}} - 2\langle \hat{\mathbf{S}}_{\mathbf{i}} \rangle \cdot \hat{\mathbf{S}}_{\mathbf{i}} - \langle \hat{n}_{\mathbf{i}} \rangle^2 + \langle \hat{\mathbf{S}}_{\mathbf{i}} \rangle^2 \right), \tag{4.1}$$

with the density and the spin operators defined as

$$\hat{n}_{\mathbf{i}} \equiv \frac{1}{2} \left(\hat{n}_{\mathbf{i}\uparrow} + \hat{n}_{\mathbf{i}\downarrow} \right), \quad \hat{\mathbf{S}}_{\mathbf{i}} \equiv \frac{1}{2} \begin{pmatrix} \hat{c}^\dagger_{\mathbf{i}\uparrow} \\ \hat{c}^\dagger_{\mathbf{i}\downarrow} \end{pmatrix} \boldsymbol{\sigma} \begin{pmatrix} \hat{c}_{\mathbf{i}\uparrow} \\ \hat{c}_{\mathbf{i}\downarrow} \end{pmatrix}, \quad \boldsymbol{\sigma} \equiv (\sigma_1, \sigma_2, \sigma_3)^T, \tag{4.2}$$

where σ_i are the Pauli-matrices. The two-operator part may be written as

$$
\begin{aligned}
\mathcal{H}, \text{two} \;=\; & -t \sum_{\langle \mathbf{ij} \rangle} \begin{pmatrix} \hat{c}^\dagger_{\mathbf{i}\uparrow} \\ \hat{c}^\dagger_{\mathbf{i}\downarrow} \end{pmatrix} \cdot \begin{pmatrix} \hat{c}_{\mathbf{j}\uparrow} \\ \hat{c}_{\mathbf{j}\downarrow} \end{pmatrix} + \sum_{\mathbf{i}} (V(\mathbf{i}) - \mu) \begin{pmatrix} \hat{c}^\dagger_{\mathbf{i}\uparrow} \\ \hat{c}^\dagger_{\mathbf{i}\downarrow} \end{pmatrix} \cdot \begin{pmatrix} \hat{c}_{\mathbf{i}\uparrow} \\ \hat{c}_{\mathbf{i}\downarrow} \end{pmatrix} \\
& + \frac{\Delta\mu}{2} \sum_{\mathbf{i}} \begin{pmatrix} \hat{c}^\dagger_{\mathbf{i}\uparrow} \\ \hat{c}^\dagger_{\mathbf{i}\downarrow} \end{pmatrix} \sigma_3 \begin{pmatrix} \hat{c}_{\mathbf{i}\uparrow} \\ \hat{c}_{\mathbf{i}\downarrow} \end{pmatrix}.
\end{aligned}
\tag{4.3}
$$

The symmetry behavior under rotations in spin-space becomes evident from this representation of the Hamiltonian. Rotations are, of course, represented by SU(2) matrices as

$$\begin{pmatrix} \hat{c}_{\mathbf{i}\uparrow} \\ \hat{c}_{\mathbf{i}\downarrow} \end{pmatrix} \to \mathcal{U} \begin{pmatrix} \hat{c}_{\mathbf{i}\uparrow} \\ \hat{c}_{\mathbf{i}\downarrow} \end{pmatrix}, \quad \mathcal{U} \in \text{SU}(2). \tag{4.4}$$

In a balanced system ($\Delta\mu = 0$), the Hamiltonian is invariant under all rotations $\mathcal{U} \in \text{SU}(2)$, while in imbalanced systems ($\Delta\mu \neq 0$) the symmetry is reduced to U(1) (rotations around the z-axis in spin-space), regardless how small the imbalance is.

From this point of view we know that any solution of the self-consistency equations may be rotated only along the z-axis in order to keep the grand potential constant. A rotation around the x- or y-axis would increase the grand potential if a minimal solution is rotated. Hence, we may assume that there is a preferred angle between the z-axis and antiferromagnetic order in an imbalanced system. In a fully SU(2)-invariant balanced system, there should be no preferred angle. We know from the Heisenberg model in a magnetic field (which arises in a strong coupling expansion at half filling) that the antiferromagnetic order is perpendicular to the magnetic field. Therefore, one may expect the same for our model, if a minimal imbalance occurs.

Nevertheless, these issues have to be addressed by numerical calculations. In the older literature [80], incommensurate antiferromagnetism is proposed to occur away from half filling

in translationally invariant systems. However, in our case the systems have a finite size and a trapping potential. It must, therefore, be checked if these older results have any relevance under these new circumstances. Furthermore, in recent literature [46], antiferromagnetism in an ultracold gas of fermions is categorically restricted to z-antiferromagnets. In further recent papers the experimental detection of this phenomenon assumes the z-axis as the preferred direction for Néel-states parallelly to the quantization axis [87, 88]. Therefore, we present numerical results for various quantities assuming different ordering types. Finding different configurations, we compare the grand potentials of the different solutions in order to decide which one is the thermodynamically stable one.

4.3 Numerical results

Analogously to the procedure used to describe fermionic superfluidity within the saddle-point approximation, Hamiltonian (4.1)+(4.3) yield self-consistency equations. With the same procedure as used in chapter 3, one can rewrite the Hamiltonian in matrix-form as:

$$\mathcal{H} = \begin{pmatrix} \hat{\mathbf{c}}_\uparrow^\dagger \\ \hat{\mathbf{c}}_\downarrow^\dagger \end{pmatrix}_{2\mathcal{N}} \cdot \begin{pmatrix} H_{0\uparrow} & U\langle\hat{\mathbf{S}}_-\rangle \\ U\langle\hat{\mathbf{S}}_+\rangle & H_{0\downarrow} \end{pmatrix}_{2\mathcal{N}\times 2\mathcal{N}} \cdot \begin{pmatrix} \hat{\mathbf{c}}_\uparrow \\ \hat{\mathbf{c}}_\downarrow \end{pmatrix}_{2\mathcal{N}} \quad , \tag{4.5}$$

where $H_{0\sigma}$ contains the terms of the interaction-free Hamiltonian part (4.3), and the Hartree-terms of (4.1) and $\hat{\mathbf{S}}_{\pm,\mathrm{ij}} \equiv \delta_{ij}(\hat{S}_{\mathrm{x,i}} \pm i\hat{S}_{\mathrm{y,i}})$ contains the Fock-terms of Hamiltonian part (4.1). Analogously to the superfluid case, the self-consistency conditions at inverse temperature β are given as

$$\langle \hat{n}_{\mathbf{i}\sigma} \rangle = \sum_{s=1}^{2\mathcal{N}} |u_{\mathbf{i}s,\sigma}|^2 f_\beta(E_s) \tag{4.6}$$

$$\langle \hat{S}_{\mathbf{i}+} \rangle = \sum_{s=1}^{2\mathcal{N}} u_{\mathbf{i}s,\uparrow}^* u_{\mathbf{i}s,\downarrow} f_\beta(E_s) \, , \tag{4.7}$$

where $u_{\mathbf{i}s,\sigma}$ are the components of a unitary transformation diagonalizing (4.5), E_s are the eigenvalues of the matrix in (4.5), $\mathcal{N}$ is the total number of lattice sites and $f_\beta(x) \equiv [1 + \exp{(\beta x)}]^{-1}$ is the Fermi function. Within this formalism, we perform calculations for balanced and imbalanced mixtures looking for antiferromagnetic phases with magnetic order parameters in arbitrary directions.

In order to find the different phases considered above, it is necessary to choose adequate starting values for $n_{i\sigma}$ and S_{i+}. If one wants to find the staggered magnetization in the z-direction, it is useful to break the $\mathbb{Z}_2$-symmetry by starting with a spatially oscillating occupation number $n_{\mathbf{i}\uparrow,0} - n_{\mathbf{i}\downarrow,0} = (-1)^{\mathbf{i}} m_0$. Initiating with $S_{\mathbf{i}+,0} = 0$, $S_{\mathbf{i}+,0} \in \mathbb{R}$ or $S_{\mathbf{i}+,0} \in \mathbb{C}$ decides whether one ends up with an in-plane antiferromagnet or not and whether the magnetization in the plane is restricted to the x-direction or if xy-antiferromagnetism will occur. The numerical iteration process (which unavoidably suffers from small numerical errors) is desiged such as to leave the initially chosen symmetry class of the desired solution invariant in this regard.

Since recent literature restricts consideration to pure z-antiferromagnets, we present results for those structures as well as results for more general ones. As argued above, we choose $S_{\mathbf{i}+,0} = 0 \, \forall \, \mathbf{i}$ in order to obtain a pure z-antiferromagnet. A weak antiferromagnetic field is superimposed in the first iteration step in order to break the rotational symmetry. Proceeding that way, we are able to reproduce qualitatively the results obtained in Refs. [45, 46].
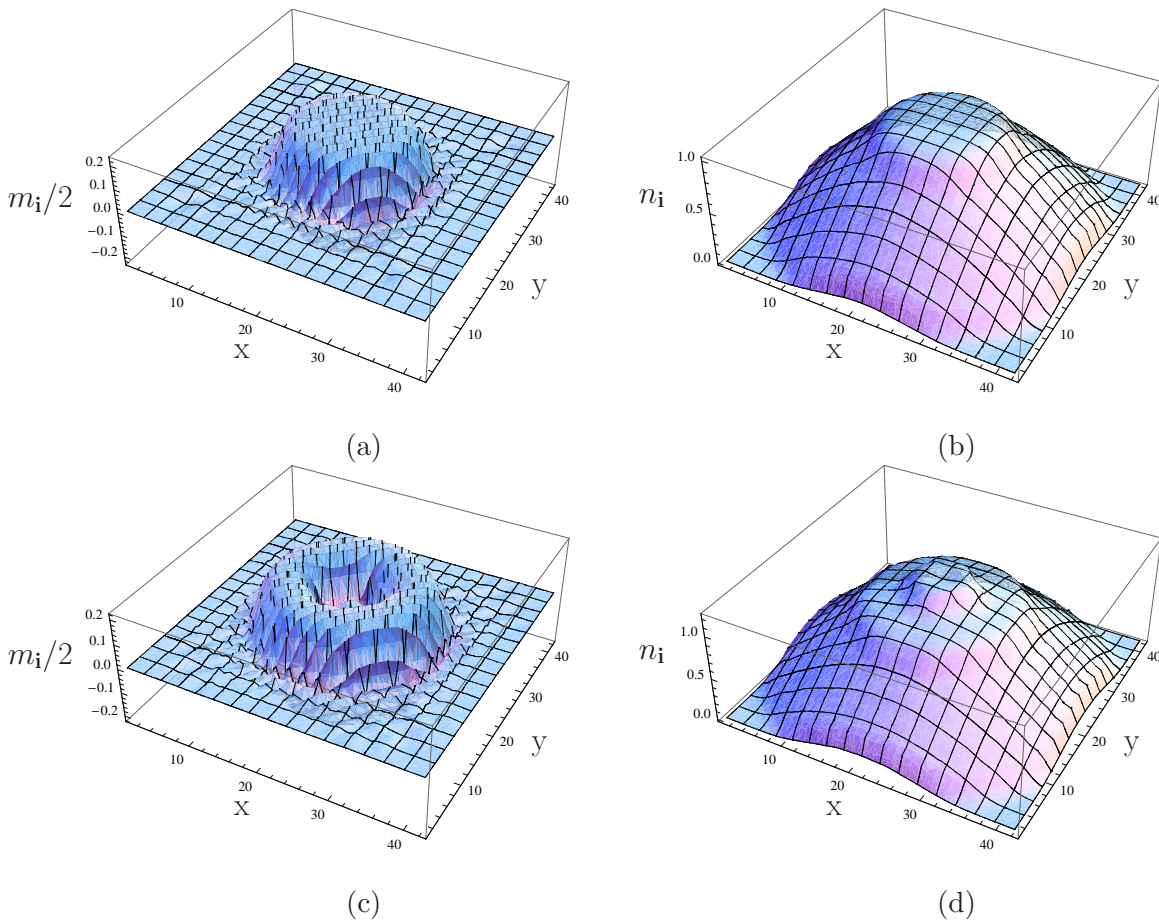
(a)

(b)

(c)

(d)

Figure 4.1: Magnetization and particle density of a z-antiferromagnet on a 42×42 square lattice. The system parameters are chosen to be $U = 2.4$, $V = 0.01$, (a)+(b) $\mu = 1.5$ (c)+(d) $\mu = 2.0$, and $\beta = 1000$ in units of t. The system is balanced ($\Delta \mu = 0$), and the filling in the center is (a)+(b) $n_{\mathrm{Center}} \approx 1$ (c)+(d) $n_{\mathrm{Center}} > 1$.

Results for balanced systems are presented in Figure (4.1) in the three-dimensional representation. Since certain details we wish to resolve are not visible in the three-dimensional representation, we present slices in the middle of the xy-plane in Figure (4.2). Furthermore, we present the numerical results for the DOS and discuss the typical features distinguishing an antiferromagnetic from a paramagnetic state.

At first we discuss balanced systems. Typical results are presented in Figure (4.2). In (4.2)(a), the center of the trap is approximatively half filled ($n_{\mathrm{Center}} \approx 1$), while in (b) results for $n_{\mathrm{Center}} > 1$ are presented. The first feature we want to emphasize, the magnetization, is always aligned (anti-)parallelly to a globally defined direction $\mathbf{m}$. The direction of $\mathbf{m}$ does not influence the grand potential and is physically chosen by spontaneous symmetry breaking. Of course, in our calculations we may decide in which direction $\mathbf{m}$ points by choosing the corresponding starting values of $n_{\mathbf{i}\sigma}$ and $S_{\mathbf{i},+}$. Since we always obtain the same amplitudes for the projection of the local magnetization on $\mathbf{m}$ (regardless of the direction of $\mathbf{m}$), we show only the results for the z-antiferromagnets. This fact is in accordance with the full SU(2)-symmetry underlying spin-balanced systems. The full SU(2)-symmetry is spontaneously broken. As a further result we obtain that the spatial region where the antiferromagnet lies displays a broadening of the half-filled regime. Figure (4.1)(b) clearly displays a half-filled plateau in the trap center where the antiferromagnetic ordering is maximal. In Figure (4.1)(d), the
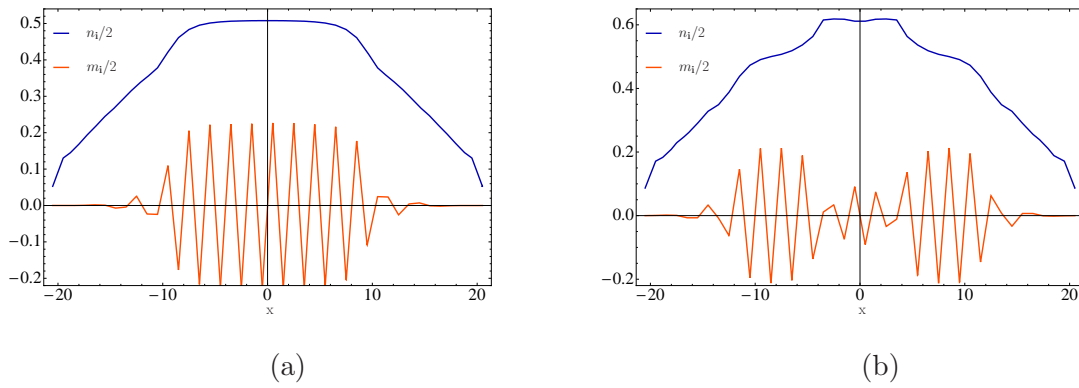
Figure 4.2: Slices through the xy-plane, on y-position 20, of the systems presented in Figure (4.1). Panel (a) corresponds to the lower total filling, and panel (b) to the higher total filling.
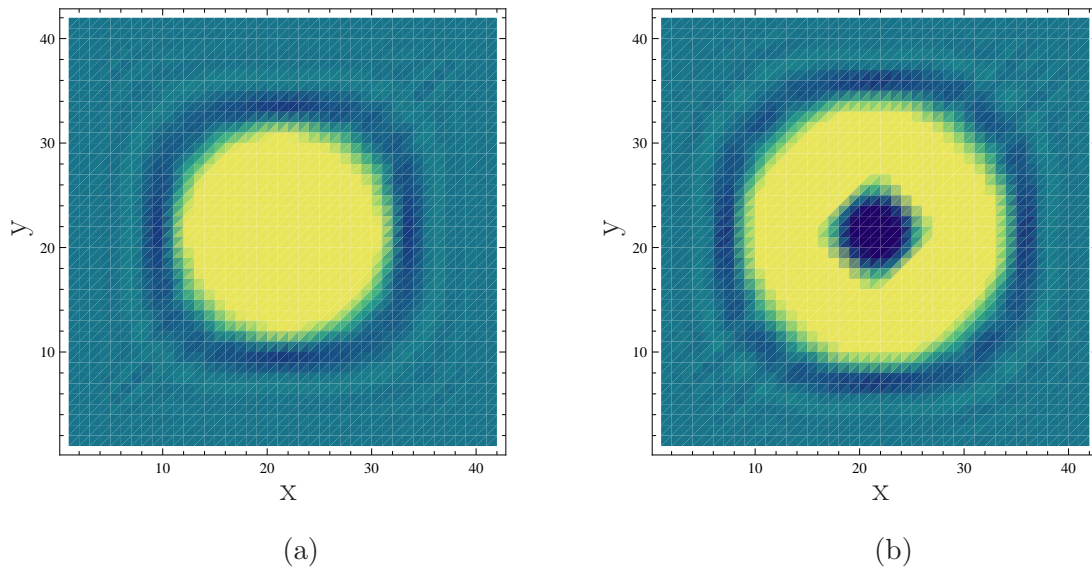

Figure 4.3: Staggered order parameter $(-1)^{\mathbf{i}} m_{\mathbf{i}}$ for low filling (a) and for high filling (b). The yellow (blue) regions indicate a positive (negative) staggered order parameter. The order parameter vanishes at the boundaries (green region). Domain-wall formation is revealed in these plots.

maximally ordered phase does not lie in the trap center. In this case the total filling is higher and, therefore, a wedding-cake structure appears. The higher-filled trap center is surrounded by a half-filled, strongly ordered ring.

A further feature at ultralow temperatures is a domain-wall formation. As presented in Figure (4.3), the staggered magnetization $(-1)^{\mathbf{i}} m_{\mathbf{i}}$ has sign changes in radial direction exactly where the filling changes from half filling to a lower or higher value. At the domain-walls the spins of nearest neighbors are aligned parallelly. These results seem to be in contrast to the prediction of incommensurate antiferromagnetism suggested by Schulz in Ref. [80]. However, this discrepancy may be explained with the results presented in section (1.4.6). Since the system is trapped, the magnetic order parameter has a globally defined direction, as derived via a mapping on the repulsive-U model [section (1.4.6)] and found in our numerical calculation without any exception. Schulz, in contrast to us, treated translationally invariant systems, where our results derived in section (1.4.6) do not apply. Hence, the trapped antiferromag-
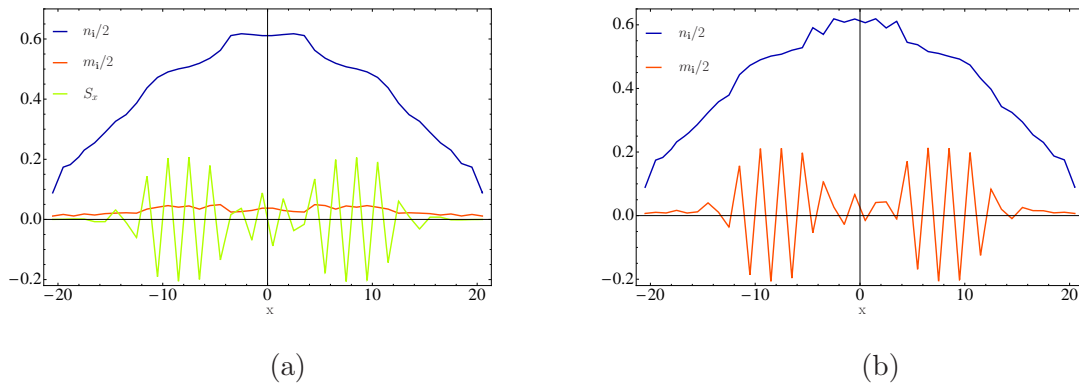
(a)

(b)

Figure 4.4: Slices through the xy-plane, on y-position 20, of a system with parameters presented in Figure (4.2) with exception of $\Delta\mu = 0.2$. In (a) x-antiferromagnetism is allowed, while in (b) the magnetization is restricted to the z-axis.

netic Hubbard model versus the translationally invariant one with infinite extension is a good example how drastically the finite size of a system influences the physical behavior.

In order to obtain an imbalance between both spin species, we turn on a Zeeman term of the form $\frac{1}{2}\Delta\mu(\hat{n}_{\mathbf{i}\uparrow} - \hat{n}_{\mathbf{i}\downarrow})$ in our grand canonical Hamiltonian. In Ref. [46], the imbalanced antiferromagnet is restricted to the z-direction. Here again, we perform calculations with the order parameter aligned parallelly and perpendicularly to the quantization axis. As argued above, one would a priori expect the direction of the antiferromagnetic ordering to be perpendicular to the z-axis. Results for a weak imbalance ($\Delta\mu = 0.2$) are shown in Figure (4.4) where in (a) the antiferromagnetic ordering is parallel to the x-axis, and in b) it is parallelly to the z-axis. In both cases we find a numerically stable antiferromagnetic solution. In (a) the x-component of the magnetization turns out to be antisymmetric in real-space, while the z-component is symmetric and positively definite. The total particle number is also an even function of **i**. In contrast to the x-antiferromagnet, in (b) the x-component of the magnetization vanishes as a consequence of the block-diagonal Hamilton-matrix. Neither the magnetization nor the total particle density are (anti-)symmetric in real space. The total particle density shows wiggles in the spatial region which is half filled. As expected from the symmetry relations, a comparison of the grand potentials shows that the x-antiferromagnet is thermodynamically stable. The wiggles, which are an artifact of the suppression of the canted antiferromagnet, are therefore an unphysical feature. The total particle density in Figure (a) still shows a broadening of the half-filled region, as was also found in the balanced case.

A system with a stronger imbalance ($\Delta\mu = 0.6$) is shown in Figure (4.5), again in (a) the x-antiferromagnet is allowed and in (b) it is suppressed. While the x-antiferromagnet is still numerically stable and lowers the grand-potential, the z-antiferromagnet is not stable at this imbalance strength, hence in (b) the normal phase appears. Here, there is no plateau-behavior in the total particle-density. A comparison of (a) and (b) shows that the z-component of the magnetization is only weakly influenced by the fact whether the system is in a xy-antiferromagnetic state or in a normal one.

In summary, for the trapped antiferromagnet at low temperatures, we obtain the following findings:

- In balanced systems, we obtain antiferromagnetic solutions of the self-consistency equations. The direction of the magnetic ordering may be freely chosen without influencing the grand potential. Broadening of the spatial regions with half filling occurs.
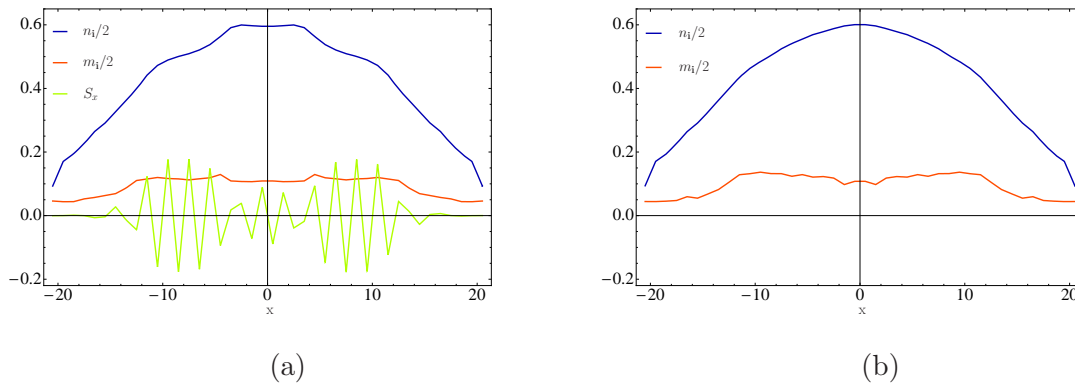
(a)   (b)

Figure 4.5: Slices through the xy-plane, on y-position 20, of a system with parameters presented in Figure (4.2) with exception of $\Delta\mu = 0.6$. In (a) x-antiferromagnetism is allowed, while in (b) the magnetization is restricted to the z-axis. In this parameter regime no z-antiferromagnet is numerically stable.

- In imbalanced systems, the antiferromagnetic order parameter is oriented perpendicularly to the quantization axis in thermodynamically stable solutions. Rotating the staggered magnetization around the z-axis does not influence the grand potential, according to the remaining U(1)-symmetry.

- Broadening of the half-filled region is still observable in the imbalanced case, but it is smeared out with increasing imbalance.

- Observables gaining their behavior from spontaneous symmetry breaking (i.e., xy-components of the spin and the z-component in the balanced case) are antisymmetric functions of the position $\mathbf{i}$. The other observables presented (i.e., the total particle density and the z-component of the spin in the imbalanced case) have an even symmetry in real-space, if the solution of the self-consistency equations lowers the grand potential.

- Domain-wall formation occurs as presented in Figure (4.3), irrespective of whether the system is balanced or not.

4.4 Temperature dependence and DOS

In the previous section, we treated our systems at a very low temperature $1/T \equiv \beta = 1000$. The properties are basically identical to those of systems in the ground state at such low temperatures, since the lowest absolute values of the eigenenergies are of the order of $10^{-3} - 10^{-2}$ depending on the system parameters. Hence, the Fermi functions do not differ qualitatively from the unit step function. One obtains

$$\max_{\{s\}} |f_{1000}(E_s) - \Theta(-E_s)| < \exp(-10) . \tag{4.8}$$

As a consequence, the occupation numbers and order parameters are quasi identical to the ones in the ground state.

In this section we will present the temperature dependence and the densities of states for an example of a balanced system. From this point of view, there is no qualitative difference from imbalanced ones, except that the order parameters and the Néel temperature are always lower than in a balanced system with the other parameters kept fixed. Remarkably, the main
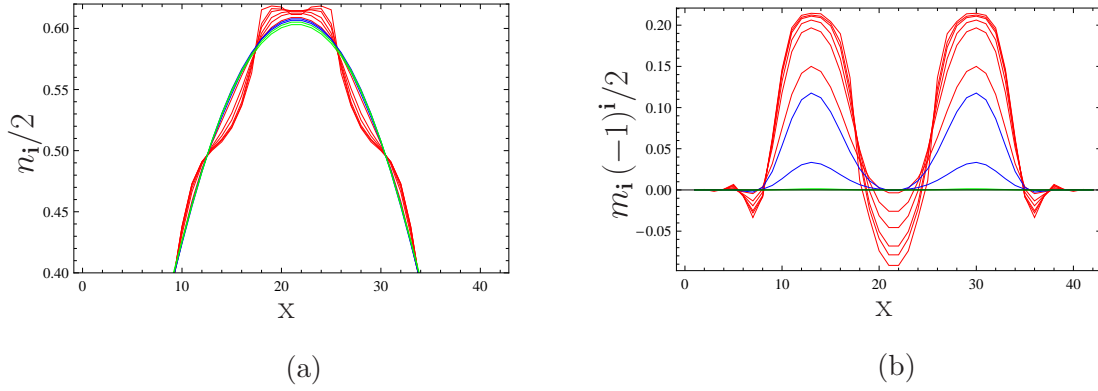
(a)

(b)

Figure 4.6: Total particle densities and staggered magnetization for different temperatures. The maximal amplitude of the staggered magnetization decreases with decreasing inverse temperature, where the inverse temperatures are in detail: $\beta = 1000$, $\beta = 20$, $\beta = 15$, $\beta = 10$, $\beta = 7.5$, $\beta = 5$, $\beta = 4.5$, $\beta = 4$, $\beta = 3.5$ and $\beta = 3$. The rest of the parameters is chosen to be as in Figure (4.1)(c)+(d). The colors are chosen as follows: $\beta > \beta_C$: red, $\beta_C > \beta > \beta_N$: blue and $\beta_N > \beta$: green.

features presented above are valid over a broad range of values of β. Results for the total particle density and the magnetization are presented in Figure (4.6). The broadening of the half-filled region is of course smeared out with a decreasing β, but still holds down to values of $\beta_C \approx 4.2$. Interestingly, the order parameter in the region near half filling does hardly decrease for decreasing $\beta > \beta_C$. In contrast, the order parameter in the higher/lower filled domains decreases continuously. For $\beta < \beta_C$ only the half-filled domain remains antiferromagnetic. The domain-wall structure does not survive in this region in the sense that the regions where the staggered magnetization $(-1)^{\mathbf{i}} m_{\mathbf{i}}$ has the opposite sign than in the half-filled region, shrink drastically (blue region in Figure (4.3)). Of course, we cannot exactly say if there is an additional phase transition at β_C or if a cross-over behavior occurs here. The situation is similar to the FFLO-BP phase transition for translationally invariant systems shown in Figure (2.2) where magnetized superfluidity with real and positively definite order becomes possible when the temperature is increased. The order parameter near the half-filled region decreases continuously for decreasing $\beta < \beta_C$ down to the Néel temperature, which is $\beta_N \approx 3.7$. Since the self-consistency equations cannot be solved analytically, there is no analogous analytical expression for β_N, as it is the case for translationally invariant systems (see, e.g., [67]). We can only estimate the Néel temperature by observing for which values of β the magnetic ordering vanishes. The temperature dependence of the total particle density and the magnetization is shown in Figure (4.6). Note at this point that the convergence behavior near the Néel temperature deteriorates drastically, so that we avoided a precise prediction of β_N in this section. We will readdress the Néel temperature in chapter 5. Furthermore, we do not present sizes such as the magnetic order parameter and the Néel temperature et cetera for different parameter regions, since a parameter scan in the weak coupling regime does not reveal any further qualitative features.

An additional observable, which is also relevant for experiments, is the DOS. We present different DOSs for the following scenarios in Figure (4.7):

- the balanced antiferromagnet at $\beta > \beta_C$,

- the balanced antiferromagnet at $\beta_C > \beta > \beta_N$,

- the balanced normal phase at $\beta_N > \beta$,
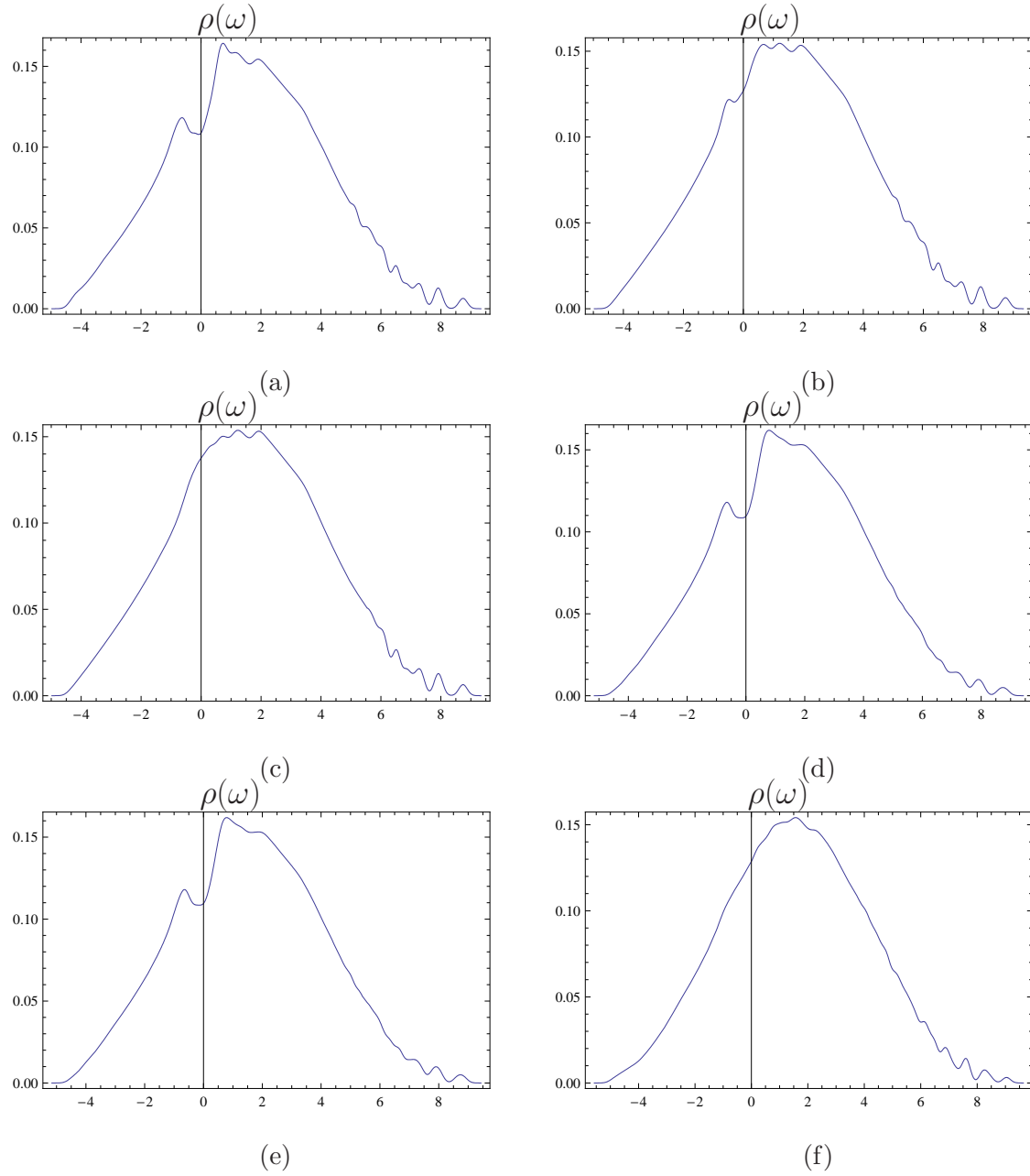
Figure 4.7: Densities of states for different parameter settings. The system parameters are chosen as in Figure (4.1) with exception of $\Delta\mu$ and β. In (a)-(c), the systems are balanced. In (a), we have $\beta > \beta_C$. In (b), a DOS typical for $\beta_C > \beta > \beta_N$ is shown. In (c), we choose $\beta_N > \beta$. In (d) and (e) we choose $\beta = 1000$ and $\Delta\mu = 0.2$ where in (d) we allow and in (e) we suppress x-antiferromagnetism. In (f) we also choose $\beta = 1000$ but $\Delta\mu = 0.6$, and we again suppress x-antiferromagnetism. Note that the DOSs in (e) and (f) do not correspond to thermodynamically stable solutions.

- the imbalanced x-antiferromagnet at $\beta = 1000 > \beta_C$

- the imbalanced (unphysical) z-antiferromagnet at $\beta = 1000 > \beta_C$ and

- the imbalanced normal phase at $\beta = 1000 > \beta_C$.

Herewith we are able to distinguish the different phases with the help of their corresponding DOS, rather than the spatially resolved particle distribution and magnetization. The features arising from a spontaneous symmetry breaking in the saddle point approximation appear in the vicinity of the Fermi edge ($\omega = 0$) as it is the case for fermionic superfluidity. In this chapter, the DOSs have been presented analogously to chapter 3 according to Equation (3.15) with $\sigma = 0.2$. In translationally invariant systems the antiferromagnetic state is characterized by a gap at the Fermi edge. This feature is not that much pronounced in the case of the trapped antiferromagnet. In Figure (4.7)(a) a minimum of the spectral function appears at the Fermi edge for a balanced antiferromagnet at $\beta > \beta_C$. As the temperature is increased in the region $\beta_C > \beta > \beta_N$, the minimum is smeared out [Figure (4.7)(b)]. The Fermi edge does not lie in the cavity caused by the antiferromagnetic minimum any more. Nevertheless, the magnetic order parameter in the half-filled region is of nearly the same size as it is for $\beta > \beta_C$, while the order parameter away from half filling is drastically reduced. The depletion of the order parameter away from half filling and the displacement of the Fermi edge from the cavity around the local minimum of $\rho(\omega)$ both occur approximatively at β_C. In Figure (4.7)(c), a typical DOS for a balanced system with $\beta < \beta_N$ is shown. Here, the DOS is monotonically increasing in a wide range around the Fermi edge. Hence, the appearance of a minimum of the DOS in the vicinity of $\omega = 0$ may be interpreted as a signature of antiferromagnetic ordering in the weak coupling regime. In the strong coupling regime one has to take into account the Mott-transition, which is not magnetic and is addressed in the next section.

Another effect (besides temperature decreasing the antiferromagnetic ordering) is the spin-imbalance, as we have shown above. In Figure (4.7)(d), the DOS of a x-antiferromagnet at ultralow-temperatures ($\beta > \beta_C$) is shown in comparison to a (unphysical) z-antiferromagnet in (4.7)(e). Both DOSs have been calculated at the same parameters with an imbalance strength of $\Delta\mu = 0.2$. Both DOSs reveal again the deep cavity in the vicinity of $\omega = 0$ as it is the case in the balanced system. Again, a broadening of the half-filled region coincides with the cavity. Interestingly, the DOSs of the physical x-antiferromagnet and of the numerically stable but unphysical z-antiferromagnet do not have drastically different qualitative features. In Figure (4.7)(f), the numerically stable DOSs in the normal phase at $\Delta\mu = 0.6$ is shown. No antiferromagnetism occurs at all in this system, and again there is no minimum in the vicinity of the Fermi edge. Hence, we may summarize:

- Deep cavities in the vicinity of the Fermi edge coincide with an antiferromagnet at low temperatures, where the half-filled region is broadened by antiferromagnetism.

- A minimum of the DOS in the vicinity of $\omega = 0$ is an indicator for antiferromagnetism in the half-filled spatial region. Broadening of the half-filled region does not necessarily occur.

- The DOS is monotonically increasing in a wide range around the Fermi surface in the normal phase.

- The DOS is not a good tool for distinguishing z-antiferromagnetism from states with a canted order parameter.

4.5 Experimental application

As mentioned above, one major goal in the near future is the experimental detection of an antiferromagnet in an ultracold two-component fermionic mixture [30, 47, 48]. The fo-
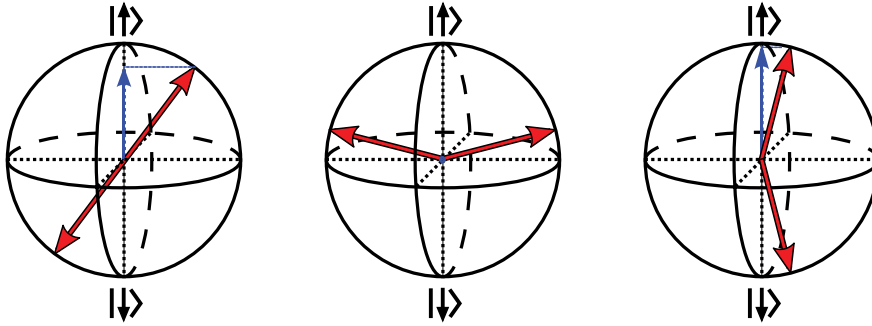
Figure 4.8: Bloch sphere representation of different antiferromagnetic states taken from Ref. [52]. Left: balanced situation, middle: imbalanced situation, right: optimal case of imbalanced situation after $\pi/2$-pulse.

cus of a multitude of recent literature was exclusively on the realization and detection of z-antiferromagnets [45, 46, 87, 49]. As we point out in our work, antiferromagnetism does not necessarily occur parallelly to the quantization axis. While in a balanced system the z-component of the antiferromagnetic order parameter is allowed to be non-zero, the amplitude is nevertheless randomly chosen by spontaneous symmetry breaking. We have shown that if there is even a minimal imbalance in the system, the z-component is strictly zero. One has always to assume at least a minimal imbalance. The spontaneously broken symmetry is the U(1)-rotation around the z-axis. Hence, e.g., the detection scheme presented in Ref. [87] will not be able to demonstrate antiferromagnetism, since it explicitly requires z-antiferromagnets to work. Here, a polarized laser beam, which excites only one of the pseudospin-species, shall pervade the atomic cloud in an experiment with its shadow revealing information about the spatial correlations of the addressed pseudospin-species. Since an in-plane antiferromagnet has no staggered order within a single spin-component, no relevant information may be acquired. Polarized lasers may not be used to distinguish between coherent linear combinations as

$$\frac{1}{\sqrt{2}}|\uparrow\rangle + \alpha|\downarrow\rangle \ , \ |\alpha| = \frac{1}{\sqrt{2}} \ , \tag{4.9}$$

which describe a perfect xy-antiferromagnet. [The direction in the xy-plane is determined by the $\arg(\alpha)$.]

A method proposed to detect antiferromagnetism independently from the direction of the magnetic order parameter is presented in Ref. [88]. Here, a pseudospin-mixing Raman-pulse is proposed to be applied on an antiferromagnetic atomic cloud. This pulse mixes both internal states and leads to a change of the momentum of the cloud. After the Raman-pulse the trap is released, and and a time-of-flight picture is taken. Doing this for different momenta $\mathbf{k}$, a reconstruction of the diagonal and the non-diagonal one-particle Green function in $\mathbf{k}$-space is possible. A Fourier transformation from $\mathbf{k}$-space to real-space is then used to calculate the ordering amplitudes. The basic problem of this method is that for [im-]balanced systems there is a remaining SU(2)[U(1)]-symmetry which is, as explained above, spontaneously broken. Hence, the different images taken for the different $\mathbf{k}$-values correspond to different Green functions, which, at least, seriously complicates the reconstruction of the ordering in real space.

As an alternative, Corcovilos et al. [52] propose to measure directly the two-particle Green function (correlation function) instead of the one-particle Green function. On the basis of
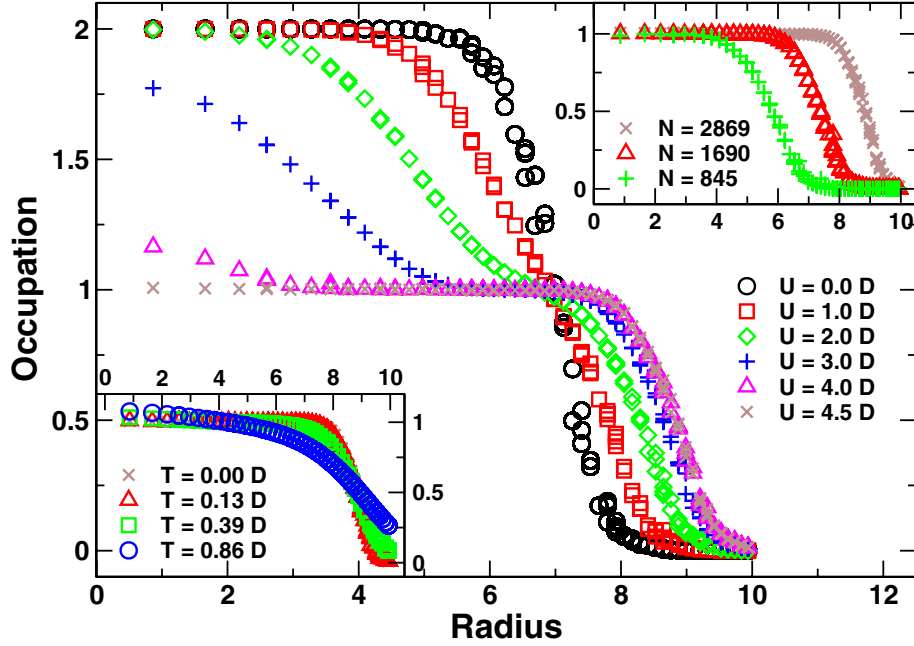
Figure 4.9: Occupation numbers obtained within R-DMFT in Ref. [28]. The phase presented here is paramagnetic, and the plateau arises due to a Mott-transition. The results presented here are for three-dimensional systems, however, qualitatively they are assumed to be the same for two dimensions. D is the half bandwidth, which is by definition $D = 2dt$. In our case we have $D = 4$. Taking into account these results, we do not expect a Mott-plateau to appear for the interaction-strength used in this chapter ($U = 2.4t$).

(among others) our previously published Ref. [89] Corcovilos et al. propose to apply a $\pi/2$-pulse on the atomic cloud in order to rotate the order parameter from the xy-plane onto the z-axis before the correlation function is measured (see Figure (4.8)). Hence, Ref. [52] also makes use of a z-antiferromagnet obtained by rotating a previously achieved state. Since the authors make use of the two-particle Green function, averaging over a multitude of single measurements does not lead to a zero expectation value, since the value which is averaged is m_z^2 rather than m_z. Due to the remaining SU(2)-symmetry in the balanced case, the signal strengths are reduced over a factor of 1/3, while in the imbalanced case the remaining U(1)-symmetry reduces the signal strength by a factor of 1/2.

An alternative method proposed by us is the use of the broadening of the half-filled region caused by the antiferromagnetic ordering. The total particle distribution is directly accessible via in-situ imaging [16, 17, 18]. One advantage of this method is that the total particle density is fully invariant under SU(2)-rotations in spin-space. Therefore, the direction of the magnetic ordering, chosen randomly by spontaneous symmetry breaking, does not influence the outcome of a single measurement.

At this point, one must pay attention to the interaction strength. If the interaction is strong, a broadening of half filling may be caused by the Mott metal insulator transition. Dynamical mean-field calculations performed within and beyond the local density approximation have been presented in Ref. [28]. As the interaction increases, the Mott-transition takes place at a value of $U_C \approx 4$ in units of t. For an interaction with $U \geq U_C$, a broadening of the half-filled region is caused in the paramagnetic phase. The existence of this incompressible
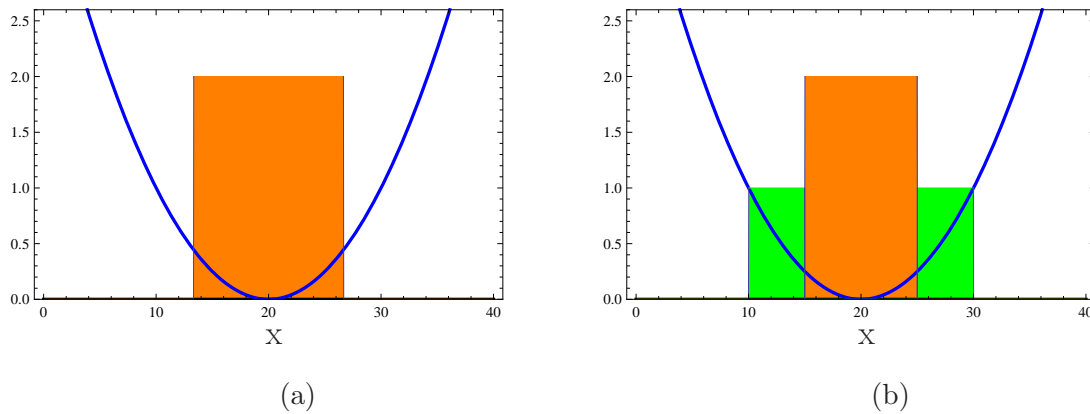
Figure 4.10: Schematic plot for the ground state filling at inactive hopping $t = 0$. Figure (a) shows the situation for $U < 0$ and (b) $U > 0$. The blue curve indicates the trapping potential in arbitrary units. The orange region is doubly and the green region is singly occupied. While at repulsive interaction a singly occupied region occurs, it is missing for attractive interaction.

Mott-plateau has been experimentally confirmed in Ref. [30], showing excellent agreement with theory. Note that the Mott-plateau may be magnetized, but this is not necessarily the case, and it is indeed not the case in the calculations and experiments performed in Refs. [28, 30]. In the weak interaction regime $U < U_C$, where our calculations are performed, there is no hint for a broadening of the half-filled region in a paramagnetic phase (see Figure (4.9)).

Of course, an additional feature which may be used as hint for antiferromagnetism, is the experimental determination of the DOS, which is, e.g., accessible via RF-spectroscopy. A local minimum below and its absence beyond the Néel temperature would indicate an antiferromagnetic transition. The DOS has the same symmetry as the Hamiltonian [SU(2) for $\Delta\mu = 0$ and U(1) for $\Delta\mu \neq 0$] and, therefore, it does also not depend on the random effect of spontaneous symmetry breaking.

4.6 Comparison to the attractive U-model

The following remark concerns again the connection between the antiferromagnetic and the superfluid trapped systems. As we have emphasized in section 4.1, a special particle-hole transformation connects the positive-U and the negative-U model. Nevertheless, the trapped models are not equivalent. Transforming one model into the other changes the character of the trapping potential V to an **i**-dependent Zeeman term. Note that this is not the case for translationally invariant systems.

The first point we want to address here is the broadening of the region of half filling at ultralow temperatures. This feature obviously occurs for $U > 0$, and it is absent for $U < 0$. For both signs of U in a translationally invariant system the gap size, the order parameter, and the transition temperature are maximal at half filling. Also, the gain of grand potential is maximal there. Heuristically, one would expect, for $U > 0$ and $U < 0$, that this region is broadened in a balanced system. In a spatial region where the chemical potential does not differ much from the one favoring half filling [$\mu - V(\mathbf{i}) \approx U/2$ in an LDA argument], one would expect an energy gain due to pairing/antiferromagnetic ordering and a slight loss of energy due to the particle density being half, with a chemical potential which is not exactly

corresponding to half filling. One could argue that, if

$$|E_{\text{gap}}| > \left| \mu(\mathbf{i}) - \frac{U}{2} \right| \, , \tag{4.10}$$

half filling is favored for both signs of U. In order to show why this is not the case, note Figure (4.10). In order to show the effect, which distinguishes both signs of the interaction, we show exact solutions for the fillings of systems with a zero hopping-amplitude ($t = 0$). Since, in this case, hopping is not allowed, each lattice-site may be treated independently, and it is a simple exercise to calculate the ground state of such a system. The on-site Hamiltonian for the balanced case is simply given as:

$$\mathcal{H}_{\mathbf{i}} = - \sum_{\sigma} \mu(\mathbf{i}) \, \hat{n}_{\mathbf{i}\sigma} + U \hat{n}_{\mathbf{i}\uparrow} \hat{n}_{\mathbf{i}\downarrow} \, . \tag{4.11}$$

First we treat the case of the attractive interaction. The occupation numbers in the ground state are given as:

$$n = \begin{cases} 2 & \text{if} \quad \mu > \frac{U}{2} \\ \\ 0 & \text{if} \quad \mu < \frac{U}{2} \end{cases} \, . \tag{4.12}$$

For $U > 0$ the situation is as follows:

$$n = \begin{cases} 2 & \text{if} \quad \mu > \frac{U}{2} \\ \\ 1 & \text{if} \quad \frac{U}{2} > \mu > 0 \\ \\ 0 & \text{if} \quad \mu < 0 \end{cases} \, . \tag{4.13}$$

This fact obviously leads to a qualitatively different behavior of trapped fermions, depending on the sign of the interaction strength. While in the attractive case half filling in the ground-state is only allowed for the degenerate case $\mu(\mathbf{i}) = U/2$, in the repulsive case a half-filled plateau may occur. If one replaces the full Hamiltonian in Equation (4.11) by the Hartree-Fock version, interestingly there is no difference for the occupation numbers in the attractive U-case. For repulsive interaction strengths the region $0 < \mu(\mathbf{i}) < U/2$ is smeared out and the change of the filling in dependence of $\mu(\mathbf{i})$ from 0 to 2 becomes smooth.

For weak tunneling strengths t one can perform perturbation theory in t, for both interaction strengths the perturbation expansion may be derived from Ref. [90]. The first order term

$$\mathcal{H}_1 = -t \sum_{(\mathbf{ij})\sigma} \hat{n}_{\mathbf{i}-\sigma} \left(1 - \hat{n}_{\mathbf{j}-\sigma} \right) \hat{c}^\dagger_{\mathbf{i}\sigma} \hat{c}_{\mathbf{j}\sigma} \tag{4.14}$$

does not lead to any contribution for $U < 0$, since a single displacement of an atom automatically leads to a change of the number of doubly occupied sites. For $U > 0$ one may assume the contribution of (4.14) to be weak or negligible if one assumes that the chemical potential difference at the domain-walls between differently filled regions is much larger than t. Hence, in further arguments we neglect (4.14).

The second order term for $U > 0$ behaves completely differently than for $U < 0$. For attractive interaction strengths the hopping-term of the Hamiltonian is mapped on a hard-core boson model with a hopping amplitude t_B and a repulsive nearest neighbor interaction

$$\mathcal{H}_{2,U<0} = \frac{2t^2}{|U|} \sum_{(\mathbf{ij})} \left(\tilde{n}_{\mathbf{i}} \tilde{n}_{\mathbf{j}} - \hat{b}^\dagger_{\mathbf{i}} \hat{b}_{\mathbf{j}} \right) \, , \tag{4.15}$$

where $\hat{b}_{\mathbf{i}}$ and $\tilde{n}_{\mathbf{i}}$ denote hard-core bosonic annihilation/numbering operators. Assuming again that all other model parameters are much larger than t, the second-order contribution may be neglected for $U < 0$. Hence, a weak hopping amplitude marginally changes the ground state of our model.

The situation is completely different when dealing with a repulsive interaction strength. If one assumes again that t is much smaller than the rest of the sizes, an antiferromagnetic coupling of the Heisenberg-type,

$$\mathcal{H}_{2,U>0} = \frac{2t^2}{|U|} \sum_{(\mathbf{ij}:\ \mathrm{h.f.})} \hat{\mathbf{S}}_{\mathbf{i}} \cdot \hat{\mathbf{S}}_{\mathbf{j}} , \qquad (4.16)$$

remains for the half-filled spatial region. Since in 0th order in t the model is completely degenerate [SU(2)-symmetric] for different spin-configurations in the half-filled region, the contribution of (4.16) is relevant, regardless of how small t is in contrast to other energy scales in the system. This mechanism leads to antiferromagnetism in the strong coupling limit for $U > 0$.

From this point of view we have learned the following for the trapped two-component Fermi-mixtures in the ground state:

- Broadening of the half-filled region is absent of an attractive interaction strength.

- Broadening of the half-filled region is a typical feature for a repulsive interaction strength. At strong coupling the half-filled plateau is a Mott-insulator, which may have antiferromagnetic order caused by a Heisenberg-coupling $2t^2/U$. At weak coupling, this effect arises only if the system has a broken symmetry. The plateau is antiferromagnetic, but not Mott-insulating.

- The occurrence or absence of a half-filled plateau are generic properties for the model and are independent from $|U|/t$. Indeed, previous literature [22] predicts a smooth crossover between weak and strong interaction strengths in the phase with broken-symmetry, at least in translationally invariant lattice systems.

4.7 Incommensurate antiferromagnetic states

Special incommensurate antiferromagnetic states may be created by particle-hole transforming a vortex-state of the attractive model onto the repulsive one. In the literature, vortex-excitations of an xy-antiferromagnet are known as merons and are extensively discussed in Ref. [50]. Hence, we will only briefly present such a state and refer to the existing literature. As a result we present one typical meron-state obtained with our program in Figure (4.11), which is, at least, a numerically stable solution. Of course, such a state does not minimize the grand-potential. This fact becomes obvious by comparing the DOSs of the meron state and the competing x-antiferromagnet shown in Figure (4.11)(b). Note that the x- and y- components of the magnetization [Figure (4.11)(a)] do not show the typical symmetry properties discussed above for commensurate states.

More sophisticated incommensurate states are discussed in Ref. [51] at strong coupling. The authors perform, analogously to our work, unrestricted Hartree-Fock calculations. At weak coupling, the results, obtained in [51], are in good agreement with our work. At first sight the results at strong coupling seem to be in contrast to our findings, since they obtain incommensurate states at thermal equilibrium. This statement would disagree with our analytical findings presented in section 1.4.6, namely that there is a uniquely defined vector to

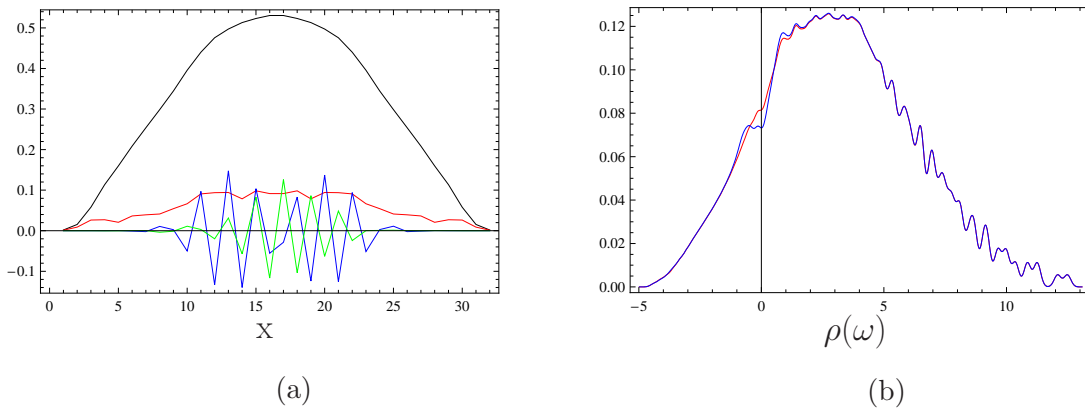(a)   (b)

Figure 4.11: In (a), the total particle density (black), the z-component (red), the x-component (blue), and the y-component (green) of the magnetization in a meron state are shown. In (b), the DOSs of the meron state (red) and of the thermodynamically stable x-antiferromagnet (blue) are shown. The parameters are $U = 2.4$, $V = 0.025$, $\mu = 1.5$, $\Delta\mu = 0.4$, and $\beta = 1000$ in units of t. The size of the square lattice is 32×32, and the vortex-number of the meron state is $m = 1$.

whom the antiferromagnetic order is aligned parallelly. At this point it is useful to reemphasize first that the results found in 1.4.6 have been derived by assuming a weak interaction strength. On this basis a term could be neglected. This assumption fails if one assumes strong interaction. Secondly, the authors of [51] use the saddle-point approximation. At strong coupling away from half filling, ferromagnetism may occur in translationally invariant systems [91]. However, the Hartree-Fock approximation is derived exclusively for weak interaction strengths. Whether this approximation describes trapped systems quantitatively and qualitatively correctly at strong coupling is questionable and unanswered until now.

4.8   Spin-dependent hopping

An additional symmetry which may be broken (analogously to superfluid systems) is the symmetry in the hopping term. In the Hamiltonian, this requires a replacement of the type

$$\mathcal{H}_t = -t \sum_{\langle \mathbf{ij} \rangle \, \sigma} \hat{c}^\dagger_{\mathbf{i}\sigma} \hat{c}_{\mathbf{j}\sigma} \rightarrow - \sum_{\langle \mathbf{ij} \rangle \, \sigma} t_\sigma \, \hat{c}^\dagger_{\mathbf{i}\sigma} \hat{c}_{\mathbf{j}\sigma} \ . \tag{4.17}$$

This asymmetry in the hopping-amplitudes breaks the rotational SU(2)-symmetry and reduces it to U(1). Nevertheless, in contrast to a Zeeman term proportional to $\Delta\mu \, (\hat{n}_{\mathbf{i}\uparrow} - \hat{n}_{\mathbf{i}\downarrow})$, the preferred antiferromagnetic order is parallel to the z-axis. This becomes immediately obvious if one performs strong coupling perturbation theory in a half-filled translationally invariant system. The model is mapped on a H_{XXZ} model instead of a Heisenberg model, as follows:

$$\mathcal{H} \rightarrow \frac{2t_\uparrow t_\downarrow}{U} \sum_{\langle \mathbf{ij} \rangle} \hat{\mathbf{S}}_\mathbf{i} \cdot \hat{\mathbf{S}}_\mathbf{j} + \frac{(t_\uparrow - t_\downarrow)^2}{U} \sum_{\langle \mathbf{ij} \rangle} \hat{S}_{\mathbf{i}3} \hat{S}_{\mathbf{j}3} \ . \tag{4.18}$$

Hence, this model is anisotropic and belongs to the Ising symmetry class. The system breaks the $\mathbb{Z}_2$-symmetry rather than the rotation around the z-axis. The mechanism presented above is suggested, e.g., in Ref. [49] to be used to stabilize the z-antiferromagnetic phase. Note, however, that the behavior of a model with reduced symmetry may be completely different with respect to the occurrence of possible phase transitions. E.g., in translationally

invariant lattices with infinite extension in two dimensions, the Ising model has a finite Curie-temperature, while for the Heisenberg model off-diagonal long-range order is forbidden due to the Mermin-Wagner theorem [92].

The point emphasized in this section is the competition of z- and in-plane antiferromagnetism. For a balanced system it is obvious from the arguments presented above that an antiferromagnetic order parameter at thermal equilibrium is parallel to the quantization axis. An imbalance in the chemical potential ($\Delta\mu \neq 0$) favors an xy-antiferromagnet, as we have shown above. Hence, if we keep all the other parameters fixed, and vary $\Delta\mu$ from 0 to higher or lower values, we expect a phase transition from a z- to an in-plane antiferromagnet. Note that, if hopping is spin-dependent, the situations for positive and negative $\Delta\mu$ are not equivalent, as it is the case for symmetric hopping amplitudes t_σ. The mapping $\Delta\mu \to -\Delta\mu$ does not simply lead to an exchange of the type $\sigma \to -\sigma$. Choosing $\Delta\mu = 0$ does not necessarily lead to balanced occupation numbers for both spin-species. The phase transitions occurring are expected to be first order transitions, since in second order transitions order parameters are usually a steady function of the parameter varied. Here, we expect jumps from parameters being 0 to finite values and vice versa.

Results for a spin-dependent hopping amplitude are presented in Figures (4.12) and (4.13). In contrast to previous sections, we present only the physical antiferromagnetic solution. In Figure (4.12)(a), the imbalance in the chemical potential is turned off ($\Delta\mu = 0$). As argued above, the total number of "↓" spins is higher than the number of "↑" spins. Here, the thermodynamically stable solution is indeed the z-antiferromagnet. Since we are in the low-temperature limit, the typical broadening of the half-filled region still occurs. In Figure (4.12)(b), we choose $\Delta\mu = -0.1$. This stabilizes the x-antiferromagnet. The resulting total particle numbers are still $N_\downarrow > N_\uparrow$, of course. In Figure (4.13)(a), we choose $\Delta\mu = 0.1$. Here, the "↑"-spins represent the majority species. As one can see, there is no direct mapping on the opposite sign of $\Delta\mu$. The system is again an x-antiferromagnet. In Figure (4.13)(b), the DOSs of the three parameter settings are presented. They are hardly distinguishable quantitatively. They possess the same qualitative features in the vicinity of the Fermi edge.

One point emphasized at symmetric hopping was the role of the symmetries of the different parameters as a function of **i**. At symmetric hopping, quantities breaking spontaneously a symmetry had an odd symmetry in real-space, while the other quantities had an even one. This feature is not valid for $t_\uparrow \neq t_\downarrow$. The z-antiferromagnet occurring at small $|\Delta\mu|$ has

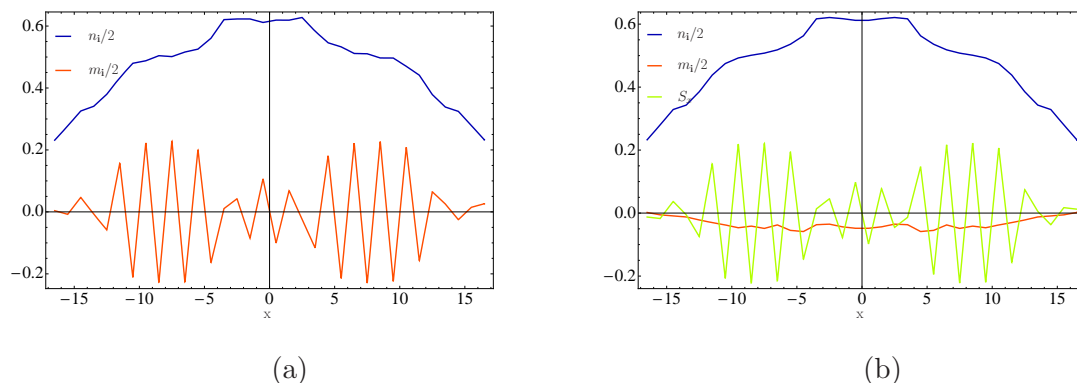(a)   (b)

Figure 4.12: Thermodynamically stable solutions for systems on a 34×34 square latice. The parameters are $U = 2.4$, $V = 0.01$, $\mu = 2.0$, $\beta = 100$, $t_\uparrow = 0.9$, and (a) $\Delta\mu = 0.0$ (b) $\Delta\mu = -0.1$ in units of $t_\downarrow$. In (a), the system is a z-antiferromagnet, while in (b) it is a x-antiferromagnet.
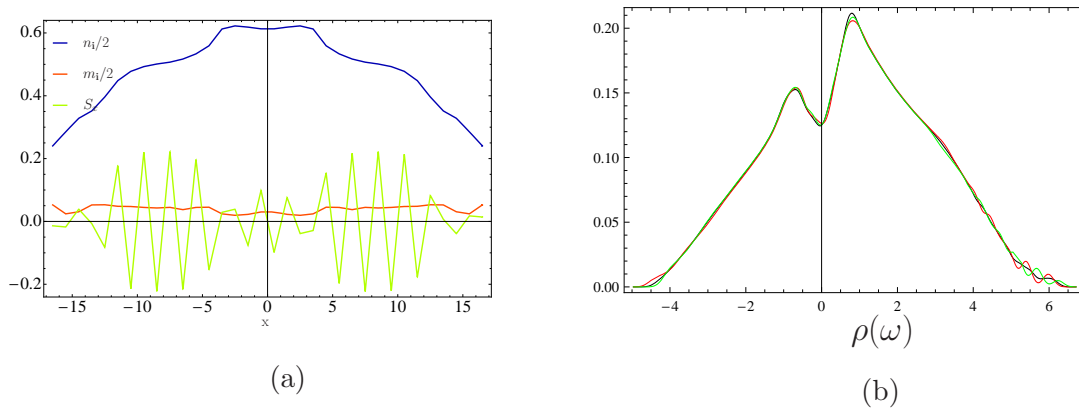
(a)

(b)

Figure 4.13: In (a), a thermodynamically stable x-antiferromagnet with the same parameters as in Figure (4.12) besides $\Delta\mu = +0.2$ is shown. In (b), the corresponding DOSs for the systems in (4.12) and (a) are presented, where the black/red/green curve corresponds to $\Delta\mu = 0 / 0.2 / -0.2$.

no symmetry in any quantity. The x-antiferromagnets arising from $\Delta\mu \neq 0$ have an even symmetry for the total particle density and the z-component of the magnetization, while the x-component of the magnetization does not have any symmetry under mirroring.

In this section, we presented exclusively results for a small hopping asymmetry $t_\uparrow/t_\downarrow = 0.9$. The effects arising here are qualitatively the same as for stronger imbalances in the hopping strength. As emphasized for spin-depending hopping in the attractive-U case in section 3.6, the Hartree-Fock approximation is not useful for describing very strong hopping asymmetries. For completeness, we present results for the most extreme hopping asymmetry in the following. Note that if one species is immobile, Hartree-Fock may predict xy-antiferromagnetism, which is absolutely unphysical in this case [see, e.g, Equation (4.18)].

If one turns off the hopping for one spin-species, one ends up with the Falicov-Kimball model [93], in which the "↓"-species is mobile and the "↑"-species is spatially fixed in the sense of an annealed disorder. The Falicov-Kimball model is frequently used as a simplification of the Hubbard model, since it is easier to handle, analytically and numerically. The translationally invariant repulsive-U Falicov-Kimball model does not have an xy-antiferromagnetic phase, since one spin-species is immobile. Z-antiferromagnets may occur at thermal equilibrium, of course. An extensive treatment of the trapped Falicov-Kimball model fitted for ultracold gases with QMC-methods is found, e.g., in Ref. [38]. We briefly summarize the authors' results and present the occurring phases in Figure (4.14). It turns out that, depending on the trapping potential and the temperature at low interaction strength, a normal phase or z-antiferromagnet may be thermodynamically stable, while at strong interactions strengths a normal phase, a "labyrinth"-phase or phase separation may occur. Especially the effects at strong interaction strengths are highly non-perturbative and, therefore, not accessible in a diagrammatic approach. An accurate investigation of our model at a finite interaction strength would be of great interest. Unfortunately, the fermionic sign problem prevents an investigation of x-antiferromagnets in most QMC-methods. Hence, an accurate method describing such a system is still a challenge for the near future.
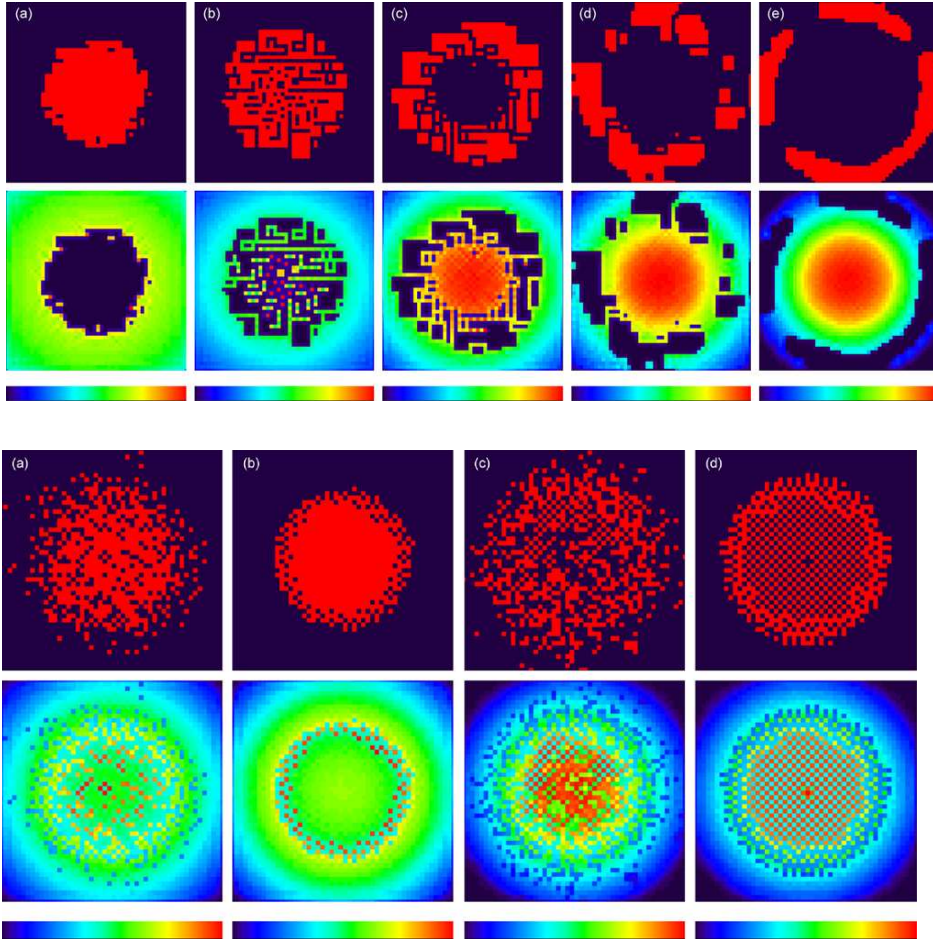
Figure 4.14: Representative QMC snapshots of real-space configurations of a trapped Falicov-Kimball model taken from Ref. [38]. The upper panel displays a labyrinth-phase and phase separation at $U = 5t_\downarrow$, while the lower panel displays z-antiferromagnetism at $U = t_\downarrow$. In the respective panels the upper (lower) image shows the distribution of the "↑"- ("↓"-)particles. The plots show systems with different values of the trapping potential strangth and different temperatures. In the upper panel, the temperature is fixed as $\beta = 100$, and the trapping potential increases from left to right.

4.9 Local density approximation

In the last section of this chapter, we briefly show why the LDA fails to describe qualitatively a trapped antiferromagnet. As we have seen in chapter 2, the saddle-point results undergo first order phase transitions when varying system parameters like μ and $\Delta\mu$ in translationally invariant systems. As a consequence, including the results of chapter 2 in the LDA would predict sharp boundaries in real-space, where different phases occur. On the basis of our results presented above in this chapter, this is not the case for superfluid and antiferromagnetic systems.

An example proving that the LDA predictions fail in predicting the correct occupation numbers beyond Hartree-Fock is shown in Figure (4.15). Here, a numerical comparison of LDA+DMFT with R-DMFT is presented for a balanced system. As one can see, the
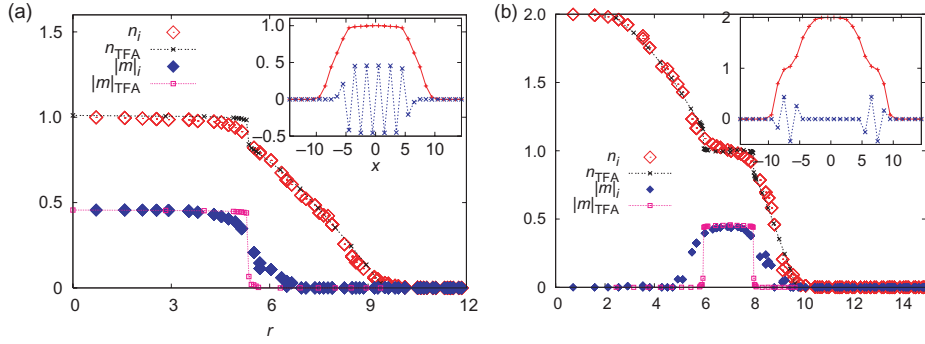
Figure 4.15: LDA(here it is called TFA)+DMFT results versus R-DMFT results for the total particle density and the local magnetization on a 30×30 square lattice. The results are taken from Ref. [46]. The system parameters are chosen to be $U = 10$ and (a) $V = 0.1$ and $\mu = 5$, (b) $V = 0.2$, $\mu = 15$ and $\Delta\mu = 0$ in units of t.

LDA especially fails in the border region where filling changes from half filling to lower or higher values. While the LDA predicts a sharp half-filled plateau in Figure (4.15), a more shoulder-like behavior appears. This shoulder-like behavior predicted by DMFT is also in good agreement with our results obtained within the saddle-point approximation presented above.

Analogously to the attractive-U model, a drastical failure of the LDA is expected at spin-dependent hopping. There is also no literature available on that topic. Nevertheless, a review of the results for translationally invariant systems presented in chapter 2 reveals that the LDA may predict spatial regions with a xy-antiferromagnet as well as regions with a z-antiferromagnet for one and the same system. As shown in our results with exact treatment of the harmonic confinement, either an x- or a z-antiferromagnet occurs globally, depending on $\Delta\mu$. A LDA-result would also violate our statements made in section 1.4.6. This is again a good example why the LDA predicts unphysical results in states with a spontaneously broken symmetry.

Chapter 5

Second Order Perturbation Theory

Finally, one question left open in the previous chapters is the role the fluctuations neglected in the interaction term. For the purpose of treating the fluctuations we perform a self-consistent perturbation expansion up to second order for the self-energy in this chapter. We present the analytical structure of the formalism used, and we explain how we evaluate it numerically. Since the diagrammatic second order formalism can also be used to reproduce - in part - the first order results of the previous chapters we compare the methods with each other. Finally, we present the numerical results of the second order code and show the influence of the fluctuations on translationally invariant and on trapped systems for repulsive interaction strengths. The underlying Hamiltonian has the form of Eq. (1.15). Although the approach presented in this chapter is able to describe both z- and x-antiferromagnets we restrict consideration to balanced systems and, therefore, we treat the numerically more simple z-antiferromagnets.

The results of this chapter were obtained in cooperation with A. Pfister and E. Jakobi. E. Jakobi provided the program for performing second order perturbation theory and A. Pfister adapted this code to the treatment of trapped Fermi gases. The present author's contributions to this collaboration were providing a saddle-point code in order to have a fast access to the relevant parameter regions and the physically correct phases occurring, as well as innumerable discussions on how to adapt E. Jakobi's code to the given physical problem.

5.1 Second order diagrammatic expansion for the self-energy

The analytical approach used in this chapter is a standard weak-coupling expansion in the self-energy using Feynman-diagrams [78]. In this approach we start from the interaction-free case and introduce small interaction U, where U must be small in comparison with the half bandwidth ($U/W < 1$, in our case: two dimensions, nearest neighbor-hopping and square lattice $W = 4t$). In this diagrammatic formalism the interaction vertices are represented as in Figure (5.1). Here, the index pairs $i\sigma$ denote real-space and spin positions. Since the interaction is purely local in our Hamiltonian, there will be only diagrams contributing if the spatial indices are equal $i = j = k = l$.

The general central issue of a weak coupling approach is the determination of the full Green function $G_{ij\sigma\sigma'}(\omega)$. The full Green function in matrix-form is given via the Dyson equation:

$$\mathcal{G}(\omega) = \left[\mathcal{G}_0^{-1}(\omega) - \Sigma(\omega)\right]^{-1} , \qquad (5.1)$$

where the matrices have the size of $2\mathcal{N} \times 2\mathcal{N}$. $\mathcal{G}(\omega)$ denotes the full Green function, $\mathcal{G}_0(\omega)$ the interaction-free Green function and $\Sigma(\omega)$ is the self-energy. The interaction-free Green
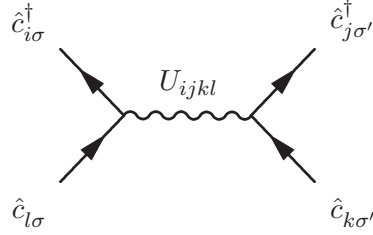
Figure 5.1: Interaction vertex for a weak coupling perturbation theory. The letters indicate the position, while $\sigma^{(\prime)}$ indicates the spin index.

function is simply defined as

$$\mathcal{G}_0(\omega) \equiv [\omega \mathbb{1} - \mathcal{H}_0]^{-1} \ , \tag{5.2}$$

where $\mathcal{H}_0$ is the interaction-free Hamiltonian. In our approach we use real frequencies ω instead of the often used Matsubara-frequencies. The disadvantage in this method lies in a more complicated evaluation of the Feynman-diagrams, i.e., one has to evaluate integrals in the real-time formalism where the evaluation of a product is sufficient in the imaginary-time formalism. Nevertheless, an analytic continuation, which is an ill-conditioned problem and which is needed for obtaining DOSs in the imaginary-time formalism, is not necessary in the real-time formalism. In our approach it is necessary to obtain the quantities of Equation (5.1) self-consistently within second order perturbation theory. In this sense we perform a conserving real-space Baym-Kadanoff approximation [94]. Since $\mathcal{G}_0^{-1}(\omega)$ is irrevertible at the discrete eigenvalues of the underlying Hamiltonian, it is necessary to add a tiny imaginary part to the frequency ω

$$\omega \rightarrow \omega + i\delta \ . \tag{5.3}$$

The quantity δ has to be chosen sufficiently large so that the spectral functions

$$\rho_{ij\sigma\sigma'}(\omega) \equiv \frac{1}{\pi}\mathfrak{Im}\left[\mathcal{G}_{ij\sigma\sigma'}(\omega)\right] \tag{5.4}$$

do not suffer from too narrow peaks. Otherwise the sampling of $\rho_{ij}(\omega)$ would increase drastically in numerical effort. On the other hand, adding too large an imaginary part $i\delta$ leads to states which differ strongly from the Hartree-Fock solutions, in the sense that at first order level the order parameter is much smaller than in exact Hartree-Fock. The artificial broadening of the DOS acts similarly to an increase of temperature. Hence, one has to be careful with the choice of δ.

In order to perform second order perturbation theory one has to include the diagrams presented in Figure (5.2). Here, (a) represents the Hartree term which can be described as the interaction of a particle with spin σ with the average density of a particle with opposite spin $-\sigma$ on the same lattice site. The Hartree term does nothing else than shifting the local chemical potential for the opposite spin-species. Its effects are the effective deformation of the trapping potential and, if one assumes asymmetric starting conditions for the Green function, it stabilizes the z-antiferromagnet. Diagram (b), the Fock term, is only present if the on-site Green function is non-diagonal in spin-space. This is the case if a x-antiferromagnet is analyzed. This fact follows directly from the way the Green function connects opposite spins in the interaction vertex. Finally, diagrams (c) and (d) are the second order contributions. Also for the second order diagrams one has to distinguish between states with diagonal and non-diagonal Green functions in spin space. In the diagonal case, diagram (d) does not contribute at all and diagram (c) yields only one half of the non-vanishing contributions in the non-diagonal case. Nevertheless, both second order diagrams generally lead to an ω-dependent contribution to the self-energy. The four relevant diagrams may be evaluated as
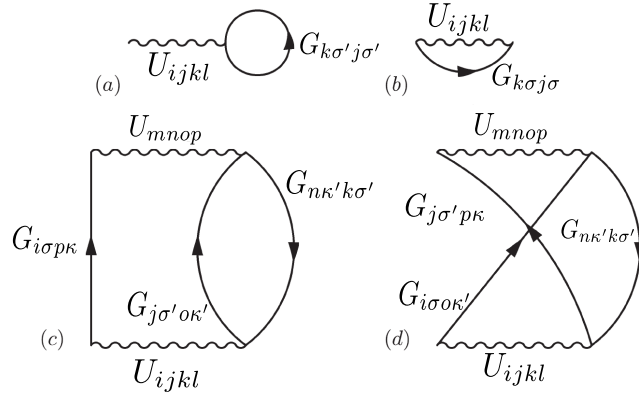
Figure 5.2: Self-energy diagrams up two second order. The diagrams (a) and (b) are the first order diagrams, (a) is the Hartree- and (b) is the Fock diagram. The diagrams (b) an (d) vanish always if the Green functions are diagonal in spin-space.

follows (a rigorous derivation of Equations (5.5)-(5.8) can be found in [95], the formulae are presented in the same order as the corresponding diagrams in Figure (5.2))

$$\Sigma_{1,\mathrm{H}} = U\,\delta_{ij}\delta_{\sigma\sigma'}\int d\omega\,\rho_{ii\bar{\sigma}\bar{\sigma}}(\omega)f_\beta(\omega) = U\,\delta_{ij}\delta_{\sigma\sigma'}\langle n_{i\bar{\sigma}}\rangle\,, \tag{5.5}$$

$$\Sigma_{1,\mathrm{F}} = U\,\delta_{ij}\delta_{\bar{\sigma}\sigma'}\int d\omega\,\rho_{ii\sigma\bar{\sigma}}(\omega)f_\beta(\omega) = U\,\delta_{ij}\delta_{\bar{\sigma}\sigma'}\langle S_{i+}\rangle = U\,\delta_{ij}\delta_{\bar{\sigma}\sigma'}\langle S_{i-}\rangle\,, \tag{5.6}$$

$$\Sigma_{2,\mathrm{NC}}(\omega) = U^2\int d\boldsymbol{\omega}\,\frac{\rho_{ij\sigma\sigma'}(\omega_1)\,\rho_{ji\bar{\sigma}'\bar{\sigma}}(\omega_2)\,\rho_{ij\bar{\sigma}\bar{\sigma}'}(\omega_3)}{\omega-\omega_1+\omega_2-\omega_3+i\delta}\times \tag{5.7}$$
$$\times\;[f_\beta(\omega_1)\,f_\beta(-\omega_2)\,f_\beta(\omega_3)+f_\beta(-\omega_1)\,f_\beta(\omega_2)\,f_\beta(-\omega_3)]\,,$$

$$\Sigma_{2,\mathrm{C}}(\omega) = -U^2\int d\boldsymbol{\omega}\,\frac{\rho_{ij\sigma\bar{\sigma}'}(\omega_1)\,\rho_{ji\bar{\sigma}'\bar{\sigma}}(\omega_2)\,\rho_{ij\bar{\sigma}\sigma'}(\omega_3)}{\omega-\omega_1+\omega_2-\omega_3+i\delta}\times \tag{5.8}$$
$$\times\;[f_\beta(\omega_1)\,f_\beta(-\omega_2)\,f_\beta(\omega_3)+f_\beta(-\omega_1)\,f_\beta(\omega_2)\,f_\beta(-\omega_3)]\,,$$

where the labels "NC" [corresponding to diagram (5.2)(c)] and "C" [corresponding to diagram (5.2)(d)] mean crossing and non-crossing Green functions, respectively. Note that, while the second order contributions are frequency dependent, the first order contributions are not. In our formulation the Hartree and the Fock terms are real quantities. While for the Hartree terms this is always the case (they lie on the diagonal part of $\mathcal{H}_0$), for the Fock terms this means that antiferromagnetism is restricted to the x-component, so that the description of a more complicated xy-antiferromagnet is not possible in this formulation, since a non-vanishing magnetization in the y-direction implies (matrix notation)

$$\left[\mathcal{G}^R(\omega)\right]^T \neq \mathcal{G}^R(\omega) \Rightarrow \rho(\omega) \to \frac{1}{2\pi i}\left[\mathcal{G}^R(\omega)-\mathcal{G}^A(\omega)\right] \notin \mathbb{R}, \tag{5.9}$$

which is not a designated situation to be treated within our code. In Eq. (5.9) we distinguish between the retarded and the advanced Green function, where in the rest of this chapter we always mean the retarded version when omitting the index A/R. However, as we have seen in the previous chapter, this is not a limitation in practice, since physical states have globally defined direction for the antiferromagnetic order parameter and a simple global rotation may be used to eliminate the y-component of the magnetization. The second order terms destroy the property of $\mathcal{G}^{-1}(\omega)$ of being a sparse matrix. A typical on-site self-energy is presented in
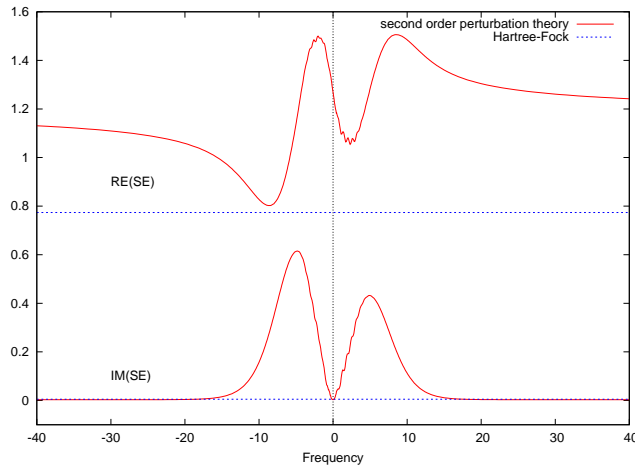
Figure 5.3: Real- and imaginary part of a typical on-site spin-diagonal self-energy in first and second order. While in first order the imaginary part vanishes, the second order diagram creates a frequency-dependent function.

Figure (5.3). From this figure it becomes obvious, that one has to choose δ in (5.3) sufficiently small, so that

$$\delta \ll \min_{\{i\sigma\}}\mathfrak{Im}[\Sigma_{ii\sigma\sigma}(0)] \ , \tag{5.10}$$

in order to obtain the correct reduction of order parameters/Néel temperatures as a consequence of the physical self-energy and not as a consequence of the artificial parameter δ.

The evaluation of the Dyson equation (5.1) and the self-energies (5.5)-(5.8) form a self-consistency cycle when starting iterations with $\mathcal{G}_0(\omega)$ and then inserting the full Green function $\mathcal{G}(\omega)$ into Eqs. (5.5)-(5.8). As abort criterion we have chosen the similarity between two Green functions in two consecutive steps

$$\int d\omega \, |\mathcal{G}_{n-1}(\omega) - \mathcal{G}_n(\omega)| < \epsilon \ , \tag{5.11}$$

with an adequate value of ϵ found empirically. For numerical purposes we relax the self-energy

$$\Sigma_n(\omega) \to \frac{2}{3}\Sigma_n(\omega) + \frac{1}{3}\Sigma_{n-1}(\omega) \tag{5.12}$$

during the iteration steps. With this real-space and real-frequency Baym-Kadanoff formalism one is theoretically able to calculate antiferromagnets and normal states with second order corrections for trapped systems with any shape of the trap as well as systems with periodic boundary conditions. The difference between periodic and static boundary conditions in this formalism lies just in the matrix elements of $\mathcal{H}_0$ as it is the case in chapter 2 in the Hartree-Fock formalism. The matrices $\mathcal{H}_0$ are the same in both formalisms.

5.2 Comparison to ED-Solver

Of course, when performing first order perturbation theory it is of interest how the algorithm used to obtain the results in the previous chapters compares with the algorithm used in this chapter. In first order the self-energy is frequency-independent and purely local. While in the previous chapters we had to diagonalize the Hamilton-matrix once per iteration step, in
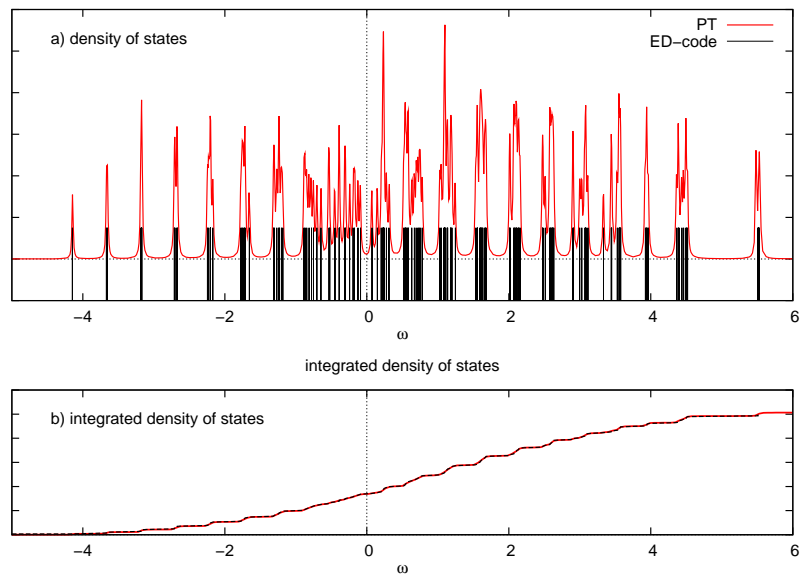
Figure 5.4: Discrete spectrum from ED-code (black) versus continuous spectrum in first order perturbation theory (red) presented in (a). The peaks of the continuous spectrum lie exactly on the discrete values. The integrated spectra (b) are identical within the linewidth.

this formalism we have to sample the inversion presented in the Dyson equation (5.1) over the relevant ω-values. The first difference is, of course, the numerical effort. It is much more efficient to perform the diagonalization once than to sample the matrix inversions. E.g., the time needed to perform calculations on a 42×42 lattice with the ED-code[1] compares approximatively with the time needed to perform calculations on a 12×12 lattice with the perturbation theory code. Furthermore, the ED-code is exact in the sense that it makes no use of the parameter δ. Since the Hamilton-matrix is diagonalized directly, one obtains the discrete eigenvalues instead of a smeared out spectrum. In the previous chapters, we have artificially smeared out the eigenvalues just for the purpose of visualization. A choice of a too large value of δ drastically reduces the size of order parameters in comparison to the ED-code. Nevertheless, in the perturbation theory code, at least at first order level one has to choose $\delta > 0$ in order to obtain the retarded Green function correctly. As becomes clear from Figure (5.4), an accurate choice of $\delta \propto 10^{-4}$ provides a good agreement between the first order code and the ED-code in this parameter region. Also the order parameters are in good agreement with ED as demonstrated in Figure (5.4). Note that the minimum of the DOS, which was classified as typical feature of an antiferromagnetic system, is hardly visible at the small system sizes accessible in the perturbation theory code, but it is still present. Nevertheless, the good agreement between both programs represents an outstanding validation for both codes, since they were developed independently with different methods.

The advantage of the perturbation theory code is the possibility of including second order diagrams, of course. This feature is impossible in the ED-formalism. In first order the self-energy is ω-independent, and, hence, one can view the self energy as a constant shift in the Hamilton-matrix

$$\mathcal{H} = \mathcal{H}_0 + \Sigma_1 \tag{5.13}$$

---

[1]ED-code: "exact diagonalization"-code, program used to obtain the Hartree-Fock results in chapters 2-4, exact in the sense of $\delta = 0$.
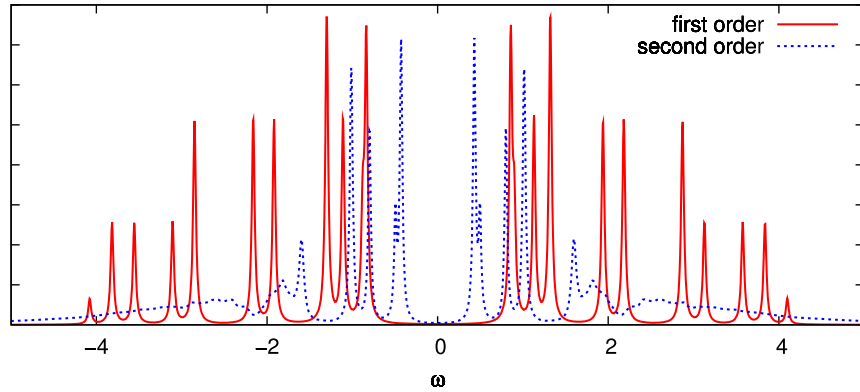
Figure 5.5: Comparison of the DOSs of a half-filled translationally invariant system within first and second order real-space Baym-Kadanoff perturbation theory. The red line represents the first order results while the dotted blue line represents the second order results. It reveals that the second order contribution smears out the spectrum and the size of the gap is reduced to about $\sim 60\%$ of the HF-value.

that can be diagonalized with standard-methods. This point becomes clear if one writes down the eigenvalue condition

$$\det(\mathcal{H} - \omega \mathbb{1}) = \det\left(\mathcal{H}_0 + \Sigma_1 - \omega \mathbb{1}\right) = 0 \ . \tag{5.14}$$

Replacing Σ_1 by $\Sigma(\omega)$ in Eq. (5.14) shows that the character of this equation completely changes and that the problem does not belong to the eigenvalue class. The same form of replacement does not create any problems while sampling a Dyson equation instead.

5.3 Results within second order

It is of interest to compare both translationally invariant and trapped systems. Translationally invariant systems have been studied within second order perturbation theory analytically in the literature [96, 97]. In this section we present the similarities and differences between the asymptotically exact $(U/t \to 0)$ analytical results and our results obtained in finite sized systems. Furthermore, we show how the second order contribution renormalizes the Hartree-Fock results for trapped systems presented in chapter 4.

5.3.1 Translationally invariant systems

In two dimensions antiferromagnetic order arising from a short-ranged interaction is forbidden in the thermodynamical limit due to the Mermin-Wagner theorem [92]. This exact statement can be reproduced when performing self-consistent perturbation theory in the weak-U/t-limit, as it is done, e.g., in Ref. [97]. In two dimensions the perturbation series predicts a breakdown of symmetry breaking at $U \neq 0$ and, therefore, the antiferromagnetic order vanishes in the ground state. In contrast to the two-dimensional situation, in $d = 3$ the order parameter and the Néel temperature are renormalized by a factor of $q \approx 0.28$.

An analogous problem is known from interaction-free BEC in two dimensions [98]. A translationally invariant free system with periodic boundary conditions has a vanishing critical temperature $T_C = 0$ in $d \leq 2$ in the thermodynamical limit, while the critical temperature
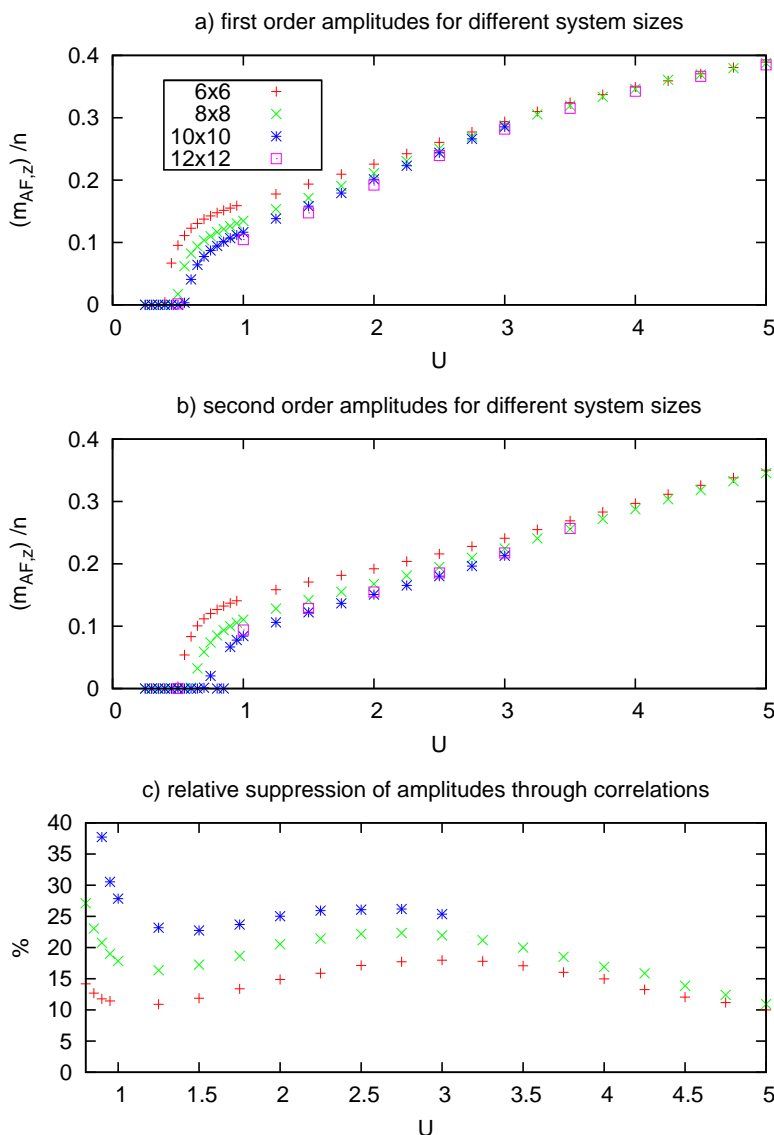
Figure 5.6: First and second order results for different system sizes at $\beta = 50$ for the spin-balanced situation and half filling obtained by A. Pfister. The boundary conditions are periodic. Both the first and second order staggered magnetizations tend to decrease with increasing system size. Note that the relative suppression of the first order results through the second order diagrams should be considered only for $U \geq 1$, since there is quasi no order for too small U-values.

becomes finite in $d \geq 3$. This is an example how thermal fluctuations suppress phase transitions in low dimensional systems[2]. Adding an harmonic potential on the two-dimensional Hamiltonian or assuming discrete eigenvalues for the momentum operator causes the DOS to be discrete and leads to a finite $T_C > 0$, since we are performing a mean-field theory (Strictly

---

[2]In $d = 2$ phase transitions are usually (e.g., if a continuous symmetry is broken) of the Kosterlitz-Thouless type, i.e., below the critical temperature the long-range correlation functions do not converge to a non-zero value. Instead, below T_C the correlation functions decay algebraically, while they decay exponentially above T_C [99].

speaking there is no singularity in the free energy of a finite-sized system and, therefore, there is no phase transition in this sense.). Of course, the symmetry breaking is of a different type for bosons, where the condensation takes place also in the interaction-free case, and fermions, where an interaction is needed to cause antiferromagnetism or superfluidity (depending on the interaction type). From this point of view, it becomes of interest to review the translationally invariant system with periodic boundaries and finite size in second order perturbation theory.

As shown in Figure (5.3) the second order self-energy tends to shift (real part) and to smear out (imaginary part) the spectra. The question we have to answer by numerical calculations is, whether this second order contribution lowers the order parameter and the Néel temperature to a finite value or to zero. Of course, there is no analytical expression available for the self-consistently obtained self-energies.

Results for a typical DOS in first and second order at the same parameters are shown in Figure (5.5). Here, the system is half filled, finite-sized and the boundary conditions are periodic. In fact, the second order contribution does not destroy the antiferromagnetic order entirely. The antiferromagnetic gap is reduced to about 60% of the Hartree-Fock value. The same happens with the order parameter. The sharp-peaked structure of the DOS away from the Fermi edge is drastically smeared out, while in the vicinity of the gap sharp peaks remain and are shifted in the direction of $\omega = 0$. The second order contribution does, of course, not change the symmetry under $\omega \rightarrow -\omega$.

In Figure (5.6) first and second order results are presented for different system sizes. Both the first and second order staggered magnetizations tend to decrease with increasing system size. Of course, in a weak coupling expansion, order parameters increase with increasing interaction strength. Remarkably, the relative suppression of the first order staggered magnetization due to second contributions increases with the system size. Since we cannot provide an analytical expression for the Green function, we have to resort to numerical arguments to explain this fact. Our argument is, that with increasing system size the number of contributions to a fixed on-site self-energy in second order (which includes quantum fluctuations) is augmented by the existence of more lattice sites, while the number of first order contributions (which stabilizes the antiferromagnet) is constant, since the Hartree-diagram is purely local in a Hubbard model. Unfortunately, accessing much bigger systems than 12×12 is numerically very costly.

Another interesting point, visible in Figure (5.6), is the decrease of relative suppression of the order parameter for large values of the interaction. At first sight this might seem to be infeasible, since the first order term increases proportionally to U, while the second order term increases proportionally to U^2. In order to explain this fact, we perform the following gedankenexperiment: Assuming to have reached a perfect Néel state which occurs at Hartree-level in a half-filled system in the ground state at $U/t \rightarrow \infty$, then every site of the system may be described by the pure state

$$|\psi(\mathbf{i})\rangle = \begin{cases} |\uparrow\rangle & \text{if } \mathbf{i} \text{ on the A-sublattice} \\ |\downarrow\rangle & \text{if } \mathbf{i} \text{ on the B-sublattice} \end{cases} . \tag{5.15}$$

This obviously causes the fluctuations to vanish

$$\left\langle \left(\hat{n}_{\mathbf{i}\sigma} - \left\langle \hat{n}_{\mathbf{i}\sigma} \right\rangle \right)^2 \right\rangle = 0 . \tag{5.16}$$

Hence, at Hartree-level, one can exactly replace

$$\hat{n}_{\mathbf{i}\uparrow}\hat{n}_{\mathbf{i}\downarrow} \rightarrow \left\langle \hat{n}_{\mathbf{i}\uparrow} \right\rangle \left\langle \hat{n}_{\mathbf{i}\downarrow} \right\rangle = 0 . \tag{5.17}$$

Consequently, including the second order contribution, which may be seen as the lowest expansion in the fluctuations, does not lead to any contribution in this case. The same is true for higher order diagrams. Of course, these predictions are completely unphysical. The strongly repulsive limit of the Hubbard model at half filling is described by an isotropic Heisenberg model with a coupling constant $J \propto t^2/U$ which becomes arbitrarily small for $U/t \to \infty$. This unphysical prediction is a good reminder of the fact, that a perturbation expansion yields completely unphysical results when used outside its region of validity. One has to be careful with the choice of U/t.

5.3.2 Trapped systems

The challenge of this chapter is, of course, the second order description of trapped systems. This was the reason for performing our diagrammatic expansion in real-space rather than the commonly used **k**-space expansion for translationally invariant systems. We have seen above results for translationally invariant systems and show in the following, how the second order contributions modify the Hartree-Fock results obtained in chapter 4.

The most efficient way to describe the consequences of fluctuations are again the comparison of the DOSs [see Figure (5.7)] and the amplitudes of the staggered order parameter as a function of U and β [see Figures (5.8) and (5.9)] obtained in first and second order.

The DOS of the antiferromagnetic trapped system is, analogously to the untrapped case, smeared out. Note that the peaks at high ω-values correspond to the chemical potential of unoccupied sites far away from the trap center. Of course, these sites are hardly affected by the influence of quantum fluctuations. For trapped systems, as we have seen in chapter 4, there is not a well visible gap in the spectrum. For systems with a larger size ($\gtrsim 30 \times 30$) at least a minimum in the DOS is the vicinity of the Fermi edge appears. However, as we have seen above, this minimum does not appear in small trapped systems, although spontaneous symmetry breaking occurs. Hence, the DOS is of academic interest here, of course, but it is not a good measure for the size of any order parameters neither for their absolute value nor for the relative suppression due to second order contributions.
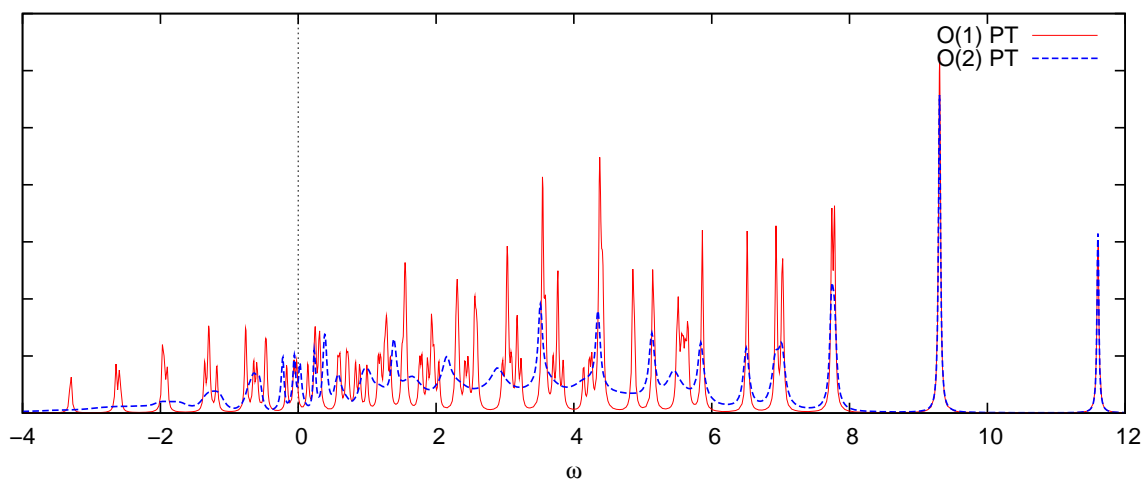

Figure 5.7: Comparison of the DOSs of first order (red) and second order (dotted blue) results for the same system parameters.
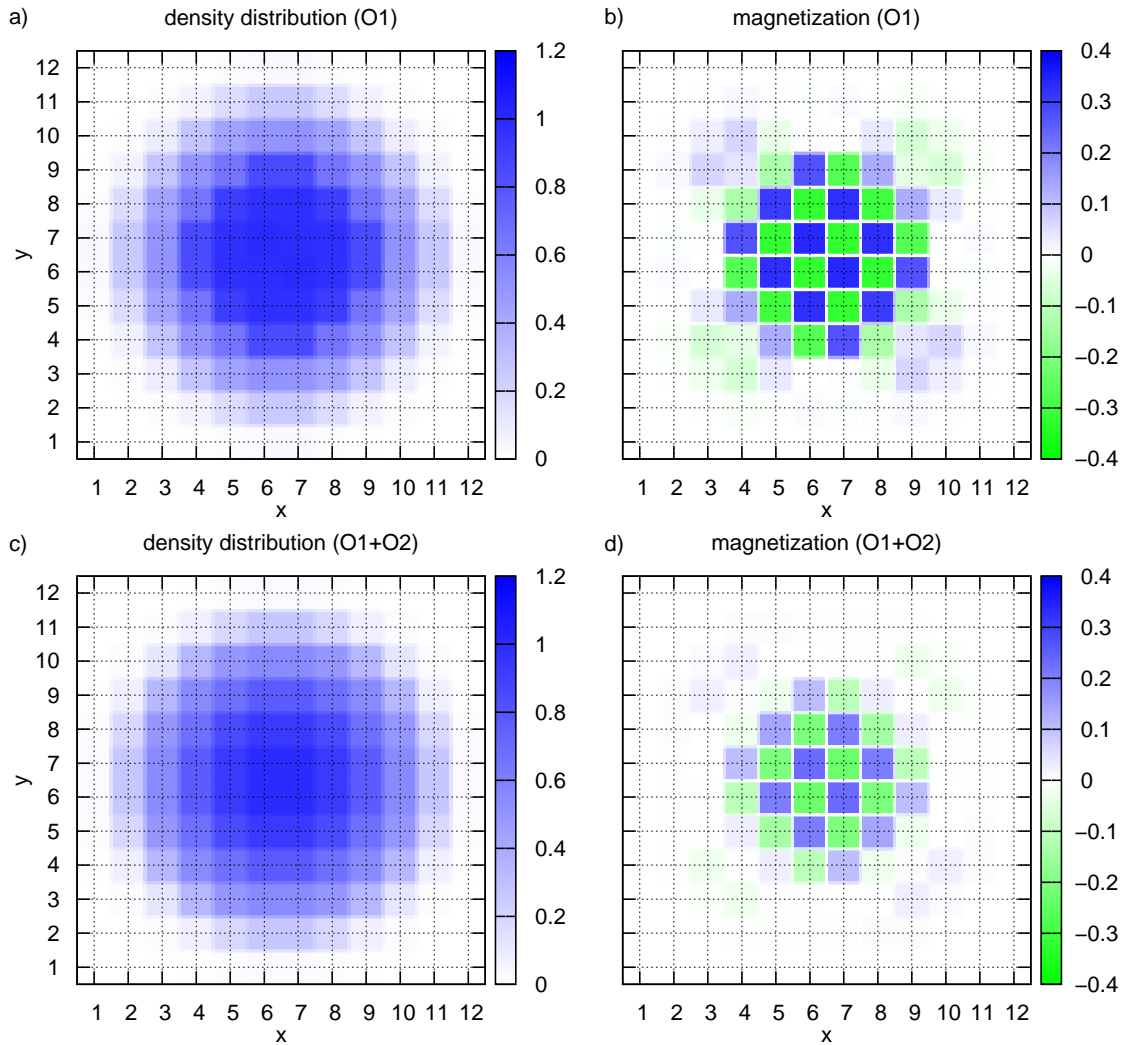
Figure 5.8: Comparison of particle density and staggered magnetization for a system treated in first and second order at the same parameters. Due to the reduction of ordering the half-filled region shrinks to the size of the region with relevant magnetization.

In Figure (5.8) the spatial distribution of the staggered magnetization and the total particle density obtained in first and second order are shown. Analogously to translationally invariant systems the staggered magnetization is reduced in amplitude and, furthermore, in its spatial expansion due to the quantum fluctuations included. In chapter 4 we have shown that antiferromagnetism leads to a broadening of the half-filled region. The reduction of the region with broken symmetry leads also to a shrinking of the half-filled region in size. The shape of the antiferromagnetic and the half-filled area coincide in both first and second order results. Unfortunately, the restriction to small system sizes in the perturbation theory code does not allow us to see the domain-wall formation found at low temperatures in chapter 4, even if we restrict consideration to first order calculations. It would be of significant interest to analyze whether the domain-wall formation survives the second order diagrams.

In Figure (5.9) the maxima of the amplitudes of the staggered magnetization obtained in the ED-code in first and in second order perturbation theory are shown as a function of
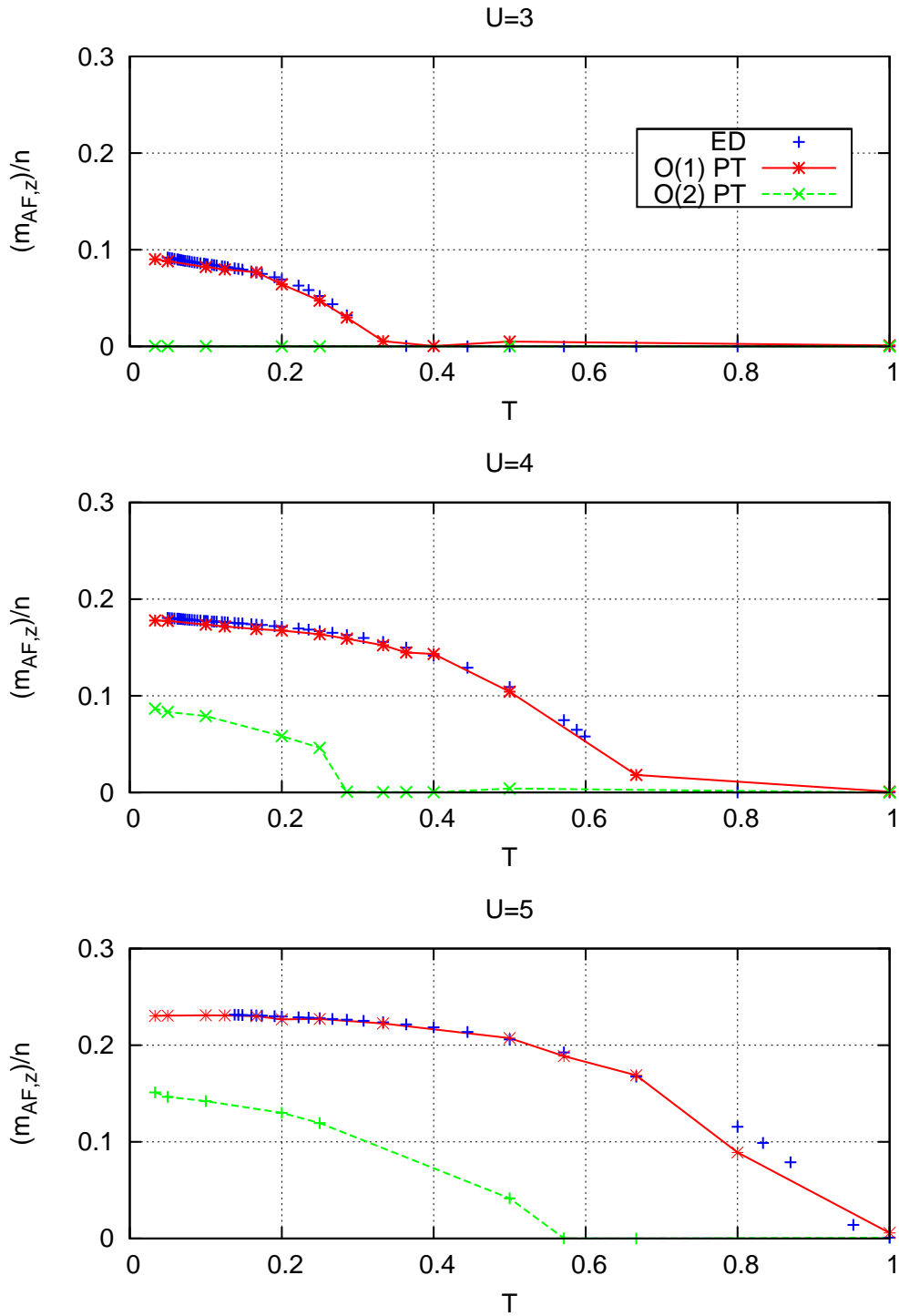
Figure 5.9: Maximum of the magnetic order parameter in first order (ED+PT code) and second order perturbation theory. The ED and the PT-code yield quantitatively similar results. The second order contribution reduces the magnetization in size. At $U = 3$ the second order contribution makes the order vanish completely.

temperature for different values of U. Again, we see good agreement between the ED-code and the first order diagrams, due to an accurate choice of $\delta \propto 10^{-4}$. Note that the choice of $U = 5$ leads to unphysical predictions in a translationally invariant system due to the absence of quantum fluctuations [see Figure (5.6)]. Here, this is not the case, since with the trap included the Hartree order parameter is smaller than in the translationally invariant system and comparable to the order parameter at $U = 3$ in the untrapped case. It reveals, that at $U = 3$ the symmetry breaking is completely suppressed by the second order terms. For $U = 4$ and $U = 5$ both the Néel temperature and the maximal order parameter at a fixed temperature are reduced, depending on U and $T = 1/\beta$. Hence, we may summarize the results of this chapter as follows:

- We have included quantum fluctuations perturbatively within a real-space Baym-Kadanoff conserving approximation.

- The first order results are in good quantitative agreement with the ED-results.

- Quantum fluctuations in second order do not suppress antiferromagnetism in finite size systems as in translationally invariant ones with infinite extension.

- The sizes of Néel temperatures and order parameters for $T \geq 0$ are renormalized and are of the same order of magnitude as the predictions of the Hartree-Fock approximation, at least for the (modest) system sizes that could be considered up till now.

5.4   Dynamical mean field theory

As the last point of this chapter we want to present an outlook regarding further calculations within the Dynamical mean field theory (DMFT). The DMFT has become of great interest in the context of ultracold Fermi gases for the description of Mott-transitions [30, 28] as well as in the context of antiferromagnets [46, 100]. The key issue in the DMFT approximation is the neglect of non-local correlations which can be simplified for z-antiferromagnets to the expression [46, 101, 102]

$$\Sigma_{ij\,\sigma\sigma'}(\omega) \rightarrow \delta_{ij}\delta_{\sigma\sigma'}\Sigma_{i\sigma}(\omega) \ . \tag{5.18}$$

The local self-energy may be computed perturbatively as it could be done with the computer program used to obtain the results of this chapter [103] or by mapping each lattice site on a single Anderson impurity model (SIAM) and afterwards solving the SIAM non-perturbatively [46, 100]. The coincidence of the Green functions of the SIAM $G_{i\sigma}^{\mathrm{SIAM}}$ and the lattice Green function's diagonal parts defines the self-consistency condition [28, 46, 104, 105] (For a detailed review see Ref. [106]):

$$G_{i\sigma}^{\mathrm{SIAM}}(\omega)^{-1} \equiv \mathcal{G}_{ii\sigma\sigma}(\omega)^{-1} + \Sigma_{i\sigma}(\omega) \ . \tag{5.19}$$

Here the SIAM itself is defined via the local action

$$\begin{aligned} \mathcal{A}_i\left[\psi_\sigma, \psi_\sigma^*, G_{i\sigma}^{\mathrm{SIAM}}\right] & \equiv & \sum_\sigma \int_0^\beta \int_0^\beta d\tau d\tau' \psi_\sigma^*(\tau) G_{i\sigma}^{\mathrm{SIAM}}(\tau - \tau')\psi_\sigma(\tau') \\ & - & U \int_0^\beta d\tau\, \psi_\uparrow^*(\tau)\, \psi_\uparrow(\tau)\, \psi_\downarrow^*(\tau)\, \psi_\downarrow(\tau) \ , \end{aligned} \tag{5.20}$$

where τ is the imaginary time and $\psi_\sigma(\tau)$ are the corresponding Grassmann variables. In DMFT Eqs. (5.1), (5.19) and (5.20) form a self-consistency loop, where (5.20) provides the self-energy destinated to be inserted in the Dyson Equation (5.1). Note that one should not
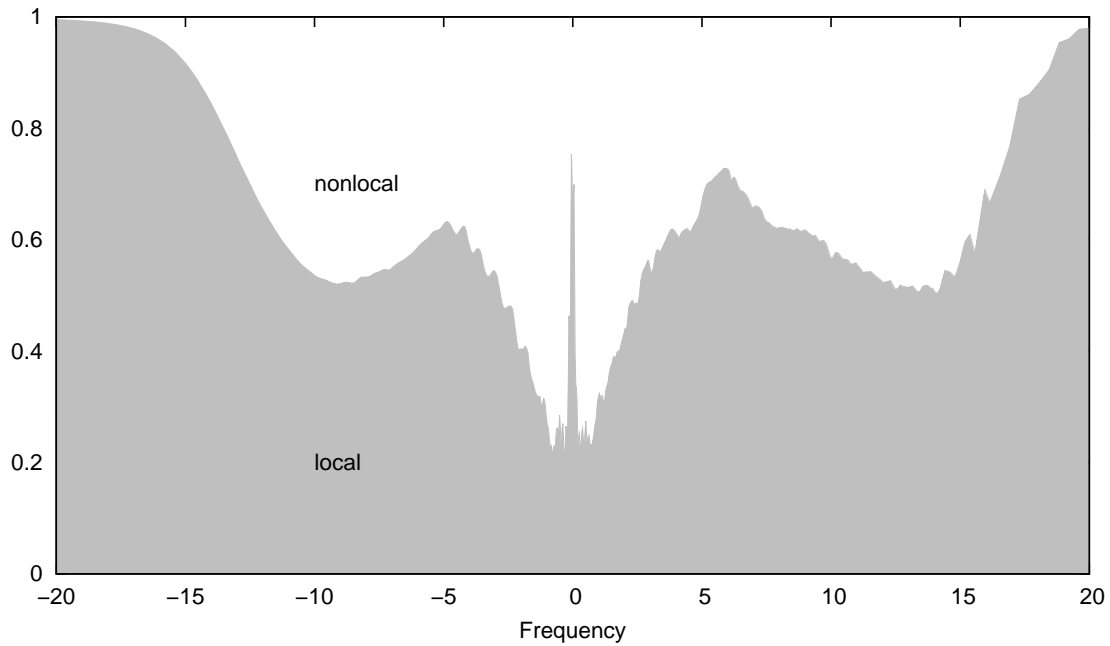
Figure 5.10: Relative weight of local and non-local contributions to a self-consistently determined self-energy. Note that in the vicinity of the Fermi Edge the weight of the nonlocal diagrams is high, so that their contribution is relevant. The system parameters are $U = 6$, $\mu = 2$ and $\beta = 50$ in units of t. The system size is 12×12.

confuse the interaction-free lattice Green function and the Green function of the SIAM and that (5.19) is not a matrix equation in contrast to Eq. (5.1).

There are several non-perturbative ways to solve the SIAM. Wide spread methods are the numerical renormalization group (NRG), which works highly efficiently in the ground state, or QMC methods based on the Hirsch-Fye [107] or continuous time [108] QMC algorithms, which are more adequate for higher temperatures (higher but still below T_N).

Regardless which DMFT solver is used and regardless whether it is perturbative in U, all the DMFT solvers neglect non-local correlations. Although DMFT was developed as an accurate method for high dimensions (or better: a high number of nearest neighbors), it is now being used as an approximation describing two-dimensional antiferromagnetic systems. It seemed to be the best and most efficient choice for performing numerics, especially because the SIAM-solver may be chosen to be non-perturbative and, therefore, the strong coupling regime may be explored in this sense.

At this point we emphasize the results presented in Figure (5.10). This Figure shows that at moderate lattice sizes the weight of nonlocal diagrams becomes in fact relevant in the vicinity of the Fermi edge ($\propto 60\% - 70\%$). This result makes it hard to believe that the neglect of non-local terms yields quantitatively correct results. Note, e.g., that in Ref. [46] a quasi perfect Néel-state within R-DMFT+NRG at $U/t = 10$ in the half-filled region is obtained. This is exactly the same what Hartree-Fock would predict where quantum fluctuations are completely neglected. In fact, the only technical difference between Hartree-Fock and DMFT regarding the z-antiferromagnet is that the local self-energy is constant in Hartree-Fock and ω-dependent in DMFT. The non-local parts of $\Sigma(\omega)$ are neglected in both approaches.

Unfortunately, there is no DMFT-data avaliable nowadays which is comparable (in the

sense of the parameter region) to our second order beyond-DMFT calculations. The production of such data will be one of the next challenges in our group in the near future.

Summary and Outlook

The goal of this thesis is to deepen and broaden our understanding of superfluid and anti-ferromagnetic phenomena in trapped ultracold fermionic quantum gases loaded onto optical lattices. For this purpose we have investigated the Hubbard Hamiltonian (1.15) for different signs of the interaction, for balanced and imbalanced systems and for systems with spin-symmetric and asymmetric hopping.

Summary

We analytically found that for trapped systems the superfluid order parameter can (without loss of generality) be chosen as a real function in space for continuous trapped systems, while this is not necessarily the case for translationally invariant ones. We mapped this result onto our Hubbard Hamiltonian. This analytical statement is in good agreement with the numerical mean field results obtained in chapters 2, where we treat translationally invariant systems, and 3, where we treat trapped ones. Indeed, we generally find a real order parameter for trapped systems and even positively definite ones for totally spin-symmetric systems. These results show that complex ansatzes, which are frequently used in the literature in the context of the LDA, fail in describing an imbalanced superfluid Fermi mixtures. We report spontaneous breaking of the spatial rotational invariance of the Hamiltonian as a consequence of imbalance in certain parameter regions rather than a complex order parameter. Spin-dependent hopping causes the CDW-state to be energetically lower than the superfluid state in a half-filled translationally invariant Hubbard model. We show that, due to the trapping, it is at least very difficult to obtain a thermodynamically stable CDW-phase, even at a strong hopping asymmetry. Furthermore, we show the importance of the inclusion of the Hartree terms, which are often neglected in the literature, within mean field theory. As a complex (but thermodynamically unstable) solution for the order parameter we present numerically stable vortices in balanced and in imbalanced systems as a complement to vortices known from BEC.

For the repulsive-U model we first map the real order parameter of the attractive-U model onto the staggered magnetization occurring in the Néel state. Analytically we obtain an antiferromagnet with an order parameter oriented parallelly to a spatially independent vector in real space. This result is also confirmed by the results of our numerical mean field investigation in chapter 4. In particular, if we turn on the spin-imbalance, we obtain an order parameter aligned perpendicularly to the quantization axis minimizing the grand potential, improving results presented in recent literature. We discuss the experimental implications arising from this fact. In this context we present the broadening of the half-filled spatial region as an additional experimental signature of the antiferromagnetic phase at half filling. An explanation of this fact is also found in chapter 4. Furthermore, we show how temperature affects our results, we present the DOSs corresponding to the real-space particle configurations, we imbed our results in the context of the existing literature on incommensurate spin waves

in the Hubbard model and discuss the role of asymmetric hopping for repulsively interacting fermions. As the last point of chapter 4 we show, why the LDA fails again in predicting even the qualitative behavior of the order parameter for trapped systems.

In chapter 5 we include quantum fluctuations within a second order Feynman-graph self-energy expansion, which extends certain selected results of chapter 4. We find that, qualitatively, the main features found in our mean field analysis survive. Critical temperatures and order parameters are not as drastically reduced in trapped systems as in systems with infinite extension. Also for translationally invariant systems we find a size-dependence of the relative reduction of order parameters due to correlation effects, namely that the bigger the system size is the smaller the order parameter becomes relatively to the corresponding mean field result. This emphasizes the role of the non-diagonal terms of the self-energy, which are often neglected especially in the DMFT.

Outlook

Neither FFLO-like states nor antiferromagnetic ones have ever been found experimentally in ultracold quantum gas experiments. The quest for these phenomena is actually one of the major goals in this experimental field. A successful detection and a comparison of the results with our predictions would be of great interest. Reversely, it would of course be gratifying, if our predictions would turn out to be helpful in the search for and detection of antiferromagnetism.

With the help of a computer program developed specifically for solving this problem we have found different exotic phases occurring in selected parameter regions in mean field theory. Most systems with an appropriate size cannot be analyzed with our real-space Baym-Kadanoff program due to technical restrictions (memory, etc.). Finding whether those phases survive the influence of quantum fluctuations or not would also be of great interest.

The importance of non-diagonal second order terms categorically neglected in DMFT puts results on trapped systems presented recently in the literature seriously into question. A comparison of DMFT data with our data in the relevant parameter region would be able to state whether the DMFT may be used in this context or whether the use of DMFT should be restricted to disordered phases, whence its fame arises and for which it is known to be one of the best approximate methods presently available.

Appendix A

Auxiliary Calculations for Chapter 1

A.1 Derivation of superfluid current and velocity for bosons

The superfluid amplitude is defined as $\rho(\mathbf{x}) \equiv |\Psi(\mathbf{x})|^2$; hence one obtains

$$\frac{\partial}{\partial t}\rho(\mathbf{x}) = \Psi^*(\mathbf{x})\frac{\partial}{\partial t}\Psi(\mathbf{x}) + \Psi(\mathbf{x})\frac{\partial}{\partial t}\Psi^*(\mathbf{x}) \ . \tag{A.1}$$

The Schrödinger equation yields

$$i\hbar\frac{\partial}{\partial t}\Psi(\mathbf{x}) = \left\langle \left[\mathcal{H}, \hat{\Psi}_{\mathbf{B}}(\mathbf{x})\right]\right\rangle \ . \tag{A.2}$$

The commutators are as follows:

$$\left[\mathcal{H}_{\mathrm{K}}, \hat{\Psi}_{\mathbf{B}}(\mathbf{x})\right] = \frac{\hbar^2}{2m}\triangle\hat{\Psi}_{\mathbf{B}}(\mathbf{x}) \ , \tag{A.3}$$

$$\left[\mathcal{H}_{\mathrm{V}}, \hat{\Psi}_{\mathbf{B}}(\mathbf{x})\right] = -V(\mathbf{x})\hat{\Psi}_{\mathbf{B}}(\mathbf{x}) \ , \tag{A.4}$$

$$\left[\mathcal{H}_{\mathrm{U}}, \hat{\Psi}_{\mathbf{B}}(\mathbf{x})\right] = -2\int d\mathbf{z}\, U(\mathbf{x}-\mathbf{z})\,\hat{\Psi}^\dagger_{\mathbf{B}}(\mathbf{z})\hat{\Psi}_{\mathbf{B}}(\mathbf{z})\hat{\Psi}_{\mathbf{B}}(\mathbf{x}) \ . \tag{A.5}$$

Combining Eqns. (A.1) - (A.4) and neglecting the contribution from (A.5) yields

$$\frac{\partial}{\partial t}\rho(\mathbf{x}) = \frac{\hbar}{2im}\left[\Psi^*(\mathbf{x})\triangle\Psi(\mathbf{x}) - \Psi(\mathbf{x})\triangle\Psi^*(\mathbf{x})\right] \tag{A.6}$$

$$= \nabla\cdot\frac{\hbar}{2im}\left[\Psi^*(\mathbf{x})\nabla\Psi(\mathbf{x}) - \Psi(\mathbf{x})\nabla\Psi^*(\mathbf{x})\right] \tag{A.7}$$

$$\equiv -\nabla\cdot\mathbf{j}(\mathbf{x}) \ . \tag{A.8}$$

Hence, if we use $\Psi(\mathbf{x}) = |\Psi(\mathbf{x})|\exp(i\varphi(\mathbf{x}))$, the current density $\mathbf{j}(\mathbf{x})$ may be written as

$$\mathbf{j}(\mathbf{x}) = \frac{\hbar}{m}|\Psi(\mathbf{x})|^2\,\nabla\varphi(\mathbf{x}) \ . \tag{A.9}$$

The contribution arising from the interaction term may be used in dilute gases [63] since $U(\mathbf{x}-\mathbf{x}')$ is assumed to be small or to be short ranged $U(\mathbf{x}-\mathbf{x}') = U\delta(\mathbf{x}-\mathbf{x}')$. Under this condition Eq. (A.5) yields

$$\left[\mathcal{H}_{\mathrm{U}}, \hat{\Psi}_{\mathbf{B}}(\mathbf{x})\right] = -2U\,\hat{\Psi}^\dagger_{\mathbf{B}}(\mathbf{x})\hat{\Psi}^2_{\mathbf{B}}(\mathbf{x}) \ . \tag{A.10}$$

In the Gross-Pitaevski approach, which is commonly used for dilute gases [63], the bosonic field operator is decomposed in a mean-field plus a fluctuation-term $\hat{\Psi}_{\mathbf{B}}(\mathbf{x}) \rightarrow \Psi(\mathbf{x}) + \delta\hat{\Psi}_{\mathbf{B}}(\mathbf{x})$. Leading to

$$\left[\mathcal{H}_{\mathrm{U}}, \hat{\Psi}_{\mathbf{B}}(\mathbf{x})\right] \sim |\Psi(\mathbf{x})|^2 \, \Psi(\mathbf{x}) + \mathcal{O}(U\delta\hat{\Psi}_{\mathbf{B}}(\mathbf{x})) \, . \tag{A.11}$$

Hence, the contribution arising from the interaction in (A.6) is of the order of $\mathcal{O}(U\delta\hat{\Psi}_{\mathbf{B}}(\mathbf{x}))$ and may therefore be neglected.

The definition of the superfluid velocity follows from the standard hydrodynamic equation

$$\mathbf{v}(\mathbf{x}) \equiv \frac{\mathbf{j}(\mathbf{x})}{\rho(\mathbf{x})} = \frac{\hbar}{m}\nabla\varphi(\mathbf{x}) \, . \tag{A.12}$$

Hence, the motion of a superfluid condensate is highly restricted [63].

A.2   Derivation of superfluid current and velocity for fermions

For fermions we define the superfluid density as $\rho(\mathbf{x}, \mathbf{x}') \equiv |\Delta(\mathbf{x}, \mathbf{x}')|^2$, so that the diagonal terms $\mathbf{x} = \mathbf{x}'$ are defined analogously to the bosonic case. Hence, one has to compute

$$i\hbar\frac{\partial}{\partial t}\Delta(\mathbf{x}, \mathbf{x}') = \left\langle \left[\mathcal{H}, \hat{\psi}_{\downarrow}(\mathbf{x})\hat{\psi}_{\uparrow}(\mathbf{x}')\right]\right\rangle \, . \tag{A.13}$$

Analogously to the bosonic case we have:

$$\left[\mathcal{H}_{\mathrm{K}}, \hat{\psi}_{\downarrow}(\mathbf{x})\hat{\psi}_{\uparrow}(\mathbf{x}')\right] = \frac{\hbar^2}{2m}\left(\triangle_{\mathbf{x}} + \triangle_{\mathbf{x}'}\right)\hat{\psi}_{\downarrow}(\mathbf{x})\hat{\psi}_{\uparrow}(\mathbf{x}') \, , \tag{A.14}$$

$$\left[\mathcal{H}_{\mathrm{V}}, \hat{\psi}_{\downarrow}(\mathbf{x})\hat{\psi}_{\uparrow}(\mathbf{x}')\right] = -\left(V_{\downarrow}(\mathbf{x}) + V_{\uparrow}(\mathbf{x}')\right)\hat{\psi}_{\downarrow}(\mathbf{x})\hat{\psi}_{\uparrow}(\mathbf{x}') \, , \tag{A.15}$$

$$\left[\mathcal{H}_{\mathrm{U}}, \hat{\psi}_{\downarrow}(\mathbf{x})\hat{\psi}_{\uparrow}(\mathbf{x}')\right] = \int d\mathbf{z}\, U(\mathbf{x}-\mathbf{z})\,\hat{\psi}_{\uparrow}^{\dagger}(\mathbf{z})\hat{\psi}_{\uparrow}(\mathbf{z})\hat{\psi}_{\uparrow}(\mathbf{x}')\hat{\psi}_{\downarrow}(\mathbf{x}) \tag{A.16}$$

$$- \int d\mathbf{z}\, U(\mathbf{x}'-\mathbf{z})\,\hat{\psi}_{\downarrow}^{\dagger}(\mathbf{z})\hat{\psi}_{\downarrow}(\mathbf{z})\hat{\psi}_{\downarrow}(\mathbf{x})\hat{\psi}_{\uparrow}(\mathbf{x}')$$

$$- U(\mathbf{x}'-\mathbf{x})\hat{\psi}_{\downarrow}(\mathbf{x})\hat{\psi}_{\uparrow}(\mathbf{x}') \, .$$

Hence, introducing the $2d$-dimensional coordinates $\mathbf{y} \equiv (\mathbf{x}, \mathbf{x}')^T$, Eq. (A.14) takes the form

$$\left[\mathcal{H}_{\mathrm{K}}, \hat{\Delta}(\mathbf{y})\right] = \frac{\hbar^2}{2m}\triangle_{\mathbf{y}}\,\hat{\Delta}(\mathbf{y}) \quad ; \quad \hat{\Delta}(\mathbf{y}) \equiv \hat{\psi}_{\downarrow}(\mathbf{x})\hat{\psi}_{\uparrow}(\mathbf{x}') \, . \tag{A.17}$$

Eq. (A.17) has the same form as for bosons in Eq. (A.3). The introduction of the generalized $2d$-dimensional "supercurrent"

$$\mathbf{j}_S(\mathbf{y}) \equiv \frac{\hbar}{m}|\Delta(\mathbf{y})|^2\,\nabla_{\mathbf{y}}\varphi(\mathbf{y}) \quad ; \quad \Delta(\mathbf{y}) = |\Delta(\mathbf{y})|\exp(i\varphi(\mathbf{y})) \tag{A.18}$$

allows to generalize (1.23) for fermions.

The contribution arising from the interaction term (A.16) leads the continuity to take the form $(\rho_S \equiv |\Delta(\mathbf{y})|^2)$

$$\frac{\partial\rho_S}{\partial t} + \nabla_{\mathbf{y}}\cdot\mathbf{j}_S = \frac{\Delta^*}{i\hbar}\left[\int d\mathbf{z}\, U(\mathbf{x}-\mathbf{z})\,\hat{\psi}_{\uparrow}^{\dagger}(\mathbf{z})\hat{\psi}_{\uparrow}(\mathbf{z})\hat{\psi}_{\uparrow}(\mathbf{x}')\hat{\psi}_{\downarrow}(\mathbf{x}) \right. \tag{A.19}$$

$$\left. - \int d\mathbf{z}\, U(\mathbf{x}'-\mathbf{z})\,\hat{\psi}_{\downarrow}^{\dagger}(\mathbf{z})\hat{\psi}_{\downarrow}(\mathbf{z})\hat{\psi}_{\downarrow}(\mathbf{x})\hat{\psi}_{\uparrow}(\mathbf{x}')\right] + \text{h.c.} \, ,$$

so that the third row in (A.16) does not contribute. Introducing a contact interaction $U\delta(\mathbf{x} - \mathbf{x}') = U(\mathbf{x} - \mathbf{x}')$ leads to

$$\frac{\partial \rho_S}{\partial t} + \nabla_{\mathbf{y}} \cdot \mathbf{j}_S = \frac{U\Delta^*}{i\hbar} \left[\hat{\psi}_\uparrow^\dagger(\mathbf{x})\hat{\psi}_\uparrow(\mathbf{x})\hat{\psi}_\uparrow(\mathbf{x}')\hat{\psi}_\downarrow(\mathbf{x}) - \hat{\psi}_\downarrow^\dagger(\mathbf{x}')\hat{\psi}_\downarrow(\mathbf{x}')\hat{\psi}_\downarrow(\mathbf{x})\hat{\psi}_\uparrow(\mathbf{x}') \right] + \text{h.c.} \ , \quad \text{(A.20)}$$

so that the interaction term does not influence the time dependence of $|\Delta(\mathbf{y})|^2_{\mathbf{x}=\mathbf{x}'}$, because of the fermionic anticommutation relations. In the case of a contact interaction it holds that $|\Delta(\mathbf{y})|^2_{\mathbf{x}=\mathbf{x}'} \gg |\Delta(\mathbf{y})|^2_{\mathbf{x}\neq\mathbf{x}'}$. Furthermore we assume the interaction strength U to be small compared to all other energy scales of our system. Hence, we neglect the contribution of (A.16) from now on.

The standard interpretation of a d-dimensional current as in the bosonic case, where we found $\mathbf{j} = \frac{\hbar}{m}|\Delta(\mathbf{x})|^2 \nabla\varphi(\mathbf{x})$ fails, since (A.14) for $\mathbf{x} = \mathbf{x}'$ leads to (using the standard product rule)

$$\begin{aligned} i\hbar\frac{\partial\Delta(\mathbf{x})}{\partial t} &= \left. \frac{\hbar^2}{2m}(\triangle_{\mathbf{x}} + \triangle_{\mathbf{x}'})\Delta(\mathbf{x},\mathbf{x}')\right|_{\mathbf{x}'\to\mathbf{x}} \\ &= \frac{\hbar^2}{2m}\left[\triangle_{\mathbf{x}}\Delta(\mathbf{x}) - 2\nabla_{\mathbf{x}}\cdot\nabla_{\mathbf{x}'}\Delta(\mathbf{x},\mathbf{x}')|_{\mathbf{x}'\to\mathbf{x}}\right] \ , \end{aligned} \quad \text{(A.21)}$$

leading to the modified continuity equation (1.26). The contribution from the interaction term vanishes exactly for a contact interaction.

A.3 Mass-imbalanced systems

In systems with a mass-imbalance, Equation (A.14) has to be adapted as

$$\left[\mathcal{H}_{\mathrm{K}}, \hat{\psi}_\downarrow(\mathbf{x})\hat{\psi}_\uparrow(\mathbf{x}')\right] \to \frac{\hbar^2}{2}\left(\frac{\triangle_{\mathbf{x}}}{m_\downarrow} + \frac{\triangle_{\mathbf{x}'}}{m_\uparrow}\right)\hat{\psi}_\downarrow(\mathbf{x})\hat{\psi}_\uparrow(\mathbf{x}') \ . \quad \text{(A.22)}$$

It is obvious that there is no way to obtain an equation of the form (1.26). With the help of the generalized "supercurrent"

$$\mathbf{j}_s(\mathbf{y}) \to \hbar|\Delta(\mathbf{y})|^2 \, (\mathcal{W}\nabla_{\mathbf{y}})\, \varphi(\mathbf{y}) \quad , \quad \mathcal{W} \equiv \mathrm{diag}_{2d\times 2d}\left(\frac{1}{m_\downarrow},\ldots,\frac{1}{m_\downarrow},\frac{1}{m_\uparrow},\ldots,\frac{1}{m_\uparrow}\right) \quad \text{(A.23)}$$

it is simple to generalize (1.23) as follows:

$$\begin{aligned} 0 = \int_{\partial V} d\mathbf{F}\cdot[\varphi(\mathbf{y})\,\mathbf{j}(\mathbf{y})] &= \int_V dV\,\nabla\cdot[\varphi(\mathbf{y})\,\mathbf{j}(\mathbf{y})] \\ &\approx \int_V dV\,\mathbf{j}(\mathbf{y})\cdot\nabla\varphi(\mathbf{y}) \\ &= \frac{1}{\hbar}\int_V dV\,\frac{\mathbf{j}(\mathbf{y})\cdot\left(\mathcal{W}^{-1}\mathbf{j}(\mathbf{y})\right)}{|\Psi(\mathbf{y})|^2} \ . \end{aligned} \quad \text{(A.24)}$$

Since $\mathcal{W}^{-1}$ is positively definite, the "supercurrent" must also vanish in the mass-imbalanced case.

Appendix B

Auxiliary Calculations for Chapter 3

B.1 Range of the self-consistency equations (3.9) and (3.10)

Equation (3.9) is trivial, since the matrix elements $u_{\mathbf{i}s,\sigma}$ represent orthonormal vectors, therefore one obtains

$$0 \leq \sum_{s=1}^{2\mathcal{N}} |u_{\mathbf{i}s,\sigma}|^2 f_\beta(\sigma E_s) \leq \sum_{s=1}^{2\mathcal{N}} |u_{\mathbf{i}s,\sigma}|^2 = 1 \ . \tag{B.1}$$

A proof for (3.10) can be derived as follows:

$$
\begin{aligned}
|\Delta(\mathbf{i})| &= \exp(-i\varphi)\Delta(\mathbf{i}) = \sum_{s=1}^{2\mathcal{N}} \exp(-i\varphi) u_{\mathbf{i}s,\uparrow} u_{\mathbf{i}s,\downarrow}^* f_\beta(E_s) \tag{B.2} \\
&= \sum_s a_{s+} f_\beta(E_s) + \sum_s a_{s-} f_\beta(E_s) \ ,
\end{aligned}
$$

where $a_{s+(-)}$ contains the positive (negative) contributions to $\Re(|\Delta(\mathbf{i})|)$. It immediately follows

$$|\Delta(\mathbf{i})| \leq \Re\left(\sum_s a_{s+}\right) \ . \tag{B.3}$$

Furthermore, one obtains

$$\sum_{s=1}^{2\mathcal{N}} u_{\mathbf{i}s,\uparrow} u_{\mathbf{i}s,\downarrow}^* = 0 \ \Rightarrow \ \sum_s a_{s+} + \sum_s a_{s-} = 0 \ , \tag{B.4}$$

since the matrix $u_{\mathbf{i}s,\sigma}$ is unitary. On the other hand one can show

$$
\begin{aligned}
\Re\left(\sum_s a_{s+}\right) - \Re\left(\sum_s a_{s-}\right) &\leq \left|\sum_s a_{s+}\right| + \left|\sum_s a_{s-}\right| \\
&\leq \sum_s |a_{s+}| + \sum_s |a_{s-}| \\
&= \sum_{s=1}^{2\mathcal{N}} |u_{\mathbf{i}s,\uparrow}| \, |u_{\mathbf{i}s,\downarrow}^*| \tag{B.5} \\
&\equiv \tilde{\mathbf{u}}_{\mathbf{i},\uparrow} \cdot \tilde{\mathbf{u}}_{\mathbf{i},\downarrow} \\
&\leq 1 \ ,
\end{aligned}
$$

where we have used again that the matrix $u_{\mathbf{i}s}$ is unitary and the Schwarz-inequality. Combining Equations (B.3) - (B.5) finally yields

$$|\Delta(\mathbf{i})| \leq \frac{1}{2} \;. \tag{B.6}$$

Appendix C

The Saddle-point Approximation Computer Program

In this part of the appendix we briefly describe the saddle-approximation solver used to produce the numerical results in chapters 2 - 4, which was a part of this PhD-thesis.

As explained mainly in the text of chapter 3, the main challenge of this code is the diagonalization of matrices and handling with linear algebra systems. Hence, the code is written in C++ using the Blitz++ package for perfomantly handling linear algebra systems. The diagonalization of the matrices itself is done by wrapping the GSL-Eigenvalue package in the Blitz++ environment.

The program uses the real-space formalism as presented in chapter 3. It is able to calculate self-consistently systems with attractive or repulsive interaction, where internally it is always used an attractive interaction. If the interaction is repulsive, the program automatically performs a special particle-hole transformation (1.35) before starting iterations and after finishing the iterations the results are transformed back.

The adjustable physical parameters are: $t_\uparrow$, $t_\downarrow$, U, μ_σ, β and the confining potential as a matrix V_σ. Furthermore, it is possible to adjust the boundary conditions by multiplying the hopping amplitudes beyond the boundaries with a factor $0 \leq \lambda \leq 1$ in order to switch softly from fixed ($\lambda = 0$) to periodic ($\lambda = 1$) boundary conditions. Since in the literature the Hartree terms are often neglected it is also possible to perform the same type of multiplication with a factor ξ.

The output of the program prints the particle densities $n_{\mathbf{i}\sigma}$ and the superfluid order parameter $\Delta(\mathbf{i})$ (xy-magnetic parameter $S_{\mathbf{i}x/y}$)) in the attractive (repulsive) case. Furthermore, the energy spectrum, the eigenstates and non-diagonal correlation functions as $\langle \hat{c}_{\mathbf{i}\downarrow} \hat{c}_{\mathbf{j}\uparrow} \rangle$ may be extracted.

Bibliography

[1] M. H. Anderson, J. R. Ensher, M. R. Matthews, C. E. Wieman and E. A. Cornell, Observation of Bose-Einstein Condensation in a Dilute Atomic Vapor, Science **269**, 198 (1995).

[2] D. Jaksch, C. Bruder, J. I. Cirac, C. W. Gardiner and P. Zoller, Cold Bosonic Atoms in Optical Lattices, Phys. Rev. Lett. **81**, 3108 (1998).

[3] I. Bloch, J. Dalibard and W. Zwerger, Many-body physics with ultracold gases, Rev. Mod. Phys. **80**, 885 (2008).

[4] M. Greiner, O. Mandel, T. Esslinger, T. W. Hänsch and I. Bloch, Quantum phase transition from a superfluid to a Mott insulator in a gas of ultracold atoms, Nature **415**, 39 (2002).

[5] M. Greiner, PhD thesis, LMU München, 2003.

[6] D. van Oosten, PhD thesis, Universiteit Utrecht, Utrecht, 2004.

[7] F. Gerbier, A. Widera, S. Fölling, O. Mandel, T. Gericke and I. Bloch, Interference pattern and visibility of a Mott insulator, Phys. Rev. A **72**, 053606 (2005).

[8] S. Fölling, A. Widera, T. Müller, F. Gerbier and I. Bloch, Formation of a Spatial Shell Structure in the Superfluid to Mott Insulator Transition, Phys. Rev. Lett. **97**, 060403 (2006).

[9] I. Bloch, Ultracold quantum gases in optical lattices, Nature Physics **1**, 23 (2005).

[10] S. Fölling, S. Trotzky, P. Cheinet, M. Feld, R. Saers, A. Widera, T. Müller, and I. Bloch, Direct observation of second-order atom tunnelling, Nature **448**, 1029 (2007).

[11] S. Trotzky, P. Cheinet, S. Fölling, M. Feld, U. Schnorrberger, A. M. Rey, A. Polkovnikov, E. A. Demler, M. D. Lukin and I. Bloch, Time-Resolved Observation and Control of Superexchange Interactions with Ultracold Atoms in Optical Lattices, Science **319**, 295 (2008).

[12] J. Bardeen, L. N. Cooper and J. R. Schrieffer, Theory of Superconductivity, Phys. Rev. **108**, 1175 (1957).

[13] R. B. Diener and Tin-Lun Ho, Fermions in Optical Lattices swept across Feshbach Resonances, Phys. Rev. Lett. **96**, 010402 (2006).

[14] C. A. Regal, M. Greiner and D. S. Jin, Observation of Resonance Condensation of Fermionic Atom Pairs, Phys. Rev. Lett. **92**, 040403 (2004).

[15] M. W. Zwierlein, A. Schirotzek, C. H. Schunck and W. Ketterle, Fermionic Superfluidity with Imbalanced Spin Populations, Science **311**, 492 (2006).

[16] G. B. Partridge, Wenhui Li, R. I. Kamar, Yean-an Liao and R. G. Hulet, Pairing and Phase Separation in a Polarized Fermi Gas, Science **311**, 503 (2006).

[17] G. B. Partridge, Wenhui Li, Y. A. Liao, R. G. Hulet, M. Haque and H. T. C. Stoof, Deformation of a Trapped Fermi Gas with Unequal Spin Populations, Phys. Rev. Lett. **97**, 190407 (2006).

[18] K. B. Gubbels, M. W. J. Romans and H. T. C. Stoof, Sarma Phase in Trapped Unbalanced Fermi Gases, Phys. Rev. Lett. **97**, 210402 (2006).

[19] M. M. Parish, F. M. Marchetti, A. Lamacraft, and B. D. Simons, Finite temperature phase diagram of a polarised Fermi condensate, Nature Physics **3**, 124 (2007).

[20] J. Kinnunen, L. M. Jensen and P. Törmä, Strongly Interacting Fermi Gases with Density Imbalance, Phys. Rev. Lett. **96**, 110403 (2006).

[21] K. Machida, T. Mizushima and M. Ichioka, Generic Phase Diagram of Fermion Superfluids with Population Imbalance, Phys. Rev. Lett. **97**, 120407 (2006).

[22] P. Noizières and S. Schmitt-Rink, Bose Condensation in an Attractive Fermion Gas: From Weak to Strong Coupling Superconductivity, J. Low Temp. Phys. **59**, 195 (1985).

[23] D. E. Sheehy and L. Radzihovsky, BEC-BCS Crossover in "Magnetized" Feshbach-Resonantly Paired Superfluids, Phys. Rev. Lett. **96**, 060401 (2006).

[24] M. M. Parish, S. K. Baur, E. J. Mueller and D. A. Huse, Quasi-one-dimensional polarized Fermi superfluids, Phys. Rev. Lett. **99**, 250403 (2007).

[25] J. Hubbard, Electron Correlations in Narrow Energy Bands, Proc. Roy. Soc. A **276**, 238 (1963).

[26] M. Köhl, H. Moritz, T. Stöferle, K. Günter and T. Esslinger, Fermionic Atoms in a Three Dimensional Optical lattice: Observing Fermi Surfaces, Dynamics, and Interactions, Phys. Rev. Lett. **94**, 080403 (2005).

[27] O. Mandel, M. Greiner, A. Widera, T. Rom, T. W. Hänsch and I. Bloch, Coherent Transport of Neutral Atoms in Spin-Dependent Optical Lattice Potentials, Phys. Rev. Lett. **91**, 010407 (2003).

[28] R. W. Helmes, T. A. Costi and A. Rosch, Mott transition of fermionic atoms in a three-dimensional optical trap, Phys. Rev. Lett. **100**, 056403 (2008).

[29] R. Jördens, N. Strohmaier, K. Günter, H. Moritz and T. Esslinger, A Mott insulator of fermionic atoms in an optical lattice, Nature **455**, 204 (2008).

[30] U. Schneider, L. Hackermüller, S. Will, T. Best, I. Bloch, T. A. Costi, R. W. Helmes, D. Rasch and A. Rosch, Metallic and Insulating Phases of Repulsively Interacting Fermions in a 3D Optical Lattice, Science **322**, 1520 (2008).

[31] J. K. Chin, D. E. Miller, Y. Liu, C. Stan, W. Setiawan, C. Sanner, K. Xu and W. Ketterle, Evidence for superfluidity of ultracold fermions in an optical lattice, Nature **443**, 961 (2006).

[32] M. Iskin and C. A. R. Sá de Melo, Superfluidity of p-wave and s-wave atomic Fermi gases in optical lattices, Phys. Rev. B **72**, 224513 (2005).

[33] M. Iskin and C. A. R. Sá de Melo, Superfluid and Insulating Phases of Fermion Mixtures in Optical Lattices, Phys. Rev. Lett. **99**, 080403 (2007).

[34] C. Honerkamp and W.Hofstetter, BCS Pairing in Fermi Systems with N Different Hyperfine States, Phys. Rev. B **70**, 094521 (2004).

[35] Á. Rapp, G. Zaránd, C. Honerkamp, and W. Hofstetter, Color Superfluidity and "Barion" Formation in Ultracold Fermions, Phys. Rev. Lett. **98**, 160405 (2007).

[36] J. Carlson and S. Reddy, Asymmetric Two-Component Fermion Systems in Strong Coupling, Phys. Rev. Lett. **95**, 060401 (2005).

[37] M. A. Cazalilla, A. F. Ho and T. Giamarchi, Two-Component Fermi Gas on Internal-State-Dependent Optical Lattices, Phys. Rev. Lett. **95**, 226402 (2005).

[38] M. M. Maśka, R. Lemański, J. K. Freericks, and C. J. Williams, Pattern Formation in Mixtures of Ultracold Atoms in Optical Lattices, Phys. Rev. Lett. **101**, 060404 (2008).

[39] W. Hofstetter, J. I. Cirac, P. Zoller, E. Demler and M. D. Lukin, High-Temperature Superfluidity of Fermionic Atoms in Optical lattices, Phys. Rev. Lett. **89**, 220407 (2002).

[40] M. Machida and S. Yamada, Novel Superfluidity in a trapped Gas of Fermi Atoms with Repulsive Interaction Loaded on an Optical Lattice, Phys. Rev. Lett. **93**, 200402 (2004).

[41] R. Barnett, D. Petrov, M. Lukin and E. Demler, Quantum Magnetism with Multicomponent Dipolar Molecules in an Optical lattice, Phys. Rev. Lett. **96**, 190401 (2006).

[42] M. Moore and H. Sadeghpour, Controlling two-species Mott insulator phases in an optical lattice to form an array of dipolar molecules, Phys. Rev. A **67**, 041603(R) (2003).

[43] B. Damski1, L. Santos, E. Tiemann, M. Lewenstein, S. Kotochigova, P. Julienne and P. Zoller, Creation of Dipolar Superfluid in Optical Lattices, Phys. Rev. Lett. **90**, 110401 (2003).

[44] G. Jo, Y. Lee, J. Choi, C. A. Christensen, T. H. Kim, J. H. Thywissen, D. E. Pritchard and W. Ketterle, Itinerant Ferromagnetism in a Fermi Gas of Ultracold Atoms, Science **325**, 1521 (2009).

[45] B. M. Andersen and G. M. Bruun, Magnetic and superfluid phases of confined fermions in two-dimensional optical lattices, Phys. Rev. A **76**, 041602(R) (2007).

[46] M. Snoek, I. Titvinidze, C. Töke, K. Byczuk and W. Hofstetter, Antiferromagnetic order of strongly interacting fermions in a trap: real-space dynamical mean-field analysis, New J. Phys. **10**, 093008 (2008).

[47] F. Werner, O. Parcollet, A. Georges and S. R. Hassan, Interaction-Induced Adiabatic Cooling and Antiferromagnetism of Cold Fermions in Optical Lattices, Phys. Rev. Lett. **95**, 056401 (2005).

[48] A. Koetsier, R. A. Duine, I. Bloch and H. T. C. Stoof, Achieving the Néel state in an optical lattice, Phys. Rev. A **77**, 023623 (2008).

[49] G. M. Bruun, O. F. Syljuåsen, K. G. L. Pedersen, B. M. Andersen, E. Demler, and A. S. Sørensen , Antiferromagnetic noise correlations in optical lattices, Phys. Rev. A **80**, 033622 (2009).

[50] Arnaud Koetsier, F. van Liere, and H. T. C. Stoof, Imbalanced antiferromagnet in an optical lattice, Phys. Rev. A **81**, 023628 (2010).

[51] B. Wunsch, L. Fritz, N. T. Zinner, E. Manousakis, and E. Demler, Magnetic structure of an imbalanced Fermi gas in an optical lattice, Phys. Rev. A **81**, 013616 (2010).

[52] T. A. Corcovilos, S. K. Baur, J. M. Hitchcock, E. J. Mueller, and R. G. Hulet, Detecting antiferromagnetism of atoms in an optical lattice via optical Bragg scattering, Phys. Rev. A **81**, 013415 (2010).

[53] G. G. Batrouni, M. H. Huntley, V. G. Rousseau and R. T. Scalettar, Exact Numerical Study of Pair Formation with Imbalanced Fermion Populations, Phys. Rev. Lett. **100**, 116405 (2008).

[54] A. Luscher, R. M. Noack and A. Laeuchli, The FFLO state in the one-dimensional attractive Hubbard model and its fingerprint in the spatial noise correlations, Phys. Rev. A **78**, 013637 (2008).

[55] M. Rizzi, M. Polini, M. A. Cazalilla, M. R. Bakhtiari, M. P. Tosi and R. Fazio, Fulde-Ferrell-Larkin-Ovchinnikov superfluidity in one-dimensional optical lattices, Phys. Rev. B **77**, 245105 (2008).

[56] B. Wang, Han-Dong Chen, and S. Das Sarma, Quantum phase diagram of fermion mixtures with population imbalance in one-dimensional optical lattices, Phys. Rev. A **79**, 051604(R) (2009).

[57] T. N. De Silva, Population imbalanced Fermi gases in quasi two dimensions, J. Phys. B **42**, 165301 (2009).

[58] S. M. A. Rombouts, Unconventional pairing phases in the two-dimensional attractive Hubbard model with population imbalance, arXiv:cond-mat , 0902.1450 (2009).

[59] I. Deutsch and P. J. Jessen, Quantum-state control in optical lattices, Phys. Rev. A **57**, 1972 (1998).

[60] R. Grimm, M. Weidemüller, Y. B. Ovchinnikov, Optical dipole traps for neutral atoms, Adv. At. Mol. Opt. Phys. **42**, 95 (2000).

[61] D. L. Haycock, P. M. Alsing, I. H. Deutsch, J. Grondalski and P. S. Jessen, Mesoscopic Quantum Coherence in an Optical Lattice, Phys. Rev. Lett. **85**, 3365 (2000).

[62] H. Metcalf and P. van Straten, *Laser Cooling and Trapping*, Springer Verlag, 1999.

[63] C. Pethick and H. Smith, *Bose − Einstein Condensation in Dilute Gases*, Cambridge University Press, Cambridge, 2002.

[64] W.Hofstetter, Ultracold atoms in optical lattices: tunable quantum many-body systems, Philosophical Journal **86**, 1892 (2006).

[65] A. Marte, PhD thesis, Technische Universität München, 2003.

[66] A. Fetter and J. Walecka, *Quantum Theory of Many − Particle Systems*, Dover Publications Inc., Dover, 2003.

[67] F. Freimuth, Diploma thesis, 2005.

[68] S. Giorgini, L. P. Pitaevskii and S. Stringari, Theory of ultracold atomic Fermi gases, Rev. Mod. Phys. **80**, 1215 (2008).

[69] A. J. Leggett, *Quantum Liquids*, Oxford University Press, Oxford, 2006.

[70] T. K. Koponen, T. Paananen, J.-P. Martikainen and P. Törmä, Finite-Temperature Phase Diagram of a Polarized Fermi Gas in an Optical Lattice, Phys. Rev. Lett. **99**, 120403 (2007).

[71] Xiaoling Cui and Yupeng Wang, Polarized Fermi gases in asymmetric optical lattices, Phys. Rev. A **81**, 023618 (2010).

[72] T. K. Koponen, T. Paananen, J.-P. Martikainen, M. R. Bakhtiari and P. Törmä, FFLO state in 1-, 2- and 3-dimensional optical lattices combined with a non-uniform background potential, New J. Phys. **10**, 045014 (2008).

[73] M. Iskin and C. J. Williams, Population imbalanced fermions in harmonically trapped optical lattices, Phys. Rev. A **78**, 011603(R) (2008).

[74] Y. Chen, Z. D. Wang, F. C. Zhang, and C. S. Ting, Exploring exotic superfluidity of polarized ultracold fermions in optical lattices, Phys. Rev. B **79**, 054512 (2009).

[75] N. Ashcroft and D. Mermin, *Solid State Physics*, HRW International Editions, Philadelphia, 1976.

[76] J. Schlipf, PhD thesis, Universität Augsburg, Augsburg, 1998.

[77] C. Knecht, PhD thesis, Johannes Gutenberg-Universität, Mainz, 2006.

[78] J. W. Negele and H. Orland, *Quantum Many − Particle Systems*, Perseus Publishing, 1998.

[79] V. Bach, E. H. Lieb and J. P. Solovej, Generalized Hartree-Fock theory and the Hubbard model, J. Stat. Phys. **76**, 3 (1994).

[80] H. J. Schulz, Incommensurate antiferromagnetism in the two-dimensional Hubbard model, Phys. Rev. Lett. **64**, 1445 (1990).

[81] P. Fulde and R. A. Ferrell, Superconductivity in a Strong Spin-Exchange Field, Phys. Rev. **135**, A550 (1964).

[82] A. I. Larkin and Y. N. Ovchinnikov, Inhomogeneous State of Superconductors, J. Exptl. Theoret. Phys. (U.S.S.R.) **47**, 1136 (1964).

[83] T. K. Koponen, J. Kinnunen, J.-P. Martikainen, L. M. Jensen and P. Törmä, Fermion pairing with spin-density imbalance in an optical lattice, New J. Phys. **8**, 179 (2006).

[84] T. Paananen, Superfluid-density of the ultra-cold Fermi gas in optical lattices, J. Phys. B **42**, 165304 (2009).

[85] T. Paananen, T. K. Koponen, P. Törmä and J.-P. Martikainen, Noise correlations of the ultra-cold Fermi gas in an optical lattice, Phys. Rev. A **77**, 053602 (2008).

[86] T. Gottwald and P. G. J. van Dongen, Ground State Properties of an Asymmetric Hubbard Model for Unbalanced Ultracold Fermionic Quantum Gases, Eur. Phys. J. B **61**, 277 (2008).

[87] G. M. Bruun, B. M. Andersen, E. Demler and A. S. Sørensen, Probing Spatial Spin Correlations of Ultracold Gases by Quantum Noise Spectroscopy, Phys. Rev. Lett. **102**, 030401 (2009).

[88] L.-M. Duan, Detecting Correlation Functions of Ultracold Atoms through Fourier Sampling of Time-of-Flight Images, Phys. Rev. Lett. **96**, 103201 (2006).

[89] T. Gottwald and P. G. J. van Dongen, Antiferromagnetic order of repulsively interacting fermions on optical lattices, Phys. Rev. A **80**, 033603 (2009).

[90] A. Harris and V. Lange, Single-Particle Excitations in Narrow Energy Bands, Phys. Rev. **157**, 295 (1967).

[91] V. Bach, E. H. Lieb and M. V. Travaglia, Ferromagnetism of the Hubbard Model at Strong Coupling in the Hartree-Fock Approximation, Rev. Math. Phys. **18**, 519 (2006).

[92] N.D. Mermin and H. Wagner, Absence of Ferromagnetism or Antiferromagnetism in One- or Two-Dimensional Isotropic Heisenberg Models, Phys. Rev. Lett. **17**, 1133 (1966).

[93] L. M. Falicov and J. C. Kimball, Simple Model for Semiconductor-Metal Transitions: Sm$B6$ and Transition-Metal Oxides, Phys. Rev. Lett. **22**, 997 (1969).

[94] G. Baym, Self-Consistent Approximations in Many-Body Systems, Phys. Rev. **127**, 1391 (1962).

[95] E. Jakobi, PhD thesis, Johannes Gutenberg-Universität, Mainz, 2010.

[96] P. G. J. van Dongen, Extended Hubbard model at weak coupling, Phys. Rev. B **50**, 14016 (1994).

[97] T. Schauerte and P. G. J. van Dongen, Symmetry breaking in the Hubbard model at weak coupling, Phys. Rev. B **65**, 081105(R) (2002).

[98] P. G. J. van Dongen, *Statistische Thermodynamik*, Lecture Notes, Mainz, SoSe 2002.

[99] D. Nelson and J. M. Kosterlitz, Universal Jump in the Superfluid Density of Two-Dimensional Superfluids, Phys. Rev. Lett. **39**, 1201 (1977).

[100] E. V. Gorelik, I. Titvinidze, W. Hofstetter, M. Snoek and N. Blümer, Néel transition of lattice fermions in a harmonic trap: a real-space DMFT study, arXiv:cond-mat , 1004.4857 (2010).

[101] W. Metzner and D. Vollhardt, Correlated Lattice Fermions in $d = \infty$ Dimensions, Phys. Rev. Lett. **62**, 324 (1989).

[102] E. Müller-Hartmann, The Hubbard model at high dimensions: some exact results and weak coupling theory, Z. Phys. B **76**, 211 (1989).

[103] T. W. M. Potthoff and W. Nolting, Interpolating self-energy of the infinite-dimensional Hubbard model: Modifying the iterative perturbation theory, Phys. Rev. B **55**, 16132 (1997).

[104] M. Jarrell, Hubbard model in infinite dimensions: A quantum Monte Carlo study, Phys. Rev. Lett. **69**, 168 (1992).

[105] A. Georges and G. Kotliar, Hubbard model in infinite dimensions, Phys. Rev. B **45**, 6479 (1992).

[106] A. Georges, G. Kotliar, W. Krauth and M. J. Rozenberg, Dynamical mean-field theory of strongly correlated fermion systems and the limit of infinite dimensions, Rev. Mod. Phys. **68**, 13 (1996).

[107] J. E. Hirsch and R. M. Fye, Monte Carlo Method for Magnetic Impurities in Metals, Phys. Rev. Lett. **56**, 2521 (1986).

[108] P. Werner, A. Comanac, L. de' Medici, M. Troyer and A. J. Millis, Continuous-Time Solver for Quantum Impurity Models, Phys. Rev. Lett. **97**, 076405 (2006).

List of publications

Selected parts of this thesis have been published in:

- T. Gottwald and P. G. J. van Dongen, Ground State Properties of an Asymmetric Hubbard Model for Unbalanced Ultracold Fermionic Quantum Gases, Eur. Phys. J. B **61**, 277 (2008).

- T. Gottwald and P. G. J. van Dongen, Antiferromagnetic Order of Repulsively Interacting Fermions on Optical lattices, Phys. Rev. A **80**, 033603 (2009), selected for the October 2009 issue of Virtual Journal of Atomic Quantum Fluids.

The following articles basing on this thesis are in preparation for publication:

- T. Gottwald and P. G. J. van Dongen, FFLO- and Néel States in Finite-size Systems (to be submitted to Phys. Rev. A).

- A. Pfister, E. Jakobi, T. Gottwald and P. G. J. van Dongen, Real-space Baym-Kadanoff Analysis for a two-dimensional Antiferromagnetic System (in preparation).